Universidade Católica Portuguesa
Faculdade de Engenharia

Structural Optimization using the Finite Element Method

João Pedro Pires Mesquita

Dissertação para obtenção do Grau de Mestre em Engenharia Civil

Júri

Prof. Doutor Manuel Barata Marques (Presidente)
Engº. Timo Prißler (Co-Orientador)
Prof. Doutor Mário Rui Tiago Arruda (Convidado)

Setembro 2014

TABLE OF CONTENTS

LIST OF FIGURES

LIST OF TABLES

NOTATION

The symbols used in this work are defined upon the first occurrence in the text. However, for the reader's convenience the meaning of the main acronyms and symbols are given here.

Abbreviations

FEM	Finite Element Method
DOF	Degrees-of-freedom
MPC	Multiple Point Constrain

Symbols

Ω	Domain of a given physical problem
Γ	Boundary of the domain
Γ_u	Dirichlet boundary
Γ_σ	Neumann boundary
$\boldsymbol{u}$	Displacement field
$\boldsymbol{t}_\Gamma$	External force
$\boldsymbol{\sigma}$	Stress components
$\boldsymbol{\varepsilon}$	Strain components
$\boldsymbol{k}$	Material stiffness matrix
$\boldsymbol{K}$	Finite element stiffness matrix
$\boldsymbol{b}$	Body force field
$\boldsymbol{D}$	Equilibrium (divergence) differential operator
$\boldsymbol{D}^*$	Compatibility (gradient) differential operator
$\boldsymbol{u}_\Gamma$	Displacements enforced on the Dirichlet boundary
$\boldsymbol{X}$	Nodal displacement values
$\boldsymbol{U}$	Displacement approximation functions
$\boldsymbol{v}, \overline{\boldsymbol{v}}$	Test functions

$\boldsymbol{n}$	Matrix of the outward normal (Chapter 2) or
	Generic direction versor (Chapter 3)
U	Internal energy density
dU	Variation of the internal energy density
U^*	Complementary energy density
dU^*	Variation of the complementary energy density
U_{tot}	Total internal energy
Π	Total potential energy
W	Work of the external forces
ε_0	Initial state of deformation
Π^*	Complementary potential energy
U_{tot}^*	Complementary internal energy
W^*	Work of the reactions on the enforced boundary displacements
$\boldsymbol{\mathcal{L}}$	A generic linear differential operator
f	Eigenfrequency
E	Young's modulus
ν	Poisson ratio
ρ	Mass density
σ_{max}	Maximum stress in a given body
K_{tn}	Stress concentration factor
w	The golden ratio
$\boldsymbol{e_i}$	Versors of directions *i*
$\boldsymbol{P}$	Arbitrary initial position vector
$\boldsymbol{A}$	The Hessian matrix
$\boldsymbol{H_i}$	Approximation of the inverse of the Hessian matrix
ξ_e	Relative density

ABSTRACT

This work reports on the formulation of the conforming finite element method (FEM) and its application to structural optimization problems. The FEM is nowadays the most widely used technique for obtaining approximate solutions of complex engineering problems that cannot be solved analytically.

The conforming finite element formulation can be reached using several approaches. One of the most general strategies is based on the weak-form of the equations governing the problem. However, rather than a pure mathematical approach, it is often more appealing to the structural engineer to reach the finite element formulation through more physically-meaningful strategies, such as the virtual work or the variational principle forms of the problem. All three of these strategies are briefly presented.

One of the most important topics in the finite element theory is the quality of the solutions. The most commonly used method to increase the quality of a finite element solution is to increase of the number of elements used in the model (mesh refinement). In this work, two numerical examples are presented to illustrate the convergence of the finite element solutions under mesh refinement.

An important application of the FEM and the focus of this work is the structural optimization. The purpose of the structural optimization is to minimize (or maximize) an objective function while respecting certain restrictions. The extremum of a continuous function on a certain interval can either correspond to a point where the gradient is null, or it may lay on the boundary of the interval. Several numerical methods for identifying null gradient points of a function are described in this work. When the extremum of a function lays on the boundary of its interval of definition, an effective minimization method should ensure that the boundaries are searched in such a way that every new iteration yields a result closer to the extremum than the one before. The basic aspects of the constrained minimization methods are briefly presented here and applied to two structural optimization problems, namely the size optimization of a bar subjected to its own weight and the topology optimization of a cantilever plate subjected to a concentrated load applied to its tip.

A large scale practical example of structural optimization, consisting of the topological optimization of a wheel carrier of a motorsports car is also presented. The model is constructed using the finite element package MSC.-NASTRAN. The main goal of the optimization is to minimize the structural weight by reducing the amount of material used in order to create a new

optimized design. The feasible optimized structure is analyzed and the obtained stresses and displacements are compared with the analysis results of the non-optimized structure.

Keywords: Finite Element Method; Structural optimization; Function minimization.

RESUMO

Esta dissertação descreve a formulação do método dos elementos finitos compatíveis (FEM) e respectiva aplicação a problemas de optimização estrutural. O FEM é, hoje em dia, a técnica mais usada para obter soluções aproximadas em problemas complexos de engenharia que não podem ser resolvidos de forma analítica.

A formulação do elemento finito compatível pode ser obtida através de diversas abordagens. Uma das estratégias mais gerais baseia-se na forma-fraca das equações governativas do problema. No entanto, em vez de uma abordagem puramente matemática, é geralmente mais apelativo para o engenheiro estrutural obter a formulação do elemento finito através de estratégias com maior significado físico, tais como o trabalho virtual ou os princípios variacionais.

Um dos tópicos mais importantes na teoria dos elementos finitos é a qualidade das soluções. O método mais usado para aumentar a qualidade de uma solução obtida através do FEM é aumentar o número de elementos usados no modelo (refinamento da malha). Nesta dissertação, dois exemplos numéricos são apresentados de forma a ilustrar a convergência das soluções obtidas através do FEM em função do refinamento da malha.

Uma aplicação importante do FEM e o foco desta dissertação é a optimização estrutural. O objectivo da optimização estrutural é minimizar (ou maximizar) uma função respeitando certas restrições. O extremo de uma função contínua num determinado intervalo pode corresponder a um ponto onde o gradiente é nulo ou situar-se na fronteira do intervalo. Vários métodos numéricos para identificação de pontos de gradiente nulo de uma função são descritos nesta dissertação. Quando o extremo de uma função se situa na fronteira do seu intervalo de definição, um método eficaz de minimização deve garantir que a procura do extremo nas fronteiras é feita de forma a que cada nova iteração produza resultados mais aproximados do extremo do que a iteração anterior. Os aspectos básicos dos métodos de minimização com restrições são sucintamente descritos nesta dissertação e aplicados em dois problemas de optimização estrutural, nomeadamente na optimização da área da secção de uma barra sujeita ao seu peso próprio e na optimização topológica de uma chapa em consola com uma carga aplicada na sua extremidade.

Um exemplo prático de aplicação em larga escala da optimização estrutural, baseado na optimização topológica da estrutura de suporte da roda de um automóvel é também apresentado. O modelo é construído com recurso ao software de elementos finitos MSC.-NASTRAN. O principal objectivo da optimização é baseado na diminuição da massa através da redução da

quantidade de material usado de forma a obter uma nova estrutura optimizada. A estrutura optimizada é analisada, sendo as tensões e deslocamentos obtidos comparados com os valores da análise efectuada na estrutura não-optimizada.

Palavras-chave: Método dos Elementos Finitos; Optimização estrutural; Minimização de funções

ACKNOWLEGMENTS

First and foremost, I would like to express my deep gratitude to my advisor, Ionut Moldovan, for the opportunity of developing this thesis under his guidance and for his endless support. His wise teachings, friendship and dedication were very important during my years at FEUCP.

I would like to thank to my co-advisor, Timo Prißler, for the opportunity of developing the practical part of my thesis at AeRa Technologies GmbH and for his support and friendship during the time in Germany.

To Marcello, Vanessa and Cristina for their support during the time in Germany.

To my parents, Ângelo and Laura, for their love, for the sacrifices I know they have made so I could have the best education and for always believing in my abilities.

To my grandmother for her wise advices and for always having something encouraging to say when I am feeling down.

To my girlfriend Rita, for her love, support, encouragement, countless hours studying together and for always having an endless trust in my abilities.

To my brothers Ivan and Bruno, for their support and for always cheering me up with their endless friendship when I need it the most.

To my cousin, Nadine, for always having a kind word to say.

To my friends David, Duarte, Ricardo and Elton for their support and encouragement.

To my friends from FEUCP, Gonçalo, Kevin, Catarina and Sónia for the countless hours studying together and for their support during my years of study at the University.

1. INTRODUCTION

Many practical engineering problems are too complex to be solved through analytical methods and numerical, approximate approaches must be used instead. Despite the momentum gained by the Numerical Analysis as a scientific field after the emergence of the electronic computer, numerical methods are nowhere near new. In fact, Babylonians used approximate methods to compute irrational numbers some 3700 years ago. Around 1700BC, they used the sexagesimal basis to expand the length of the diagonal of a unit square (i.e. the number $\sqrt{2}$) in an infinite series with arbitrary precision. Polygons were used by Archimedes some 2300 years ago to approximate circles in order to obtain valid approximations of the number π, and later a similar procedure was independently developed by Liu Hui. Virtually all great mathematicians of the Middle Ages have their names linked to some numerical method. Newton's Method is still successfully used today to obtain the roots of real-valued functions; Lagrange's name is linked to the interpolation of functions using polynomial bases; Gaussian integration is still the predilect method for numerical integration of functions and Euler's Method is arguably the simplest numerical procedure for solving ordinary differential equations. The development of electronic computers in the 1940s revolutionized the way the calculations were performed and opened the way to the wide scale use of otherwise old numerical methods (obviously, the impetus behind this trend also led to successive improvements of the methods themselves).

The FEM as a numerical method to solve partial differential equations can be traced back to Courant's work of 1943. Even in this case, however, the underlying principles are older, having been formulated by Ritz in 1909. The Courant's article presented for the first time the idea of dividing the domain into finite triangular sub-regions in the context of the development of a numerical solution of the cylinder torsion problem. However, the contribution of Courant was rather vague, as the presentation was short on details on the mathematical procedure that the author adopted (Gupta & Meek, 1996).

The work of Argyris & Kelsey (1960) represented a significant improvement in the application of the FEM to structural mechanics problems. A matrix approach to the theory of structures was proposed, along with the development of the concepts of stiffness and flexibility matrices. Another landmark was the work of Turner *et al.* (1956), where the study of the deflections of a plate raised the question of convergence by showing that the mesh refinement leads to error decrease. The credit of the naming of the method goes to Clough, who first introduced the concept of "finite elements" in the article Clough (1960), by extending Turner's work on the study of the convergence of the stress components. Another significant advance in

the development of the FEM arised with the work of Zienkiewicz and Cheung (1965), who broadened the application range of the method outside of the framework of solid mechanics and hence to non-structural applications.

The FEM is based on performing a division of a complex domain into a series of smaller regions, referred to as elements, in which the differential equations are approximately solved. This process of subdividing the domain into its elements is called discretization (or "meshing"). The linking between the elements is typically enforced by the adequate choice of the functions used to approximate the physical quantities in each element (conforming or conventional finite elements).

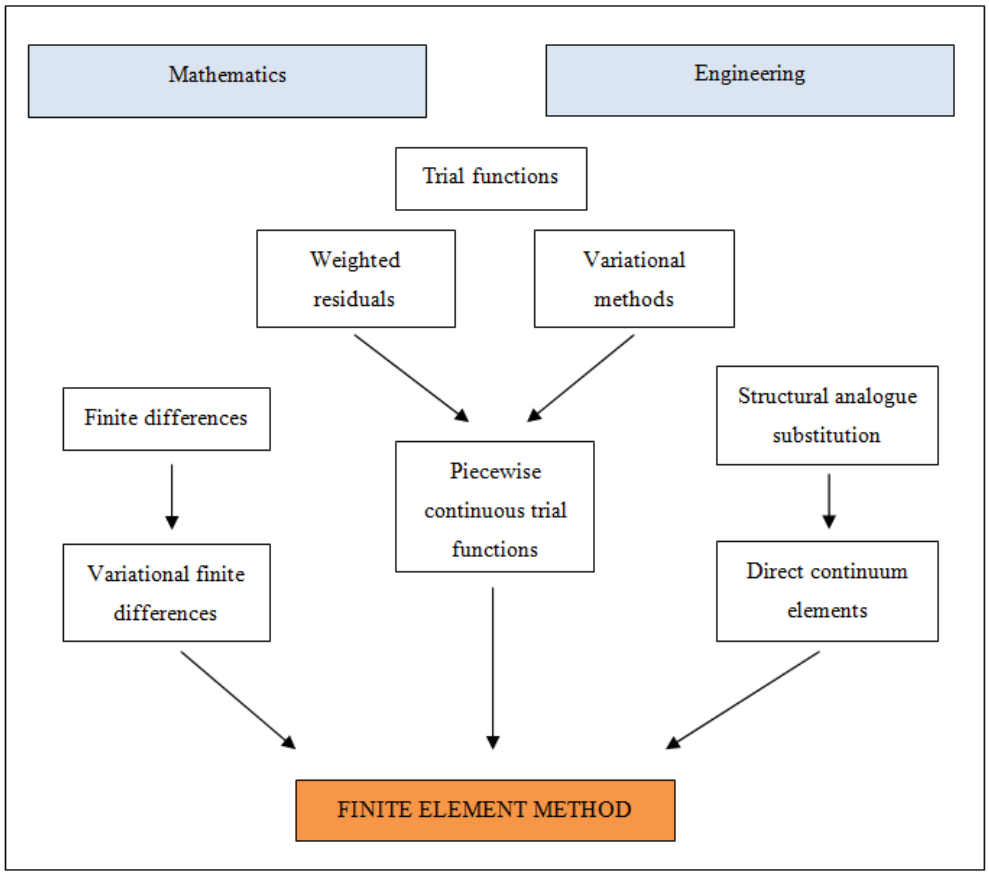

Figure 1-1 - Approximation methods that led to the FEM

Over the years, several approaches to the FEM have been developed, by mathematicians and engineers alike, in an attempt to create techniques capable of yielding acceptable approximations to the real solutions. The approaches range between "purely mathematical" and "structurally intuitive", but despite their different degrees of generality, most conventional

approaches yield similar formulations for structural mechanics problems to those tackled in this work (Zienkiewicz *et al.*, 2005). Figure 1-1 illustrates some of the approaches to the FEM that were proposed over the years.

This multiple perspective philosophy is illustrated in the first part of this work (Chapter 2), where the formulation of the conventional FEM is derived using various perspectives, namely the weak-form approach, the virtual work principle and the variational principles strategy. In the same chapter, the concepts of error and convergence of the FEM are briefly explained and subsequently illustrated using two numerical examples. It is shown how the quality of the results can be improved by decreasing the leading dimension of the finite elements, a process known as mesh refinement.

The fundamentals of structural optimization are presented in Chapter 3. As every structural optimization problem involves finding the extremum of some objective function, several well known function minimization methods, for both one-dimensional and multi-dimensional problems, and with or without additional restrictions, are presented. To illustrate the optimization process, a restricted optimization example of a constant stress bar is presented, as well as a topology optimization problem of a cantilever plate.

In order to illustrate the application of the FEM to the optimization of a more complex structure, the topological optimization of a wheel carrier of a vehicle is presented in Chapter 4.

Finally, Chapter 5 presents the main conclusions of this work, regarding the structural optimization with the FEM, and its importance towards the optimization of large scale structures.

2. FUNDAMENTALS OF THE FINITE ELEMENT METHOD

Complex problems occurring in engineering applications generally lack analytic solution and numerical methods must be used to approximate their solutions. Among these, the FEM is nowadays the most widely used, mainly due to the outstanding versatility and adaptability it offers to the user. To illustrate these features of the FEM, its bases will be presented next, in a wider, general context, followed by particularization to the problem of solid mechanics.

2.1 Problem definition

Consider, in general, a problem given by the set of differential equations,

$$\boldsymbol{\mathcal{A}}(\boldsymbol{u}) = \mathbf{0} \tag{2.1}$$

defined on a domain Ω and by the set of boundary conditions,

$$\boldsymbol{\mathcal{B}}(\boldsymbol{u}) = \mathbf{0} \tag{2.2}$$

applied on its boundary Γ. In expressions (2.1) and (2.2), $\boldsymbol{u}$ is an unknown function, which must be determined.

The general problem definition given above is particularized next for the solid mechanics application presented in Figure 2-1.

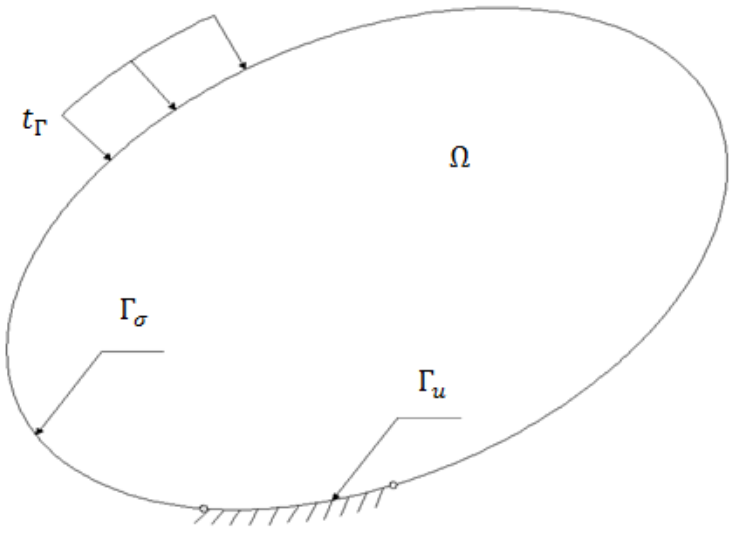

Figure 2-1 - Problem's domain, Dirichlet and Neumann boundaries

Under static conditions, the following equations govern the response of the domain Ω to the external force $\boldsymbol{t_\Gamma}$,

- equilibrium equation

$$\boldsymbol{D\sigma + b = 0} \tag{2.3}$$

- compatibility equation

$$\boldsymbol{D^* u = \varepsilon} \tag{2.4}$$

- constitutive law

$$\boldsymbol{\sigma = k\varepsilon} \tag{2.5}$$

In the above equations, $\boldsymbol{u}$ is the displacement field, vectors $\boldsymbol{\sigma}$ and $\boldsymbol{\varepsilon}$ collect the stress and strain components, $\boldsymbol{k}$ is the material stiffness matrix, $\boldsymbol{b}$ represents the body force field, and $\boldsymbol{D}$ and $\boldsymbol{D^*}$ are the divergence and gradient operators. Equations (2.3) to (2.5) can be merged into the Navier equation,

$$\boldsymbol{DkD^* u + b = 0} \tag{2.6}$$

The Dirichlet (Γ_u) and Neumann (Γ_σ) boundaries of the domain Ω are defined as the parts of the external boundary where the displacements ($\boldsymbol{u_\Gamma}$) and the tractions ($\boldsymbol{t_\Gamma}$) are known,

$$\boldsymbol{u - u_\Gamma = 0}\text{ , on } \Gamma_u \tag{2.7}$$

$$\boldsymbol{n\sigma = t_\Gamma}\text{ , on } \Gamma_\sigma \tag{2.8}$$

2.2 Weak-form approach to the problem

One of the most general ways to derive the finite element formulation associated to a given problem is to use its weak-form as a starting point (Zienkiewicz *et al.*, 2005). The weak-form of equations (2.1) and (2.2) is obtained after enforcing weakly these equations, using some arbitrary functions collected in bases $\boldsymbol{v}$ and $\overline{\boldsymbol{v}}$,

$$\int_\Omega \boldsymbol{v}^T \boldsymbol{\mathcal{A}}(\boldsymbol{u}) d\Omega \; + \int_\Gamma \overline{\boldsymbol{v}}^T \boldsymbol{\mathcal{B}}(\boldsymbol{u})\, d\Gamma = \boldsymbol{0} \tag{2.9}$$

where $\boldsymbol{v}^T$ represents the transpose of vector $\boldsymbol{v}$.

If expression (2.9) is valid for any possible choice of $\boldsymbol{v}$ and $\overline{\boldsymbol{v}}$, it is equivalent to the local satisfaction of the differential equations (2.1) and boundary conditions (2.2). It is important to stress that the integrals in (2.9) must be proper, which poses certain restrictions on

the test functions $\boldsymbol{v}$ and $\overline{\boldsymbol{v}}$ and on the trial functions that are used to approximate the unknown field $\boldsymbol{u}$.

The Equation (2.9) is integrated by parts, to yield, in general,

$$\int_{\Omega} \boldsymbol{\mathcal{C}}(\boldsymbol{v})^T \boldsymbol{\mathcal{D}}(\boldsymbol{u}) d\Omega + \int_{\Gamma} \boldsymbol{\mathcal{E}}(\overline{\boldsymbol{v}})^T \boldsymbol{\mathcal{F}}(\boldsymbol{u}) d\Gamma = \mathbf{0} \tag{2.10}$$

Operators $\boldsymbol{\mathcal{C}}$ to $\boldsymbol{\mathcal{F}}$ present in the weak-form (2.10) normally contain lower order derivatives than the operators from the initial equations (2.1) and (2.2). This renders the choice of the approximation functions more flexible, as lower order degree continuity is required, although a higher degree of continuity is now necessary for the test functions $\boldsymbol{v}$ and $\overline{\boldsymbol{v}}$.

The weak-form approach is applied to solid mechanics problems by enforcing weakly the domain and boundary equations (2.6) and (2.8),

$$\int_{\Omega} \boldsymbol{v}^T (\boldsymbol{D}\boldsymbol{k}\boldsymbol{D}^*\boldsymbol{u} + \boldsymbol{b}) d\Omega + \int_{\Gamma_\sigma} \overline{\boldsymbol{v}}^T (\boldsymbol{t}_{\boldsymbol{\Gamma}} - \boldsymbol{n}\boldsymbol{\sigma}) d\,\Gamma_\sigma = \mathbf{0} \tag{2.11}$$

The kinematic boundary condition (2.7), defined on boundary Γ_u, is not enforced because it is assumed to be respected a priori by the displacement field $\boldsymbol{u}$. This so called "conformity constraint" must therefore be observed by the trial functions used to approximate the displacement field. The kinematic boundary Γ_u is labeled essential boundary, as opposed to the natural boundary Γ_σ, on which boundary condition (2.8) is explicitly included in the weak-form.

Integrating equation (2.11) by parts, results:

$$\int_{\Gamma} \boldsymbol{v}^T \boldsymbol{n}\boldsymbol{\sigma} d\Gamma - \int_{\Omega} (\boldsymbol{D}^*\boldsymbol{v})^T \boldsymbol{\sigma} d\Omega + \int_{\Omega} \boldsymbol{v}^T \boldsymbol{b} d\Omega + \int_{\Gamma_\sigma} \overline{\boldsymbol{v}}^T (\boldsymbol{t}_{\boldsymbol{\Gamma}} - \boldsymbol{n}\boldsymbol{\sigma}) d\Gamma_\sigma = \mathbf{0} \tag{2.12}$$

As the choice of $\boldsymbol{v}$ and $\overline{\boldsymbol{v}}$ is arbitrary, important simplifications can be achieved by setting $\boldsymbol{v} = \overline{\boldsymbol{v}}$ at this point, to yield,

$$-\int_{\Omega} (\boldsymbol{D}^*\boldsymbol{v})^T \boldsymbol{k} (\boldsymbol{D}^*\boldsymbol{u}) d\Omega + \int_{\Omega} \boldsymbol{v}^T \boldsymbol{b} d\Omega + \int_{\Gamma_u} \boldsymbol{v}^T \boldsymbol{n} (\boldsymbol{k}\boldsymbol{D}^*\boldsymbol{u}) d\Gamma_u + \int_{\Gamma_\sigma} \boldsymbol{v}^T \boldsymbol{t}_{\boldsymbol{\Gamma}} d\Gamma_\sigma = \mathbf{0} \tag{2.13}$$

At the same time, choosing basis $\boldsymbol{v}$ such to have $\boldsymbol{v} = \mathbf{0}$ on Γ_u, makes the Dirichlet integral in (2.13) disappear and expression (2.13) simplifies to,

$$-\int_{\Omega} (\boldsymbol{D}^*\boldsymbol{v})^T \boldsymbol{k} (\boldsymbol{D}^*\boldsymbol{u}) d\Omega + \int_{\Omega} \boldsymbol{v}^T \boldsymbol{b} d\Omega + \int_{\Gamma_\sigma} \boldsymbol{v}^T \boldsymbol{t}_{\boldsymbol{\Gamma}} d\Gamma_\sigma = \mathbf{0} \tag{2.14}$$

The FEM is based on the partition of the domain Ω into smaller regions, called finite elements. In each of the finite elements, equation (2.14) remains valid. Using this approach, the integral equation (2.14) can be reduced to a set of algebraic equations by approximating the displacement field in the domain of an element as,

$$\boldsymbol{u} = \boldsymbol{U}\boldsymbol{X} \tag{2.15}$$

In expression (2.15), matrix $\boldsymbol{U}$ collects a subset of a function basis and the unknown vector $\boldsymbol{X}$ lists their weights.

According to the Galerkin principle, the test functions are also expanded in the same basis,

$$\boldsymbol{v} = \boldsymbol{U}\boldsymbol{X} \tag{2.16}$$

Inserting expressions (2.15) and (2.16) into the weak-form (2.14), yields,

$$-\boldsymbol{X}^T \int_{\Omega} (\boldsymbol{D}^*\boldsymbol{U})^T \boldsymbol{k} (\boldsymbol{D}^*\boldsymbol{U}) d\Omega \, \boldsymbol{X} + \boldsymbol{X}^T \int_{\Omega} \boldsymbol{U}^T \boldsymbol{b} d\Omega + \boldsymbol{X}^T \int_{\Gamma_\sigma} \boldsymbol{U}^T \boldsymbol{t}_{\boldsymbol{\Gamma}} d\Gamma_\sigma = \boldsymbol{0} \tag{2.17}$$

which is equivalent to,

$$\boldsymbol{K}\boldsymbol{X} + \boldsymbol{f} = \boldsymbol{0} \tag{2.18}$$

where

$$\boldsymbol{K} = \int_{\Omega} (\boldsymbol{D}^*\boldsymbol{U})^T \boldsymbol{k} (\boldsymbol{D}^*\boldsymbol{U}) d\Omega \tag{2.19}$$

$$\boldsymbol{f} = -\int_{\Omega} \boldsymbol{U}^T \boldsymbol{b} d\Omega - \int_{\Gamma_\sigma} \boldsymbol{U}^T \boldsymbol{t}_{\boldsymbol{\Gamma}} d\Gamma_\sigma \tag{2.20}$$

System (2.18) is symmetric and, when written for the whole finite element mesh, block-diagonal. After its solution, the finite element approximations of the displacement, strain and stress fields are recovered using definition (2.15) and equations (2.4) and (2.5), respectively.

2.3 The virtual work principle as a weak-form

For the structural engineer, it is often more appealing to reach the finite element formulation from the physically-meaningful virtual work principle.

In order to formulate the virtual work principle, it is necessary to enunciate the basic concepts related to internal and complementary energies, and potential and complementary potential energies.

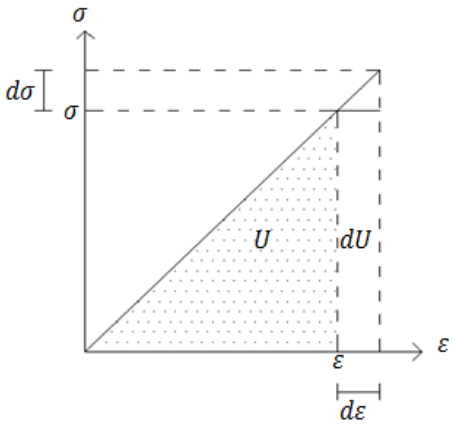

Figure 2-3 - Internal energy density and its variation

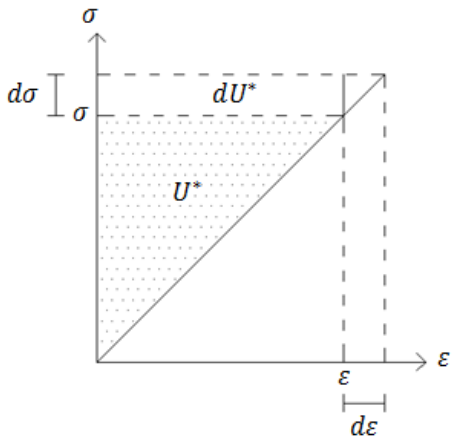

Figure 2-2 - Complementary energy density and its variation

Considering a deformable body subjected to a uniaxial state of stress, and hence experiencing a longitudinal deformation, infinitesimal changes in stress $(\sigma + d\sigma)$ cause infinitesimal increases in deformation $(d\varepsilon)$. The infinitesimal variation of the internal energy density is defined as the work of the stresses on the deformation $d\varepsilon$:

$$dU = \sigma d\varepsilon + \frac{1}{2} d\sigma d\varepsilon \tag{2.21}$$

or, admitting geometrical linearity,

$$dU = \sigma d\varepsilon \tag{2.22}$$

It is now possible to define the internal energy density (associated to the uniaxial stress state) as the sum of all infinitesimal variations (dU) between zero and the final strain (ε),

$$U = \int_0^{\varepsilon} \sigma \, d\varepsilon \tag{2.23}$$

Considering the same body, under the same conditions, the infinitesimal variation of the complementary energy density is defined as the variation of the stress on the total deformation of the body:

$$dU^* = \varepsilon \, d\sigma + \frac{1}{2} d\sigma d\varepsilon \tag{2.24}$$

and for infinitesimal deformations,

$$dU^* = \varepsilon \, d\sigma \tag{2.25}$$

Thus, the complementary energy density associated to the uniaxial state of stress is defined as the sum of all infinitesimal variations (dU^*) between zero and the final stress (σ),

$$U^* = \int_0^{\sigma} \varepsilon \, d\sigma \tag{2.26}$$

It is important to define a correlation between the internal energy density and the complementary energy density, as their sum is equal to the work of a constant stress field on the total strain,

$$U^* + U = \sigma\varepsilon \tag{2.27}$$

The potential energy of a mechanical system is the difference between the total internal energy of the system (U_{tot}) and the work of the applied external and volume forces (W),

$$\Pi = U_{tot} - W \tag{2.28}$$

where,

$$\begin{cases} U_{tot} = \dfrac{1}{2}\displaystyle\int_{\Omega} \boldsymbol{\sigma}^T(\boldsymbol{\varepsilon} - \boldsymbol{\varepsilon_0}) d\Omega \\ \mathrm{W} = \displaystyle\int_{\Gamma_\sigma} \boldsymbol{t}_{\boldsymbol{\Gamma}}^T \, \boldsymbol{u} \, d\Gamma_\sigma + \int_{\Omega} \boldsymbol{b}^T \boldsymbol{u} \, d\Omega \end{cases} \tag{2.29}$$

in which $\boldsymbol{\varepsilon_0}$ is the initial state of deformation.

The complementary potential energy of a mechanical system is defined as the difference between the total complementary internal energy of the system (U_{tot}^*) and the work of the reactions on the enforced boundary displacements (W^*),

$$\Pi^* = U_{tot}^* - W^* \tag{2.30}$$

where,

$$\begin{cases} U_{tot}^* = \dfrac{1}{2}\displaystyle\int_{\Omega} \boldsymbol{\sigma}^T(\boldsymbol{\varepsilon} + \boldsymbol{\varepsilon_0}) d\Omega \\ \mathrm{W}^* = \displaystyle\int_{\Gamma_u} \boldsymbol{t}^T \, \boldsymbol{u}_{\boldsymbol{\Gamma}} \, d\Gamma_u \end{cases} \tag{2.31}$$

The virtual work principle states that, on a deformable body in equilibrium, the exterior work is equal to the internal work, i.e. the work of the applied forces and reactions on the displacement field is equal to the work of the stresses on the corresponding strains,

$$\int_{\Gamma_u} \boldsymbol{t}^T \boldsymbol{u}_{\boldsymbol{\Gamma}}\, d\Gamma_u + \int_{\Gamma_\sigma} \boldsymbol{t}_{\boldsymbol{\Gamma}}^T \boldsymbol{u}\, d\Gamma_\sigma + \int_{\Omega} \boldsymbol{b}^T \boldsymbol{u}\, d\Omega = \int_{\Omega} \boldsymbol{\sigma}^T \boldsymbol{\varepsilon}\, d\Omega \qquad (2.32)$$

By the application of the definitions (2.28) to (2.31) and the property (2.27), it is possible to reach the virtual work principle in the form of potential energies,

$$W^* + W = U_{tot} + U_{tot}^* \Rightarrow \Pi + \Pi^* = 0 \qquad (2.33)$$

There is an immediate correspondence between the weak-form approach to the problem described in Section 2.2 and the virtual work principle. In fact, to create a weak-form it is sufficient to define a weighting function vector,

$$\boldsymbol{v} = \delta\boldsymbol{u} = \boldsymbol{\delta}(\boldsymbol{UX}) = \boldsymbol{U}\, \delta\boldsymbol{X} \qquad (2.34)$$

where $\delta\boldsymbol{u}$ represents any compatible virtual displacement field and $\delta\boldsymbol{X}$ its corresponding weights.

The choice of the test functions above allows the transformation of expression (2.32) into a weak-form equivalent statement,

$$-\delta\boldsymbol{X}^T \int_{\Omega} (\boldsymbol{D}^*\boldsymbol{U})^T \boldsymbol{k} (\boldsymbol{D}^*\boldsymbol{U}) d\Omega\, \boldsymbol{X} + \delta\boldsymbol{X}^T \int_{\Omega} \boldsymbol{U}^T \boldsymbol{b} d\Omega + \delta\boldsymbol{X}^T \int_{\Gamma_\sigma} \boldsymbol{U}^T \boldsymbol{t}_{\boldsymbol{\Gamma}} d\Gamma_\sigma = \boldsymbol{0} \qquad (2.35)$$

As the virtual work principle must hold for any generalized displacements $\delta\boldsymbol{X}$, expression (2.35) simplifies to the finite element system (2.18).

It should be noted that both weak-form and virtual work formulations can be used for linear and non-linear problems. However, the virtual work principle is restricted, in the presented form, to solid mechanics application.

2.4 Variational principle form of the problem

A more general, yet physics-based, approach to the FEM is provided by the so-called variational principles.

In order to approach the concept of variational principle, it is first necessary to define a functional scalar quantity,

$$\Pi = \int_{\Omega} F\left(\boldsymbol{u}, \frac{\partial \boldsymbol{u}}{\partial x}, \ldots\right) d\Omega + \int_{\Gamma} E(\boldsymbol{u}, \frac{\partial \boldsymbol{u}}{\partial x}, \ldots) d\Gamma \tag{2.36}$$

where $\boldsymbol{u}$ is the unknown function and F and E are differential operators. A variational principle states that the correct solution of the problem is the one that makes Π stationary for arbitrary changes $\delta\boldsymbol{u}$,

$$\delta\Pi = 0 \tag{2.37}$$

Although variational principles do not exist for all well posed problems defined by valid partial differential equations, when they do exist, they offer some advantageous properties:

- form (2.37) is very well suited to the framework of the FEM;
- the stiffness matrix always results symmetric/Hermitian.

Symmetric/Hermitian stiffness matrices may, at times, arise from weak formulations as well. When this happens, there exists a variational principle associated to the respective problem, although it may yet be unknown.

The existence and establishment of natural variational principles can be approached by considering the case of a physical problem defined by the partial differential equation

$$\boldsymbol{\mathcal{A}}(\boldsymbol{u}) = \boldsymbol{\mathcal{L}}\boldsymbol{u} + \boldsymbol{b} = \boldsymbol{0} \tag{2.38}$$

in which $\boldsymbol{\mathcal{L}}$ is a differential operator. It can be shown that natural variational principles exist if this operator is self-adjoint, that is,

$$\int_{\Omega} \boldsymbol{\psi}^T (\boldsymbol{\mathcal{L}}\boldsymbol{\gamma}) d\Omega = \int_{\Omega} \boldsymbol{\gamma}^{\mathrm{T}} (\boldsymbol{\mathcal{L}}\boldsymbol{\psi}) d\Omega + \ b.t. \tag{2.39}$$

for any two function sets $\boldsymbol{\psi}$ and $\boldsymbol{\gamma}$, where notation $b.t.$ is used to designate boundary terms. If the requirement above is fulfilled, it is possible to write the function Π, from which the variational principle is obtained, as,

$$\Pi = \int_{\Omega} \left(\frac{1}{2}\boldsymbol{u}^T(\boldsymbol{\mathcal{L}}\boldsymbol{u}) + \ \boldsymbol{u}^T\boldsymbol{b}\right) d\Omega + \ b.t. \tag{2.40}$$

$$\delta\Pi = \frac{1}{2}\int_{\Omega} \delta\boldsymbol{u}^T(\boldsymbol{\mathcal{L}}\boldsymbol{u}) d\Omega + \frac{1}{2}\int_{\Omega} \boldsymbol{u}^T \delta(\boldsymbol{\mathcal{L}}\boldsymbol{u})\, d\Omega + \int_{\Omega} \delta\boldsymbol{u}^T\boldsymbol{b} d\Omega + \ b.t. \tag{2.41}$$

$$\delta\Pi = \int_{\Omega} \delta\boldsymbol{u}^T(\boldsymbol{\mathcal{L}}\boldsymbol{u} + \boldsymbol{b}) d\Omega + \ b.t. = 0 \tag{2.42}$$

Statement (2.42) is called the variational principle form of the initial problem.

The application to solid mechanics is made by identifying forms (2.6) and (2.38), from which results,

$$\boldsymbol{\mathcal{L}} = \boldsymbol{D}\boldsymbol{k}\boldsymbol{D}^{*} \tag{2.43}$$

The first step to obtain the variational principle is to determine if the operator $\mathcal{L}$ is self-adjoint:

$$\int_{\Omega} \delta\boldsymbol{u}^{T}\boldsymbol{\mathcal{L}}\boldsymbol{u}\, d\Omega = \int_{\Gamma} \delta\boldsymbol{u}^{T}\boldsymbol{n}\boldsymbol{\sigma} d\Gamma - \int_{\Omega} (\boldsymbol{D}^{*}\delta\boldsymbol{u})^{T}\boldsymbol{k}\boldsymbol{D}^{*}\boldsymbol{u}\, d\Omega$$

$$= \int_{\Gamma} \delta\boldsymbol{u}^{T}\boldsymbol{n}\boldsymbol{\sigma} d\Gamma - \int_{\Omega} (\boldsymbol{k}\boldsymbol{D}^{*}\delta\boldsymbol{u})^{T}\boldsymbol{D}^{*}\boldsymbol{u}\, d\Omega$$

$$= \int_{\Gamma} \delta\boldsymbol{u}^{T}\boldsymbol{n}\boldsymbol{\sigma} d\Gamma - \int_{\Gamma} (\boldsymbol{n}\delta\boldsymbol{\sigma})^{T}\boldsymbol{u}\, d\Gamma + \int_{\Omega} (\boldsymbol{D}\boldsymbol{k}\boldsymbol{D}^{*}\delta\boldsymbol{u})^{T}\boldsymbol{u}\, d\Omega$$

$$= \int_{\Gamma} \delta\boldsymbol{u}^{T}(\boldsymbol{n}\boldsymbol{\sigma}) d\Gamma - \int_{\Gamma} \boldsymbol{u}^{T}(\boldsymbol{n}\delta\boldsymbol{\sigma}) d\Gamma + \int_{\Omega} \boldsymbol{u}^{T}\boldsymbol{\mathcal{L}}\, d\Omega$$

$$\int_{\Omega} \boldsymbol{u}^{T}\boldsymbol{\mathcal{L}}\delta\boldsymbol{u}\, d\Omega = \int_{\Omega} \delta\boldsymbol{u}^{T}\boldsymbol{\mathcal{L}}\boldsymbol{u}\, d\Omega - \int_{\Gamma} \delta\boldsymbol{u}^{T}(\boldsymbol{n}\boldsymbol{\sigma})\, d\Gamma + \int_{\Gamma} \boldsymbol{u}^{T}(\boldsymbol{n}\delta\boldsymbol{\sigma})\, d\Gamma \tag{2.44}$$

which means that operator $\boldsymbol{\mathcal{L}}$ is indeed self-adjoint.

Once proven the self-adjointness of the operator $\boldsymbol{\mathcal{L}}$, the existence of a natural variational principle is verified. This principle is given by the minimum potential energy theorem,

$$\begin{cases} \Pi = \dfrac{1}{2}\displaystyle\int_{\Omega} \boldsymbol{\varepsilon}^{T}\boldsymbol{\sigma}\, d\Omega - \int_{\Omega} \boldsymbol{u}^{T}\boldsymbol{b}\, d\Omega - \int_{\Gamma_{\sigma}} \boldsymbol{u}^{T}\boldsymbol{t}_{\boldsymbol{\Gamma}}\, d\Gamma_{\sigma} \\ \delta\Pi = 0 \end{cases} \tag{2.45}$$

It is now possible to obtain the variational form of the solid mechanics problem by taking explicitly the differential of the potential energy Π,

$$\delta\Pi = -\int_{\Omega} \delta\boldsymbol{u}^{T}(\boldsymbol{D}\boldsymbol{\sigma} + \boldsymbol{b})\, d\Omega + \int_{\Gamma_{\sigma}} \delta\boldsymbol{u}^{T}(\boldsymbol{n}\boldsymbol{\sigma} - \boldsymbol{t}_{\boldsymbol{\Gamma}})\, d\Gamma_{\sigma} = 0 \tag{2.46}$$

Analyzing and comparing forms (2.46) and (2.11), it is noted that the former represents a particular case of the latter. This fact is always true when variational principles exist. It is important to note that the use of variational principles is restricted to linear elasticity problems, due to the self-adjointness requirement for the operator $\boldsymbol{\mathcal{L}}$.

The finite element formulation based on variational principles (known as the Rayleigh-Ritz method) is immediate when a variational principle exists. Using the approximation,

$$\boldsymbol{u} = \boldsymbol{UX} = \sum_i u_i x_i \qquad (2.47)$$

The differential variation of the functional Π is expressed as,

$$\delta\Pi = \frac{\partial\Pi}{\partial x_1}\delta x_1 + \frac{\partial\Pi}{\partial x_2}\delta x_2 + \ ... + \frac{\partial\Pi}{\partial x_n}\delta x_n = 0 \qquad (2.48)$$

In order to satisfy expression (2.48) for any arbitrary variation of x, it is necessary that partial derivatives $\frac{\partial\Pi}{\partial x_1}$ to $\frac{\partial\Pi}{\partial x_n}$ are all null. As this system can immediately be written in the form (2.18), it is adequate for direct application of the FEM.

For the solid mechanics problem, the finite element approximation of the potential function is,

$$\Pi = \frac{1}{2}\boldsymbol{X}^T \int_\Omega (\boldsymbol{D}^*\boldsymbol{U})^T \boldsymbol{k} (\boldsymbol{D}^*\boldsymbol{U})\, d\Omega\, \boldsymbol{X} - \boldsymbol{X}^T \int_\Omega \boldsymbol{U}^T \boldsymbol{b}\, d\Omega - \boldsymbol{X}^T \int_{\Gamma_\sigma} \boldsymbol{U}^T \boldsymbol{t}_\Gamma\, d\Gamma_\sigma \qquad (2.49)$$

where the first integral expression represents the stiffness matrix $\boldsymbol{K}$ and the remaining expressions give the equivalent nodal forces, simplifying (2.49) to,

$$\Pi = \frac{1}{2}\boldsymbol{X}^T\boldsymbol{K}\boldsymbol{X} + \boldsymbol{X}^T\boldsymbol{f} \qquad (2.50)$$

2.5 Error and convergence

The FEM is approximate in nature and the quality of its solution may result disappointingly low if its convergence properties are not well understood or appropriately handled. Consequently, the study of the quality of the solutions and of the means available to the analyst to improve it is an important issue in the FEM.

In essence, there are two methods capable of increasing the quality of the solutions obtained through the FEM:

- the h-refinement, that is based on the increase of the number of elements;
- the p-refinement, which consists of increasing the degree of the approximation functions.

The order of convergence (O), when the leading dimension of the element is reduced h times is can be determined by,

$$O = h^{p+1} \qquad (2.51)$$

where p is the largest degree of a complete polynomial used for the construction of the basis of the finite element.

For instance, if the approximation functions are linear ($p = 1$) and the leading dimension of the element is reduced to half, it should be expected that the errors would decrease roughly four times.

In complex engineering structures, it is generally computationally ineffective to use the same level of h-refinement throughout all of the structure. The h-refinement should thus be localized, that is, confined to areas where sudden variations of the unknown fields are expectable. A typical example is the stress concentration zones, such as those occurring around wedges, notches, cracks and localized applied loads.

The mesh refinement strategy holds several advantages over the alternative p-refinement such as its easy implementation, the possibility of performing localized refinements and the use of the same type of element in all of the mesh, which reduces the time spent on the element generation[1]. However, the convergence obtained by increasing the number of elements is typically lower than the convergence obtained by increasing the degree of the approximation functions.

In commercially available finite element software, the most broadly used method to increase the quality of a solution is the mesh refinement. Some software, however, also allow the analyst to choose between a (typically limited) number of elements with different p-refinements.

In order to achieve the convergence of a certain solution, obtained through the FEM, to the exact solution, there are two convergence criteria that must be fulfilled. The first criterion states that the finite element basis must be chosen such as to be able to represent exactly a rigid body displacement of the element, if such displacement is physically possible. Thus, for an element with N nodes,

$$\sum_{i=1}^{N} f_i(x) = 1 \qquad (2.52)$$

[1] Although the use of elements with different p-refinements in the same mesh is not theoretically impossible, the computational effort required for creating "connecting" elements hinders, in practice, localized p-refinement

that is, the shape functions $f_i(x)$ must form a partition of unity. The capacity of the element to recover rigid-body motion ensures that the FEM solution steadily converges to the exact solution as the element size is decreased and indeed recovers it exactly in the limit, when the element becomes a point (and thus the rigid-body displacement is its exact solution). The second criterion states that the displacement approximation functions must be chosen such that the deformations generated at the interface of two adjacent elements are finite.

In order to illustrate the relevance of the mesh refinement towards the achievement of satisfactory results, two numerical examples are presented next. The first example is an eigenmode analysis of a rectangular plate and the second example is a static analysis of a tension coupon with a circular hole in its center. In both examples, the analytic solution is available, which allows for a relevant analysis of the effect of the mesh refinement on the finite element solution. Both examples are implemented using the finite element software PATRAN and MSC.-NASTRAN.

a) Calculation of the eigenmodes of a rectangular plate

- Description of the problem

Consider the rectangular plate represented in Figure 2-4, constructed of aluminum and simply supported on all of its edges. The equation (2.53) providing the analytic solution of the first eigenfrequency was derived by Feldmann *et al.*(2009).

$$f = \frac{\alpha}{L^2}\sqrt{\frac{Et^3}{12\mu(1-\nu^2)}} \qquad (2.53)$$

where,

$$\begin{cases} \mu = \rho \cdot t \\ \alpha = 1{,}57(1+\lambda^2) \\ \lambda = \dfrac{L}{B} \end{cases} \qquad (2.54)$$

In the above equations, E is the Young's modulus, ν is the Poisson ratio, t stands for the thickness of the plate, ρ is the material density and L and B are the larger and smaller dimensions of the plate, respectively.

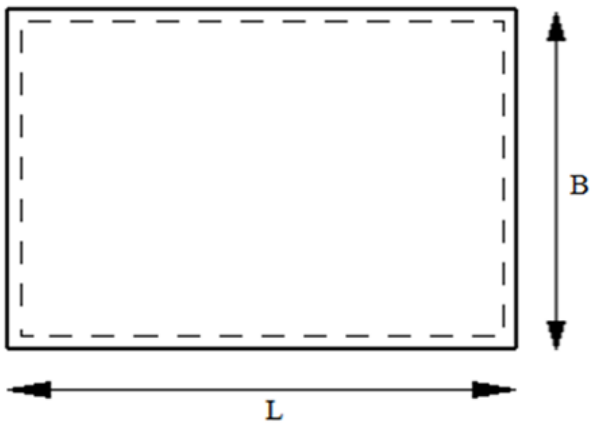

Figure 2-4 - Rectangular plate

- Testing setup

The Feldmann problem is solved next, using the data listed Table 1.

Dimensions and Properties	
L	1200 mm
B	800 mm
t	6.25 mm
E	68900 MPa
ν	0.33
ρ	27 kN/m^3

Table 1 - Dimensions and properties of the rectangular plate

Under these conditions, equation (2.53) yields a value of 33.868 Hz for the first eigenfrequency. To perform the finite element analysis, the plate is discretized using 4-node, 24 degrees-of-freedom (DOF) square shell elements available in MSC.-NASTRAN.

In order to assess the convergence to the analytic solution, the analysis is performed using elements with leading dimensions comprised between 2 and 40 cm.

- Finite element results

The deformed shapes corresponding to the first eigenmode and the respective eigenfrequencies are given in Table 2 for each of the analyzed situations.

Element dimension: 40 × 40 cm	**Element dimension: 20 × 20 cm**
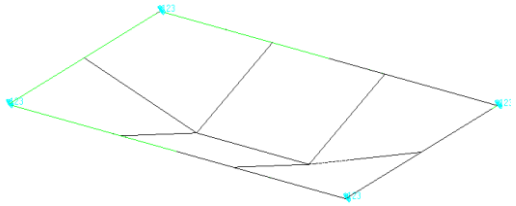	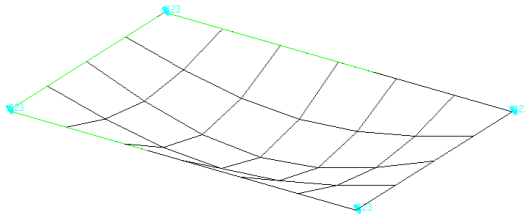
***f* = 29.29 Hz**	***f* = 32.546 Hz**
Element dimension: 10 × 10 cm	**Element dimension: 8 × 8 cm**
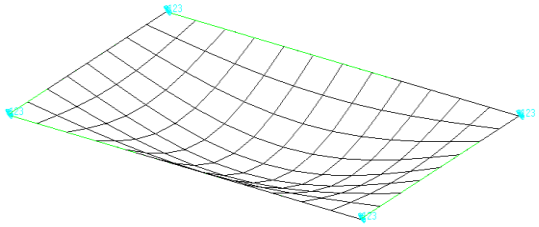	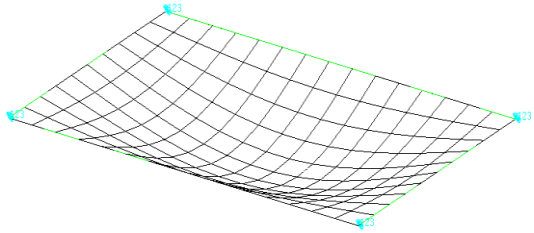
***f* = 33.445 Hz**	***f* = 33.567 Hz**
Element dimension: 4 × 4 cm	**Element dimension: 2 × 2 cm**
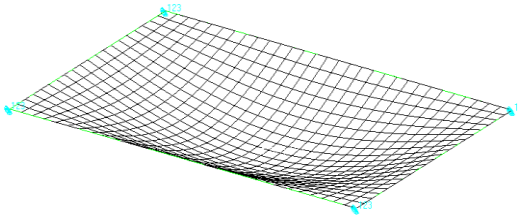	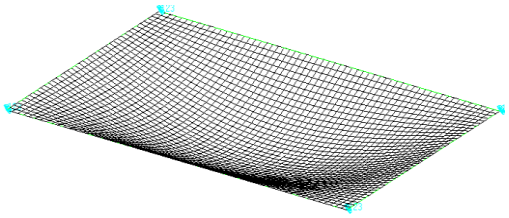
***f* = 33.756 Hz**	***f* = 33.81 Hz**

Table 2 - Deformed shape and eigenfrequency corresponding to the first eigenmode for different element dimensions

The effect of the mesh refinement procedure is clearly visible as the error decreases from 13.52% for the case of the coarsest mesh to 0.17% for the finest mesh. The price to be paid, however, is the computational effort, which increases exponentially with the total number of DOF, which ranges between 144 and 57600.

b) Static analysis of a tension coupon

- Description of the problem

Consider the tension coupon represented in Figure 2-5, constructed of aluminum, with a circular hole in its center and subjected to an edge load. The equation (2.55) providing the analytic solution of the maximum stress at the edge of the hole was derived by Pilkey & Pilkey (2008),

$$\sigma_{máx} = \sigma_n \, K_{tn} \qquad (2.55)$$

where K_{tn} is a stress concentration factor based on the net cross-sectional area, which can be graphically determined from a diagram given in Pilkey & Pilkey (2008), and σ_n is the normal stress based on net area,

$$\sigma_n = \frac{\mathrm{P}}{t(\mathrm{H} - \mathrm{D})} \qquad (2.56)$$

in which P is the external load (applied as a distributed force on the respective boundary), t is the thickness of the coupon, H stands for the width of the element and D for the diameter of the hole.

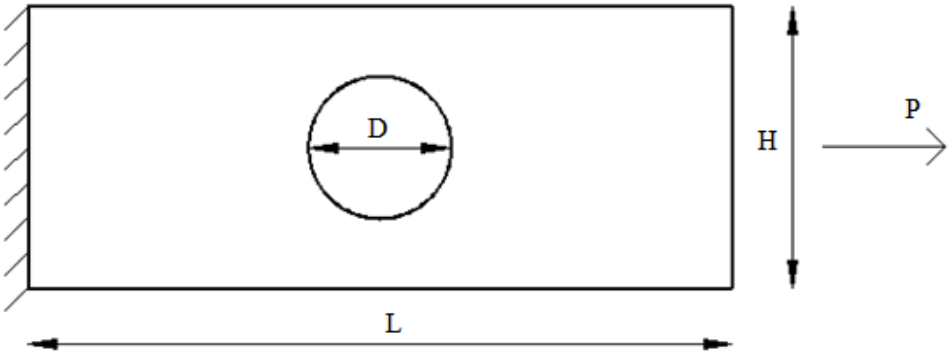

Figure 2-5 - Tension coupon

- Numerical setup

The theoretical solution of the maximum stress at the edge of the hole is obtained using the data listed in Table 3, and yields a value of 2170 kPa. The discretization of the plate is performed using square shell elements, the same type of elements as in the previous example.

Dimensions and Properties	
L	200 cm
H	80 cm
t	2,5 cm
E	68.9 GPa
ν	0,33
D	40 cm
P	10 kN

Table 3 - Dimensions and properties of the tension

To achieve the convergence to the analytic solution, the analysis is performed using points as mesh "seeds". By optimizing the number and position of these points, as well as the finite elements length, more accurate results are obtained.

- Finite element results

The stress diagrams and the values of the maximum stresses corresponding to the analyses performed with increasing number of elements are presented in Table 4. The orange areas of the stress diagrams represent the zones where the stress is larger, and the blue areas are the zone where the stresses are minor.

Number of elements: 32
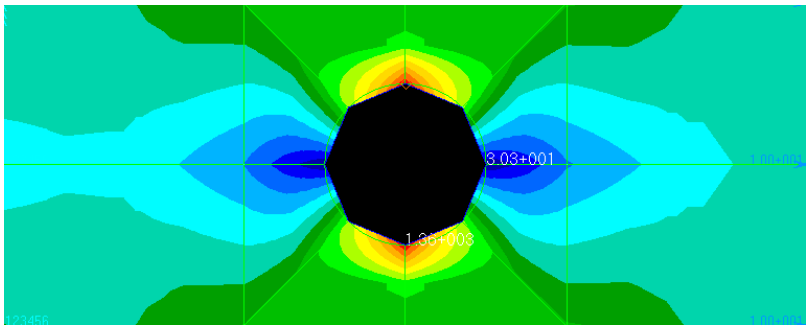 $\sigma_{máx} = 1362.88\ kPa$
Number of elements: 80
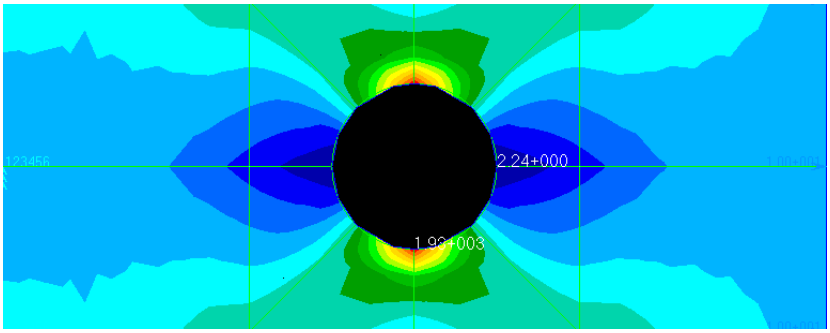 $\sigma_{máx} = 1936.39\ kPa$
Number of elements: 144
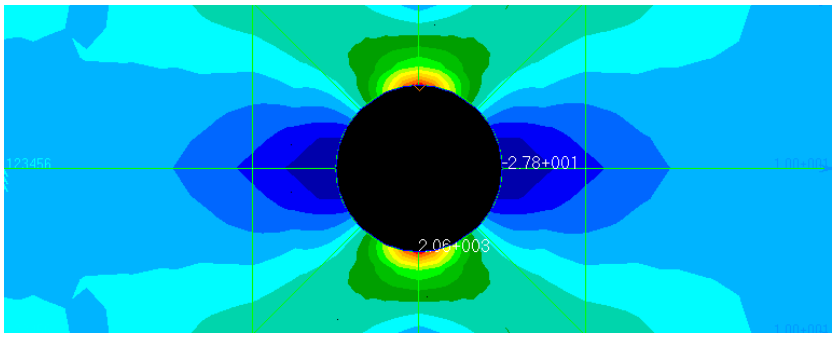 $\sigma_{máx} = 2062.47\ kPa$

Table 4 – von Mises stress diagram and maximum von Mises stress for increasing number of elements

Number of elements: 208
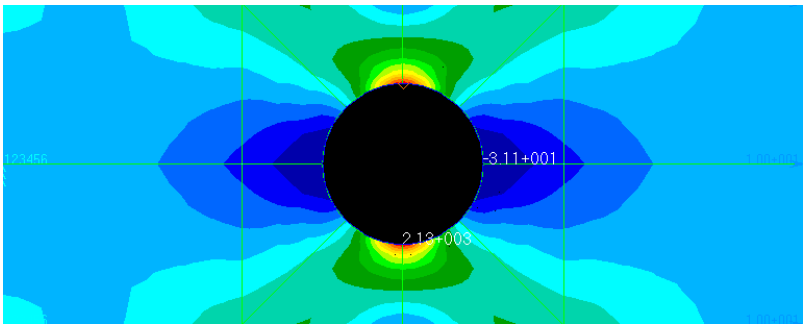 $\sigma_{máx} = 2135.30\ kPa$
Number of elements: 288
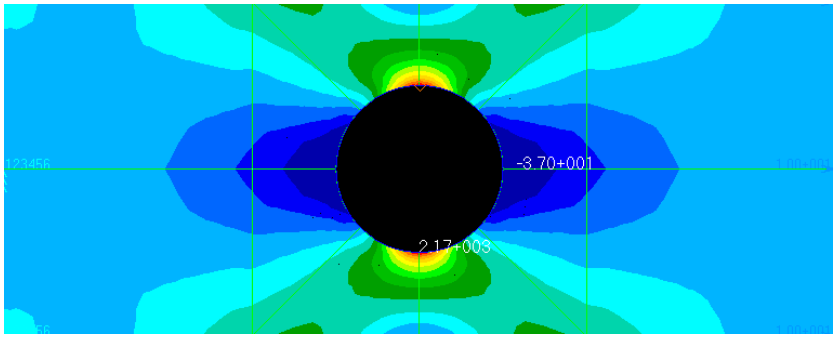 $\sigma_{máx} = 2164.70\ kPa$
Number of elements: 480
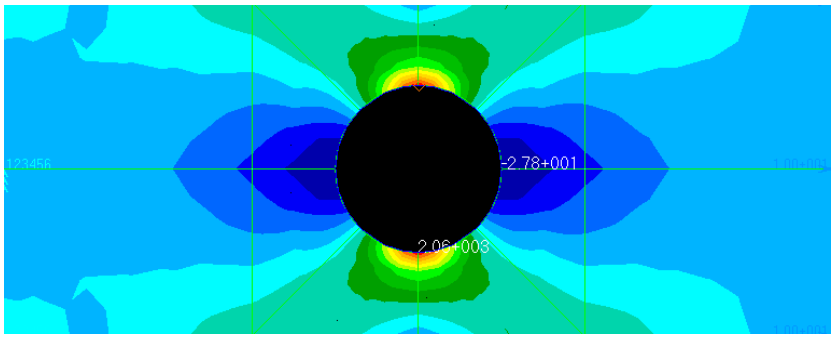 $\sigma_{máx} = 2171.60\ kPa$

Table 4(cont.) – von Mises stress diagram and maximum von Mises stress for increasing number of elements

The mesh refinement yields significant effects on the accuracy of the results, as the error decreases from 37.19% for the coarsest mesh, with 32 elements, to 0.074% for the finest mesh, with 480 elements. However, the number of DOF increases from 768 to 11520.

3. STRUCTURAL OPTIMIZATION

Many engineering problems involve structural optimization. Their goal is to satisfy certain requirements (e.g. limit state conditions) while minimizing certain quantities (e.g. resources spent) and maximizing others (e.g. structural safety). The requirements to satisfy are called restrictions and the functions to minimize/maximize are called objective functions. Optimization problems can be classified in three categories:

- Size optimization problems, which typically consist of the calibration of the cross sectional properties and dimensions of the structural elements. An example of a size optimization problem is the weight minimization of a truss structure by varying the cross-sectional areas of each element (Figure 3-1). The constraints are the allowable stress in all members and possibly, the displacements of selected nodes;

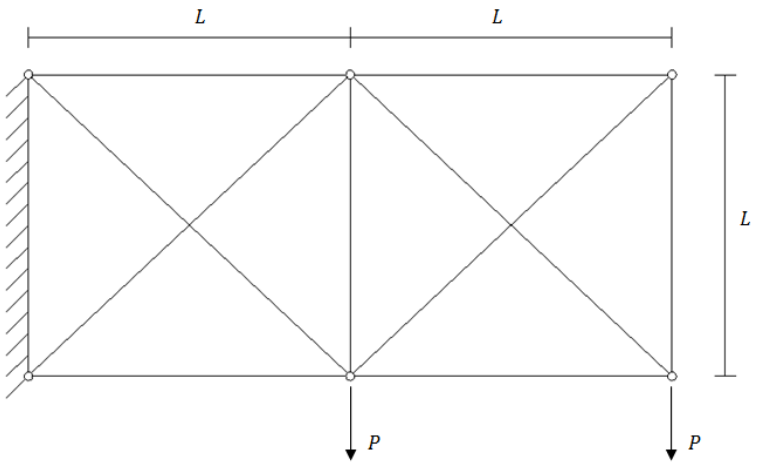

Figure 3-1 - Size optimization problem: ten-bar truss

- Shape optimization problems, which consist of the optimization of the boundary shape, generally used to reduce stresses or to make the stress distribution uniform with no increase of structural weight. An example of such problem is the shape optimization of the Michell's arch[2] to achieve weight minimization by varying the coordinates of the nodes, with a displacement constraint at the loaded node;

[2] Structure named in honor of Anthony George Maldon Michell, an Australian mechanical engineer who played an important role in the development of structural optimization by publishing in 1904, his work "*The limits of economy of material in frame structures"*.

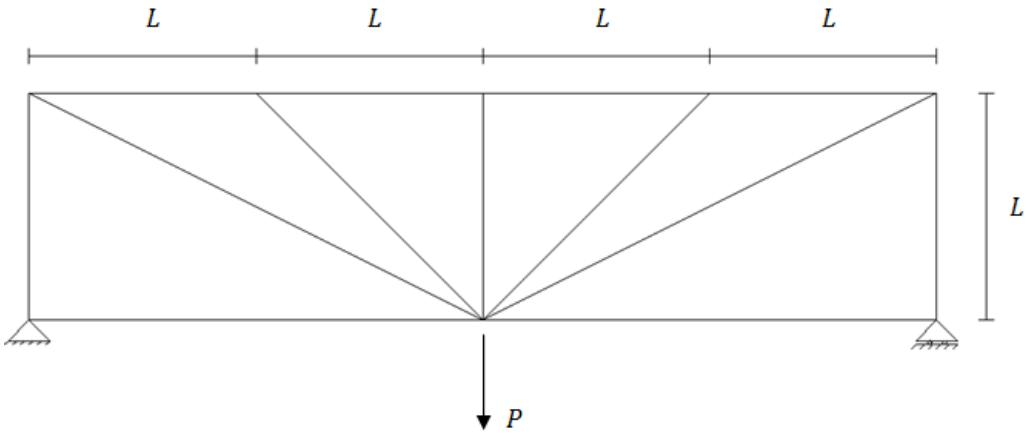

Figure 3-2 - Shape optimization problem – Michell's arch shape optimization

- Topology optimization problems, in which the goal is to determine the optimal distribution of material, given the design space, boundary conditions, loads and required design performance. An example of topology optimization problem is the optimization of a bicycle frame (Figure 3-3). The design process starts from the definition of a design area domain (the left-hand-side of Figure 3-3) and evolves towards the optimized material distribution (the right-hand-side of the same Figure), observing, at all times, a range of strength and displacement constraints.

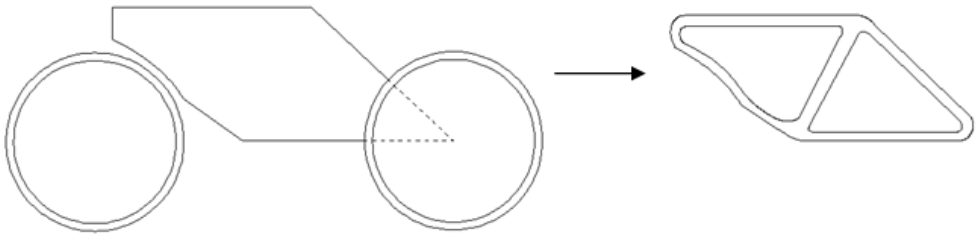

Figure 3-3 - Topology optimization problem: bicycle frame topology optimization

Some key numerical methods to find extrema of functions (which constitute an essential part of all structural optimization procedures), are introduced in the next Section. The general description of the methods is followed by their application to two optimization problems from the engineering practice.

3.1 Introduction to the minimization[3] of functions

Given a function $f(\boldsymbol{x})$ of N variables, the main objective of a generic minimization problem is to find the values of all variables ($\boldsymbol{x}$), that correspond to a minimum of $f(\boldsymbol{x})$. Besides this primary objective, the minimization method should be computationally fast, consume limited resources and accommodate additional constraints applied on the function's variables.

The minimization methods presented in this Section are aimed at identifying local, rather than global minima of functions. A global minimum is defined as the lowest value of the function on a search interval, while a local minimum stands for the lowest value of the function in a finite neighborhood, but not necessarily on the entire search interval. It is important to note that both minima may either correspond to a null gradient point or be on the interval's boundary. Clearly, finding the global minimum generally yields better practical results than local minimum. However, as many methods of finding the global minimum are simply based on comparing local minima, only the latter will be treated here.

Relative to the constraints posed on the function's variables, the minimization problem may be unconstrained or constrained. The unconstrained minimization is used when no constraints are applied on the variables, while the constrained minimization occurs when restrictions are enforced on the variables. Within the constrained type of minimization, there are three different types to be considered:

- Simple: the restrictions are simply used to limit a search interval;
- Linear programming: the constraints are linear functions of the same variables;
- Higher degree programming: the constraints are higher degree functions of the same variables.

Except for some particularly simple cases, determining analytically extrema of functions is not a straightforward task, so numerical methods are typically used instead. A classification of some of the most common methods for functions minimization is given next. For functions of a single variable (1D minimization), the methods can be classified as:

- Methods that do not require computation of derivatives:
    - The Golden Search method
    - The Brent method
- Method that do require the computation of derivatives:
    - The Brent method, modified

[3] It should be noted that the extremum-finding methods described in this section are invariant to whether the extremum is a minimum or a maximum. For simplicity and without lack of generality, minimum extrema are adopted in this presentation.

For functions of N variables, the methods presented here are:

- Methods that do not require computation of gradients:
  - The Downhill Simplex method
  - The Powell method
- Methods that do require computation of gradients:
  - Conjugate gradient methods (Fletcher-Reeves, Polak-Ribiere)
  - Quasi-Newton methods (Davidon-Fletcher-Powell, Broyden-Fletcher-Goldfarb-Shanno)

  All these methods are briefly described in the next sections.

3.2 One-dimensional minimization (unconstrained)

3.2.1 Golden search method

This method is one of the simplest minimum-finding methods, although not very fast in convergence. Employed to search for the minimum value of a continuous function, the method starts with the calculation of 3 abscissas (the bracketing points $a < b < c$) such that,

$$\begin{cases} f(a) > f(b) \\ f(c) > f(b) \end{cases}$$

After this, a new sampling point (d) is chosen between b and the furthest away limit of the bracketing interval (L_1). Then, based on the value of the function in the bracketing points, one of them is discarded by the following procedure:

- If $f(d) > f(b) \rightarrow a \equiv d$ (Figure 3-4)
- Else $\begin{cases} c \equiv b \\ b \equiv d \end{cases}$ (Figure 3-5)

These criteria ensure that the minimum is, at all times, inside the bracketing interval. The point-discarding process described above repeats itself and allows for a gradual narrowing of the searching interval, until it becomes smaller than a tolerance, never inferior to $\sqrt{\varepsilon}$, being ε the machine precision.

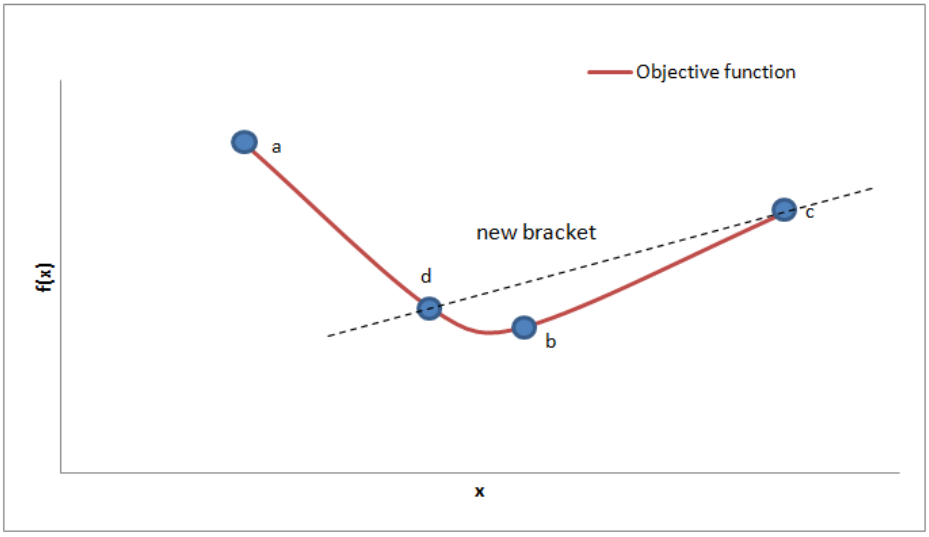

Figure 3-4 - Bracketing interval when f(d)>f(b)

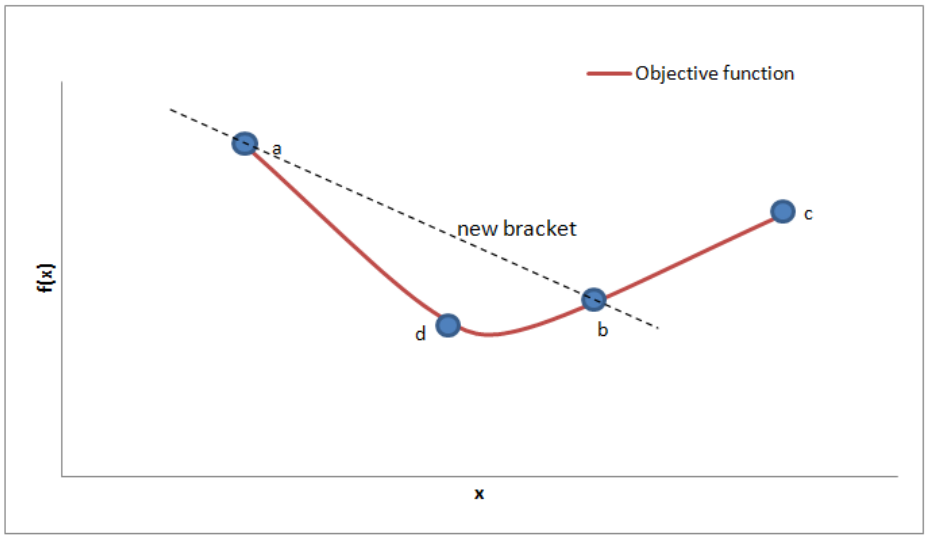

Figure 3-5 - Bracketing interval when f(d)<f(b)

Although slow, in general, the convergence of the method can be improved by taking the new sampling point (*d*) such that the length between *b* and *d* is given by $w \cdot L_1$, being *w* the golden ratio[4] 0.38197, and L_1 the distance between *b* and the furthest away point of the bracketing interval.

[4] This number, along with 0,61803, are well-known for their importance in the old Greek architecture. Buildings with the dimensions related through these constants were considered aesthetically pleasing.

3.2.2 Brent's method in 1D

This method is the most effective when the objective function´s behavior near its minimum is smooth and hence is possible to use a parabola to approximate the function. Just as in the Golden Search method, the starting point of the Brent's method involves the definition of three (bracketing) points. However, unlike the Golden Search method, the bracketing points are used to create an interpolating parabola. It is possible to prove that the extremum of this parabola is located at:

$$x = b - \frac{1}{2}\left(\frac{(b-a)^2[f(b)-f(c)] - (b-c)^2[f(b)-f(a)]}{(b-a)[f(b)-f(c)] - (b-c)[f(b)-f(a)]}\right) \qquad (3.1)$$

The process is illustrated in Figure 3-6. In the first iteration, the parabola passes through the first three bracketing points 1-2-3, and has an extremum at point 4. The second iteration uses the new bracketing interval obtained from the first interval by discarding the abscissa corresponding to the largest function value. In the case presented in Figure 3-6, the new parabola will thus pass through points 1, 2 and 4.

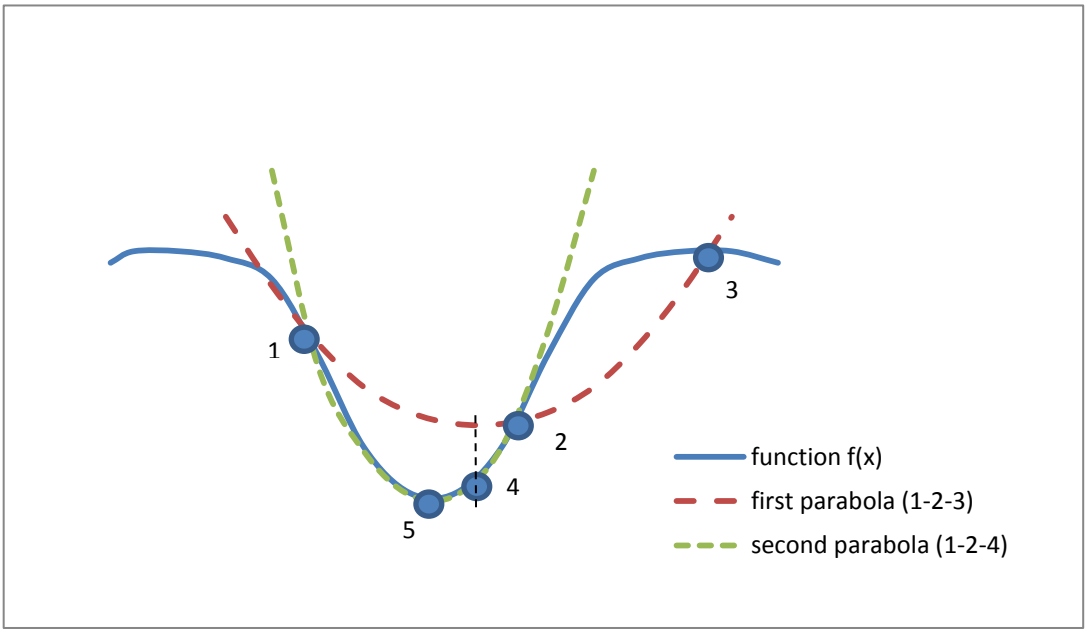

Figure 3-6 - Approximation of a function's minimum according to Brent's method

Although this method provides quadratic convergence, it has certain disadvantages when compared to the golden ratio method, such as the possibility of having iterations that yield maxima instead of minima, or the numerical problems encountered when approaching the

extremum. This last issue is caused by the instability of equation (3.1), as the method gets closer to the extremum, due to the decreasing distance between the interpolation points.

3.2.3 Brent's method, with first derivates

When information about the function's first derivative is available, it must be handled with care. Indeed, the two most obvious strategies may be problematic at a deeper consideration:

- The elaboration of a numerical root-finding algorithm to find the root of the function's derivative, using only derivative information, has problems related to the issue of distinguishing between a maximum and a minimum and to the fact that the derivative in an outer point of the bracketing interval points to the exterior of this interval.
- The construction of a higher-degree polynomial approximation of the function, using the information on the function and derivative's values, although sometimes adequate, may amplify the numerical errors when the bracketing interval decreases.

Instead of using the ideas presented above, the modified Brent's method evaluates the derivative of the function in the middle of the bracketing interval in order to establish if the next bracketing point should lay on the left or the right side of the interval. Then, as shown in Figure 3-7, this derivative and the derivative of the second-best bracketing point so far (a) are interpolated to zero and the new point (d) that results from this interpolation is included in the new bracketing interval. However, if the new point is not consistent with the side of the interval it should lay into (between points a and b), the new point is dropped and substituted by point d', chosen in the middle of the "correct" region, as shown in Figure 3-8.

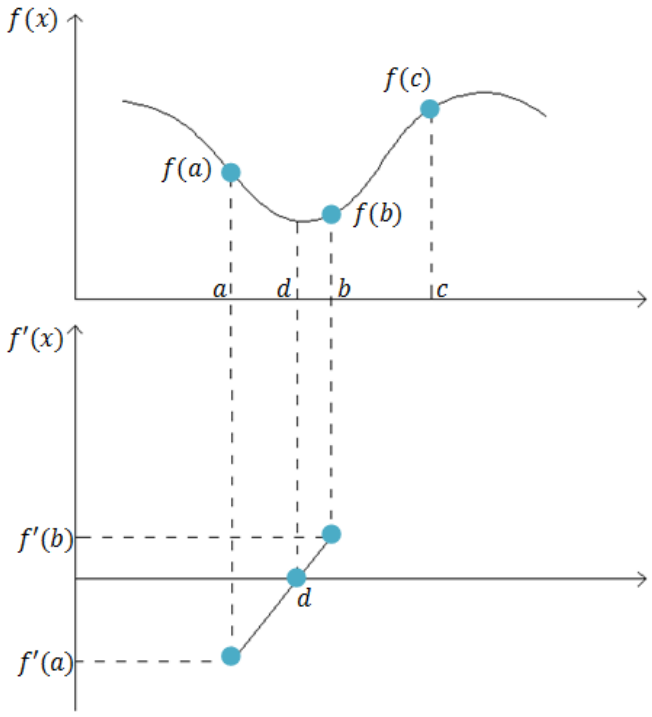

Figure 3-7 - Linear interpolation yields a new bracketing point (d) in the acceptable region of the bracketing interval

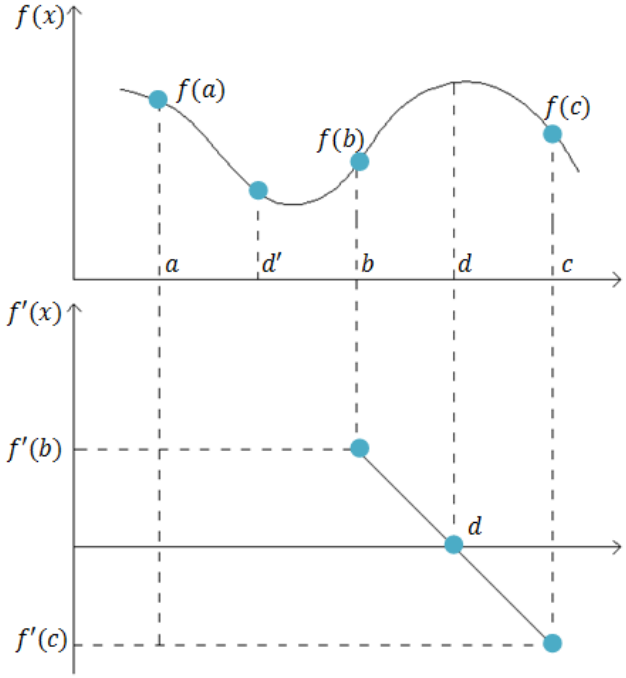

Figure 3-8 - Linear interpolation yields a new bracketing point (d) in the unacceptable region of the bracketing interval

3.3 Multi-dimensional minimization (unconstrained)

3.3.1 Downhill simplex method

This minimization method uses a simplex, defined as a geometrical figure with N+1 points and all of their interconnecting lines and surfaces, where N is the dimension of the space the function is defined on. The simplex is constructed by taking one initial arbitrary point ($\boldsymbol{P_0}$) and one arbitrary side length (λ), from which it is possible to generate the remaining simplex points as,

$$\boldsymbol{P_i} = \boldsymbol{P_0} + \lambda \boldsymbol{e_i} \qquad (3.2)$$

where e_i stands for the versor of each one of the N directions in the function's space.

The downhill simplex method uses the simplex to evaluate the objective function at each node of the figure, in order to identify the node that corresponds to the highest value of the function. Once this point is found, a new trial point is obtained as the "symmetric" of the largest-valued point on the other side of the simplex. This procedure is called "reflection" and is illustrated in Figure 3-9. After the reflection, a new function evaluation takes place at the new point and if the new value is lower than the previous highest one, the previous point is discarded and a new simplex is constructed using the new point. Conversely, if the new point corresponds to a value larger than the largest of the previous simplex, the new point is discarded and a new trial point is defined on the same vertex, but closer to the center of the simplex. This procedure is called "contraction". (Press *et al.*, 1992)

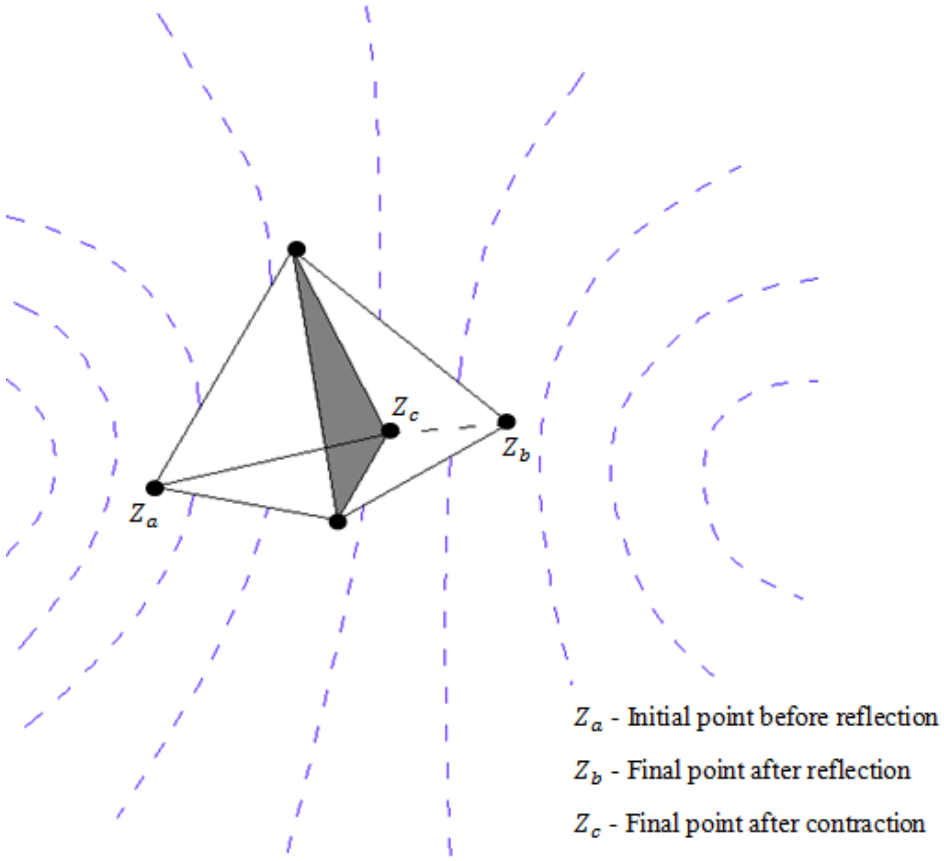

Figure 3-9 - "Reflection" and “contraction” of the highest value point from the initial simplex in a valley simulated by the blue dashed lines

Although this method does not require the use of derivatives, many evaluations may be needed at every iteration for the simplex to approach the minimum. On the other hand, the method is remarkably robust and particularly efficient for functions with unstable behavior.

It is important to note that this method is the only N-dimension minimization technique that does not use 1-dimension minimization as its basis.

3.3.2 Powell’s method

Powell’s method is a numerical technique for unconstrained minimization that does not require the calculation of derivatives and consists of sequences of 1-dimension minimizations.

The method uses a sequential minimization of the function, which takes place in different directions:

- The function is minimized in an arbitrary direction (*x*);

- Taking the minimum found in the *x* direction as a new starting point, the function is now minimized in another direction (*y*);
- This process repeats itself until the function's minimum is found.

Obviously, this method requires the availability of a line-minimization algorithm, to take as input an arbitrary initial position vector $\boldsymbol{P}$ and the minimization direction versor $\boldsymbol{n}$, and to output the function's minimum in the **n** direction,

$$\boldsymbol{P_{min}} = \boldsymbol{P} + \lambda \boldsymbol{n} \tag{3.3}$$

Depending on the adopted line minimization technique, the method may reach quadratic convergence (Chapra & Canale, 2006). The fact that it does not necessarily require the evaluation of function's derivatives is also an advantage. However, the method may require a very large number of iterations to converge when the minimization directions correspond to the directions of the referential and the function is characterized by a long narrow valley, not aligned to any of the axes. The reason for this is that the minimization of the function in one direction generally compromises anterior minimizations in orthogonal directions, leading to the necessity of restoring the minima in the anterior directions and the process repeats itself.

To avoid this issue, it is desirable to identify some directions that do not interfere with each other, so that the minimization along one is not hindered by the minimization along the other. These are called "conjugate directions" and their theory is briefly reviewed in the next Section.

3.3.3 Conjugate directions

Consider the expansion in Taylor series of a function $f(\boldsymbol{x})$: $\mathbb{R}^N \longrightarrow \mathbb{R}$, around a point $\boldsymbol{P}$,

$$f(\boldsymbol{P} + \boldsymbol{x}) = f(\boldsymbol{P}) + \sum_{i=1}^{N} \frac{\partial f(\boldsymbol{P})}{\partial x_i} x_i + \frac{1}{2} \sum_{\substack{i=1 \\ j=1}}^{N} \frac{\partial^2 f(\boldsymbol{P})}{\partial x_i \partial x_j} x_i x_j \tag{3.4}$$

which can be written in the equivalent matrix form:

$$f(\boldsymbol{P} + \boldsymbol{x}) = c - \boldsymbol{b}\boldsymbol{x} + \frac{1}{2} \boldsymbol{x}^T \boldsymbol{A} \boldsymbol{x} \tag{3.5}$$

where

$$\boldsymbol{b} = -\nabla f(\boldsymbol{P}) \tag{3.6}$$

$$c = f(\boldsymbol{P}) \tag{3.7}$$

and $\boldsymbol{A}$ is the Hessian matrix of the function, computed in point $\boldsymbol{P}$.

Consider next the Taylor series expansion of the gradient of the function $f(\boldsymbol{x})$. The derivative of the function in a generic direction x_i is,

$$\frac{\partial f(\boldsymbol{P}+\boldsymbol{x})}{\partial x_i} = \frac{\partial f(\boldsymbol{P})}{\partial x_i} + \sum_{j=1}^{N} \frac{\partial^2 f(\boldsymbol{P})}{\partial x_i \partial x_j} x_j \qquad (3.8)$$

and applying the same procedure for all directions *i*,

$$\boldsymbol{\nabla} f(\boldsymbol{P}+\boldsymbol{x}) = \boldsymbol{\nabla} f(\boldsymbol{P}) + \boldsymbol{A}\boldsymbol{x} \qquad (3.9)$$

Using expression (3.6), result (3.9) is put in the form,

$$\boldsymbol{\nabla} f(\boldsymbol{P}+\boldsymbol{x}) = \boldsymbol{A}\boldsymbol{x} - \boldsymbol{b} \qquad (3.10)$$

From result (3.10), it follows that the change of the gradient when one successively moves from point $\boldsymbol{P}$ in directions $\boldsymbol{u}$ and $\boldsymbol{v}$ (not necessarily orthogonal) is,

$$\boldsymbol{\nabla} f(\boldsymbol{P}+\boldsymbol{u}+\boldsymbol{v}) - \boldsymbol{\nabla} f(\boldsymbol{P}+\boldsymbol{u}) = \boldsymbol{A}(\boldsymbol{u}+\boldsymbol{v}) - \boldsymbol{A}\boldsymbol{u} = \boldsymbol{A}\,\boldsymbol{v} \qquad (3.11)$$

The necessary and sufficient condition for this change not to be affected by a subsequent minimization in direction $\boldsymbol{w}$ is for the vector $\boldsymbol{w}$ to be orthogonal to the anterior change of gradient,

$$\boldsymbol{w}^T\left(\boldsymbol{\nabla} f(\boldsymbol{P}+\boldsymbol{u}+\boldsymbol{v}) - \boldsymbol{\nabla} f(\boldsymbol{P}+\boldsymbol{u})\right) = \boldsymbol{w}^T\boldsymbol{A}\,\boldsymbol{v} = 0 \qquad (3.12)$$

When the condition (3.12) is satisfied for two direction vectors, they are labeled conjugate directions. When this condition is satisfied for a whole vector set, a conjugate set is obtained.

The minimization along a set of conjugate directions lifts the necessity of performing various passages through each direction, requiring only one passage through all *N* directions, if the analyzed function is a quadratic form, that is, if the expression (3.5) is exact. If the Taylor expansion is not exact, more iterations will be needed, but the convergence is still generally much faster than that of the Powell's method.

The efficient construction of conjugate directions is important as it may be the most computationally demanding process in the conjugate gradient methods. To obtain conjugate directions it is necessary to consider, first, an arbitrary initial vector, $\boldsymbol{u_0}$, and to create a set of vectors, $\boldsymbol{u_i}$, such that the expression (3.12) is verified for any pair of these vectors,

$$\boldsymbol{u_i}\,\boldsymbol{A}\,\boldsymbol{u_j} = 0 \text{ , for any } i \neq j \qquad (3.13)$$

Application of definition (3.13) for computing the conjugate directions involves the computation of the Hessian matrix, which is generally difficult to accomplish. Therefore, it is

important to recover the conjugate directions without knowledge of the Hessian matrix. This is only practically achievable in an exact manner for quadratic functions. However, the method used to do so produces good approximations of the conjugate directions even when the function is relatively far from quadratic. Starting with a direction vector $\boldsymbol{u_0}$ and an auxiliary vector $\boldsymbol{v_0} = \boldsymbol{u_0}$, the method successively constructs the recursive sequence,

$$\begin{cases} \boldsymbol{u_{i+1}} = \boldsymbol{v_{i+1}} + \vartheta_i \boldsymbol{u_i} \\ \boldsymbol{v_{i+1}} = \boldsymbol{v_i} - \lambda_i \boldsymbol{A u_i} \end{cases} \tag{3.14}$$

where,

$$\begin{cases} \vartheta_i = \dfrac{\boldsymbol{v_{i+1}^T v_{i+1}}}{\boldsymbol{v_i^T v_i}} \\ \lambda_i = \dfrac{\boldsymbol{v_i^T v_i}}{\boldsymbol{u_i A u_i^T}} \end{cases} \tag{3.15}$$

It can be shown that vectors $\boldsymbol{v_i}$ and $\boldsymbol{u_i}$ satisfy the following orthogonality conditions:

$$\begin{cases} \boldsymbol{v_i^T u_j} = 0 \\ \boldsymbol{v_i^T v_j} = 0 \\ \boldsymbol{u_i^T A\, u_j} = 0 \end{cases} \tag{3.16}$$

Consequently, if the Hessian matrix was known, it would be possible, by the application of (3.14) and (3.15), to construct the sequence of conjugate directions $\boldsymbol{u_i}$. However, as the Hessian matrix is not known, an alternative approach must be identified. Consider now that the auxiliary vectors $\boldsymbol{v_i}$ are defined as the gradient of the function in the current point $\boldsymbol{P_i}$,

$$\boldsymbol{v_i} = -\boldsymbol{\nabla} f(\boldsymbol{P_i}) \tag{3.17}$$

Now, by the application of the equation (3.10), the function's gradient computed in a point $\boldsymbol{P_{i+1}}$ located at a distance λ along a direction $\boldsymbol{u_i}$ is,

$$-\boldsymbol{\nabla} f(\boldsymbol{P} + \lambda \boldsymbol{u_i}) = \boldsymbol{A\, u_i}\, \lambda - \boldsymbol{v_i} \tag{3.18}$$

Setting λ as the distance between the initial considered point and the minimum in direction $\boldsymbol{u_i}$, and defining

$$\boldsymbol{v_{i+1}} = -\boldsymbol{\nabla} f(\boldsymbol{P} + \lambda \boldsymbol{u_i}) \tag{3.19}$$

equation (3.18) is identical to the second equation of system (3.14). Through this method, it is therefore possible to construct the sequence of vectors $\boldsymbol{u_i}$ without any knowledge on the Hessian matrix.

Concluding, considering an arbitrary initial point $\boldsymbol{P_0}$, the procedure to obtain the conjugate directions is based on the following steps:

- Obtain the function's gradient in $\boldsymbol{P_0}$ and set $\boldsymbol{v_0} = \boldsymbol{u_0} = -\boldsymbol{\nabla} f(\boldsymbol{P_0})$;
- Find the function's minimum point, $\boldsymbol{P_1}$, along direction $\boldsymbol{u_0}$, setting λ_0 as the distance between $\boldsymbol{P_1}$ and $\boldsymbol{P_0}$;
- The gradient of the function in the point $\boldsymbol{P_1}$ is $-\boldsymbol{v_1}$;
- Compute ϑ_i from (3.15);
- Apply relation (3.14) to obtain $\boldsymbol{u_1}$;
- Repeat the procedure.

3.3.4. Gradient methods

As opposed to the Downhill Simplex method and Powell's method, gradient methods require the computation of the function's gradient. The gradient methods introduced in this section are:

- The steepest descent method;
- Conjugate gradient methods:
  - The Fletcher-Reeves method;
  - The Polak-Ribiere method.

The gradient of a function in a given point is the direction of the steepest descent of the function. This is the basis of the steepest descent method. According to this method and considering an initial arbitrary point $\boldsymbol{P_i}$, the next iteration point $\boldsymbol{P_{i+1}}$ is obtained by minimizing the function along the local downhill gradient in point $\boldsymbol{P_i}$, $-\boldsymbol{\nabla} f(\boldsymbol{P_i})$. Although the first iteration uses an optimal minimization direction indeed, the following iterations do not. Therefore, many iterations may be needed to converge when the function is characterized by a long narrow valley. As each component of the function's gradient takes as much time to compute as a function evaluation, the steepest descent method may sometimes prove to be a slow convergence method, and consequently is rarely used.

Alternatively, the procedure presented in Section 3.3.3. can be used to compute the conjugate directions and the successive minimizations can be performed along those. This is the strategy used by all conjugate gradient methods, of which Fletcher-Reeves and Polak-Ribiere methods are briefly presented next.

According to the Fletcher-Reeves method, from an initial point $\boldsymbol{P_i}$, the minimum point, $\boldsymbol{P_{i+1}}$, is found along the function's gradient direction, setting λ_i as the length between the starting and the minimum points, and $\boldsymbol{v_{i+1}}$ as the function's gradient in point $\boldsymbol{P_{i+1}}$, $\boldsymbol{v_{i+1}} = -\boldsymbol{\nabla} f(\boldsymbol{P_{i+1}})$. The computation of the new search direction is given by,

$$\boldsymbol{u_{i+1}} = \boldsymbol{v_{i+1}} + \vartheta_i \boldsymbol{u_i} \qquad (3.14)$$

where,

$$\vartheta_i = \frac{\boldsymbol{v}_{i+1}^T \boldsymbol{v}_{i+1}}{\boldsymbol{v}_i^T \boldsymbol{v}_i} \tag{3.15}$$

The Fletcher-Reeves method yields the exact minimum in a single step when the objective function is a quadratic form. On the other hand, when used on non-quadratic functions, the method loses accuracy and the minimum-finding process may take much more iterations.

The Polak-Ribiere method is aimed at correcting the Fletcher-Reeves slow convergence issue for non-quadratic functions by slightly altering equation (3.15) to,

$$\vartheta_i = \frac{(\boldsymbol{v}_{i+1}^T - \boldsymbol{v}_i^T)\boldsymbol{v}_{i+1}}{\boldsymbol{v}_i^T \boldsymbol{v}_i} \tag{3.20}$$

According to (3.16), $\boldsymbol{v}_i^T \boldsymbol{v}_{i+1} = 0$ when the function is precisely quadratic. Therefore, the Polak-Ribiere and Fletcher-Reeves methods yield identical results for quadratic functions. As the functions are generally not exactly quadratic, however, relation (3.16) is not exactly satisfied and the Polak-Ribiere and Fletcher-Reeves methods yield different results (Chong & Zak, 2001). In such situations, the use of definition (3.20) rather than (3.15) may reduce significantly the number of iterations required for full convergence to the function's minimum.

3.3.5. Quasi-Newton methods

The quasi-Newton methods are techniques capable of good performances on the minimization of quadratic and smooth non-quadratic functions. They make direct use of the Hessian matrix, which is iteratively approximated to avoid its explicit calculation (Chapra & Canale, 2006). As for the conjugate gradient methods, the minimum of a function $f(\boldsymbol{x}): \mathbb{R}^N \longrightarrow \mathbb{R}$ is obtained in precisely N steps if the function is quadratic, or a quadratic convergence is recovered if the function is not quadratic.

Quasi-Newton methods, start from an initial point $\boldsymbol{x_i}$, where the function's gradient is known. A new point, $\boldsymbol{x_{i+1}}$, is subsequently found such that the gradient in this new point is null. Thus, by application of expression (3.10),

$$\boldsymbol{\nabla} f(\boldsymbol{x_{i+1}}) = \boldsymbol{A}(\boldsymbol{x_{i+1}} - \boldsymbol{x_i}) + \boldsymbol{\nabla} f(\boldsymbol{x_i}) = \boldsymbol{0} \tag{3.21}$$

from which,

$$\boldsymbol{x_{i+1}} - \boldsymbol{x_i} = -\boldsymbol{A}^{-1} \boldsymbol{\nabla} f(\boldsymbol{x_i}) \tag{3.22}$$

There are, however, two main problems concerning the enforcement of equation (3.22). The first problem is that the Hessian matrix is practically unaffordable to calculate. The second issue is that the method needs a mechanism to ensure the recovery of a function minimum

instead of a maximum. The first issue is overcome by approximating, rather than computing, the inverse of the Hessian matrix as,

$$\lim_{i\to\infty} \boldsymbol{H_i} = \boldsymbol{A^{-1}} \tag{3.23}$$

Although the approximation $\boldsymbol{H_i}$ is not exactly $\boldsymbol{A^{-1}}$ after N iterations, the difference between the both endows the method with a mechanism to control the direction of the iterative process and therefore to ensure that the new point is a minimum and not a maximum. The condition for the function to descend in a given direction, $\boldsymbol{x_{i+1} - x_i}$, is,

$$\boldsymbol{\nabla f^T(x_i)(x_{i+1} - x_i) = (x_{i+1} - x_i)^T \nabla f(x_i) < 0} \tag{3.24}$$

Using (3.22), expression (3.24) becomes,

$$\boldsymbol{\nabla f^T(x_i)(x_{i+1} - x_i)^T = -(x_{i+1} - x_i)^T \mathbf{A}\,(x_{i+1} - x_i) < 0} \tag{3.25}$$

The condition (3.25) is only satisfied independently of the point if the matrix **A** is positive definite. However, if analyzing far from minimum, there is no guarantee that the Hessian is positive definite. To overcome this issue, it is possible to choose the Hessian approximation such that the positive-definiteness condition is accomplished at every iteration. Such approximation is achievable using different algorithms, such as the Davidson-Fletcher-Powell (DFP) and the Broyden-Fletcher-Goldfarb-Shanno (BFGS) algorithms.

The DFP approximation technique defines the inverse Hessian approximation as,

$$\boldsymbol{H_{i+1} = H_i + \frac{(x_{i+1} - x_i) \otimes (x_{i+1} - x_i)}{(x_{i+1} - x_i)(\nabla f(x_{i+1}) - \nabla f(x_i))} - \frac{\left[H_i\left(\nabla f(x_{i+1}) - \nabla f(x_i)\right)\right] \otimes \left[H_i\left(\nabla f(x_{i+1}) - \nabla f(x_i)\right)\right]}{\left(\nabla f(x_{i+1}) - \nabla f(x_i)\right) H_i \left(\nabla f(x_{i+1}) - \nabla f(x_i)\right)}} \tag{3.26}$$

where $\otimes$ stands for the "outer" product of two vectors.

The BFGS approximation method has exactly the same formula as the DFP method, with one additional term,

$$\boldsymbol{\ldots + \left[\left(\nabla f(x_{i+1}) - \nabla f(x_i)\right) H_i \left(\nabla f(x_{i+1}) - \nabla f(x_i)\right)\right] m \otimes m} \tag{3.27}$$

where $\boldsymbol{m}$ is the vector,

$$\boldsymbol{m} = \frac{(\boldsymbol{x_{i+1}} - \boldsymbol{x_i})}{(\boldsymbol{x_{i+1}} - \boldsymbol{x_i})\big(\boldsymbol{\nabla} f(\boldsymbol{x_{i+1}}) - \boldsymbol{\nabla} f(\boldsymbol{x_i})\big)} - \frac{\boldsymbol{H_i}\big(\boldsymbol{\nabla} f(\boldsymbol{x_{i+1}}) - \boldsymbol{\nabla} f(\boldsymbol{x_i})\big)}{\big(\boldsymbol{\nabla} f(\boldsymbol{x_{i+1}}) - \boldsymbol{\nabla} f(\boldsymbol{x_i})\big)\boldsymbol{H_i}\big(\boldsymbol{\nabla} f(\boldsymbol{x_{i+1}}) - \boldsymbol{\nabla} f(\boldsymbol{x_i})\big)} \tag{3.28}$$

Although both conjugate gradient and quasi-Newton methods require the computation of the function's gradient, the difference between them relies on the fact that the quasi-Newton methods store and accumulate the information on the computation of the gradient at arbitrary points. Despite this difference, there is not any substantial advantage that the quasi-Newton methods have over the conjugate gradient methods. However, the quasi-Newton methods are historically older and hence more widely understood, controlled and used in numerical algorithms.

3.4 Restricted optimization: linear programming

Practical engineering problems are generally characterized by the minimization or maximization of some objective function subjected to various types of constraints. When both the objective function and the constraints applied to it are linear, the problem is a linear programming problem, whose generic definition is: find N independent variables $x_1, x_2, \dots, x_N$ that maximize[5] the objective function (Chong & Zak, 2001),

$$z = a_{0_1}x_1 + a_{0_2}x_2 + \cdots + a_{0_N}x_N \qquad (3.29)$$

subjected to the primary constraints,

$$x_1 \geq 0,\ x_2 \geq 0, \qquad \dots\ x_N \geq 0 \qquad (3.30)$$

and to $M = m_1 + m_2 + m_3$ secondary constraints defined as,

$$\begin{cases} a_{i1}x_1 + a_{i2}x_2 + \cdots + a_{iN}x_N \leq b_i \ \ (b_i \geq 0) \\ a_{j1}x_1 + a_{j2}x_2 + \cdots + a_{jN}x_N \geq b_j \ \ (b_j \geq 0) \\ a_{k1}x_1 + a_{k2}x_2 + \cdots + a_{kN}x_N = b_k (b_k \geq 0) \end{cases} \qquad (3.31)$$

It should be noted that the positiveness constraints applied on b_i, b_j and b_k are conventional rather than restrictive, as the parameters a can have any sign.

The features and terminology of a common linear programming problem are introduced using the following example:

$$\text{Maximize } z = x_1 + x_2$$

$$\text{Subject to } x_1, x_2 \geq 0$$

$$\text{and} \begin{cases} 2x_1 - x_2 \leq 5 \ \ (m_1 = 1) \\ 3x_1 + 2x_2 \geq 2 \ \ (m_2 = 1) \\ x - 3y = -9 \ \ (m_3 = 1) \end{cases}$$

[5] For some reason, Linear Programming is typically presented using the maximum extremum, instead of the minimum extremum, as used for the unrestricted extremum-finding theory.

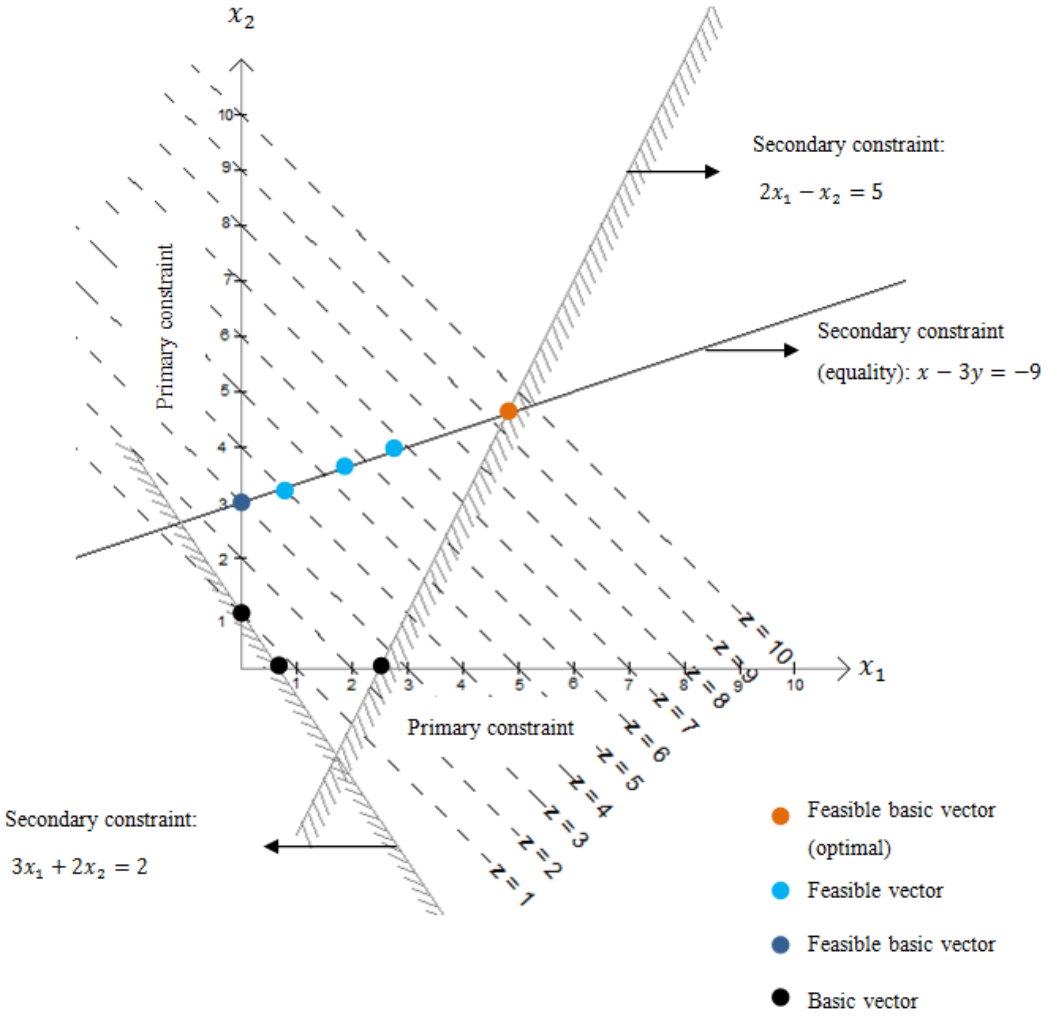

Figure 3-10 - General concepts of a linear programming problem

Figure 3-10 illustrates some basic concepts of the linear programming theory:

- Basic vector: a set $\boldsymbol{x}$ satisfying N (of the M) constraints as equalities;
- Feasible vector: a set $\boldsymbol{x}$ satisfying all existing constraints;
- Feasible basic vector: a set $\boldsymbol{x}$ satisfying all constraints, out of which N as equalities.

There are some important remarks regarding the linear programming problems. The most important is the fundamental theorem of linear optimization, which states that the optimal vector corresponds to a feasible basic vector (Press *et al.*, 1992). However, optimal feasible vectors may not exist when no feasible vectors exist or when feasible vectors exist, but the objective function is unbounded. It is sometimes possible that a linear programming problem is set up so it has no feasible solution, mainly because the problem is unsolvable or because of

errors in the problem set up. For instance, if the problem is over-constrained, it is possible that no solution exists that respects all the constraints. Another possible issue is that the objective function may be unbounded, which means that the problem is under-constrained and therefore ill-posed. Another important remark regards the relation between the type of constraints and the dimensionality of the problem. The inequality constraints limit the area of the (hyper)plane represented by the objective function where the feasible vectors are located. Conversely, equality constraints reduce the dimensionality of the problem by one. This is illustrated in Figure 3-10, where the equality constraint situate the feasible vectors on a line rather than committing them to a certain region of the plane, as inequality constraints do.

The importance of the fundamental theorem of linear optimization relies on the fact that it reduces the linear optimization problem to finding the best feasible basic vector. Thus, an immediate strategy is to start in a feasible point, proceed in the direction of the gradient until the limit of an inequality constraint is found, go along this constraint until another limit is encountered and continue the process until the optimal point is found. However, this procedure can be simplified by using a more efficient approach, the simplex method.

The simplex method is a way of organizing the strategy that came out of the fundamental theorem of linear optimization, such that the objective function increases at each step and the optimal feasible vector is reached after no more than N or M iterations, whichever is greater. A full description of the simplex method is, however, beyond the scope of this document.

3.5 Numerical application

In order to illustrate the application of the optimization theory introduced in this chapter, an example of structural optimization problem is presented next. The example is the well-known constant stress bar problem, where the exact (exponential) generatrix is approximated by a parabola. To illustrate the strategy adopted for obtaining the optimal surface, all calculations are given in full detail. It should be noted that an intuitive approach was preferred to other, more efficient solution strategies, to enhance the legibility of the text.

3.5.1. Size optimization of a cylindrical bar

The problem solved in this section is formulated as follows: given a bar of an initially cylindrical shape and length L, constructed of a material of specific weight γ and yield stress σ_c and subjected to its own weight and an acting force P uniformly distributed on its free cross section (Figure 3-11), find the optimal shape of the bar such as to minimize its mass (or volume) while not exceeding the yield stress in any cross section.

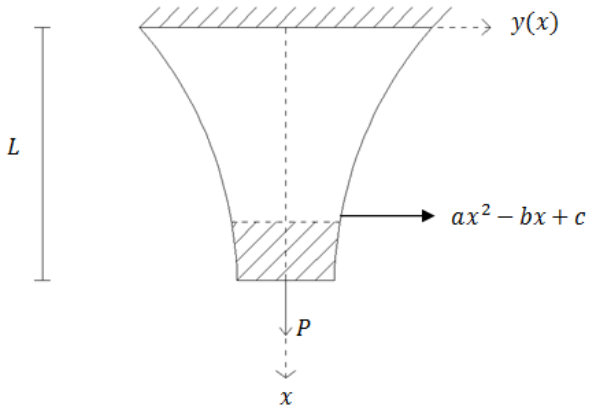

Figure 3-11 - Constant stress bar

The analytical solution of this problem is well-known. The optimal shape of the bar corresponds to a surface of revolution generated by an exponential curve, with a variation of the cross sectional area given by,

$$A(x) = \frac{P}{\sigma_c} e^{\frac{\gamma(L-x)}{\sigma_c}} \tag{3.32}$$

As typical of the size optimization problems, the expression of the generatrix is approximated using a polynomial, in this case, a parabola,

$$r_{approx}(x) = ax^2 - bx + c \tag{3.33}$$

where *a*, *b* and *c* are the optimization parameters to be determined.

Using this approximation, the volume of the body comprised between x and L is,

$$V = \int_x^L \pi(ax^2 - bx + c)^2 dx$$

$$V(x) = \frac{\pi a^2}{5}(L^5 - x^5) - \frac{\pi ab}{2}(L^4 - x^4) + \frac{\pi}{3}(b^2 + 2ac)(L^3 - x^3) - \pi bc(L^2 - x^2) + \\ + \pi c^2(L - x)$$

The objective function to minimize is therefore,

$$V_{tot} = V(0) = \frac{\pi a^2}{5} L^5 - \frac{\pi ab}{2} L^4 + \frac{\pi}{3}(b^2 + 2ac)L^3 - \pi bcL^2 + \pi c^2 L \qquad (3.34)$$

subjected to the bounds and restrictions given in Table 5:

Bounds	$x \geq 0$ $a, b, c \geq 0$
Restrictions	$ax^2 - bx + c \geq 0$ $\sigma(x) = \frac{P + \gamma V(x)}{A(x)} \leq \sigma_c$

Table 5 - Bounds and restrictions of the problem

The problem is solved using the following values for the size, material and loading parameters,

$$\begin{cases} P = 1\ kN \\ \sigma_c = 10\ kPa \\ \gamma = 1\ kN/m^3 \\ L = 1\ m \end{cases}$$

As the objective function and the restrictions are non-linear, the example presented here is more complex than a linear programming problem. Despite its greater complexity, however, the problem can be handled by combining minima-finding methods (applied to the searching domain, that is, the locus of the feasible vectors) and the linear programming method, which is used to explore the borders of the domain by "walking" along the inequality constraints until the optimal point is found.

a) Search for a feasible basic vector: find *a*, *b* and *c* such that all restrictions are satisfied, three of which in equality form.

Option 1: keep $b = c = 0$ and vary a,

$$\frac{P + \gamma V(x)}{A(x)} \leq \sigma_c \Leftrightarrow \frac{1 + \frac{\pi a^2}{5}(1^5 - x^5)}{\pi(ax^2)^2} \leq 10 \Leftrightarrow \frac{1}{\pi} + \frac{a^2(1 - x^5)}{5} \leq 10a^2x^4$$

For $x = 0$, it results $\frac{1}{\pi} + \frac{a^2}{5} \leq 0$ which is impossible.

Option 2: keep $a = c = 0$ and vary b,

$$\frac{P+\gamma V(x)}{A(x)} \le \sigma_c \Leftrightarrow \frac{1+\frac{\pi b^2}{3}(1^3-x^3)}{\pi(-bx)^2} \le 10 \Leftrightarrow 1+b^2\frac{\pi}{3}(1-x^3) \le 10x^2b^2$$

For $x=0$, it results $1+b^2\frac{\pi}{3} \le 0$ which is impossible as well.

Option 3: keep $a=b=0$ and vary c,

$$\frac{P+\gamma V(x)}{A(x)} \le \sigma_c \Leftrightarrow \frac{1+\pi c^2(1-x)}{\pi c^2} \le 10$$

For $x=0$,

$$1+\pi c^2 \le 10\pi c^2 \Leftrightarrow 9\pi c^2 \ge 1 \Leftrightarrow c \ge 0.188$$

For $x=L=1$, it results $1 \le 10\pi c^2$ which is true. Thus, a feasible basic vector is $\begin{cases} a=0 \\ b=0 \\ c=0.188 \end{cases}$

b) Obtain the optimal value of parameter b by "walking" through the domain along the direction given by $(a,c)=(0,0.188)$ in order to minimize V_{tot}.

Before performing the minimization, the bounds of b must be identified, such as to satisfy all the inequality restrictions,

$$\frac{P+\gamma V(x)}{A(x)} \le \sigma_c \Leftrightarrow \frac{1+\frac{\pi b^2}{3}(1^3-x^3)-\pi 0.188b(1^2-x^2)+\pi 0.188^2(1-x)}{\pi(-bx+0.188)^2} \le 10$$

For $x=0$,

$$\frac{1+\frac{\pi b^2}{3}-\pi 0.188b+\pi 0.188^2}{\pi 0.188^2} \le 10 \Leftrightarrow 0 \le b \le 0.56286$$

For $x=L=1$,

$$\frac{1}{\pi(-bx+0.188)^2} \le 10 \Rightarrow \begin{cases} b \le 0.0096 \\ b \ge 0.366 \end{cases}$$

The result $b \ge 0.366$ is rejected as it turns the expression ax^2-bx+c negative. Thus, the feasible values for b range between 0 and 0.0096.

The variation of $V_{tot}=\frac{\pi b^2}{3}-\pi 0.188b+\pi 0.188^2$ with the parameter b is plotted in Figure 3-12. As b can only take values between 0 and 0.0096, the point that minimizes the total volume is $b=0.0096$.

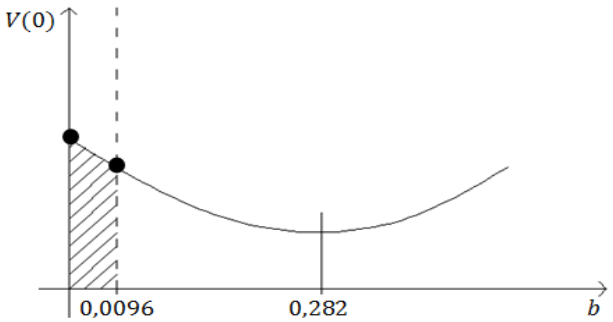

Figure 3-12 - Function V_{tot} for a = 0 and c = 0.188

c) Obtain the optimal value of parameter a by "walking" through the domain along the direction given by $(b, c) = (0.0096, 0.188)$ in order to minimize V_{tot}.

Before performing the minimization, the bounds of a must be identified, such as to satisfy all the inequality restrictions,

$$\frac{P + \gamma V(x)}{A(x)} \leq \sigma_c \Leftrightarrow 1 + \frac{\pi a^2}{5}(1 - x^5) - \frac{\pi\, 0.0096\, a}{2}(1 - x^4) +$$

$$+ \frac{\pi}{3}(0.0096^2 + 2a\, 0.188)(1 - x^3) - 0.0096\, \pi\, 0.188(1 - x^2) +$$

$$+ \pi 0.188^2(1 - x) \leq 10(ax^2 - 0.0096x + 0.188)^2$$

For $x = 0$,

$$1 + \frac{\pi}{5}a^2 - 0.0151a + 0.9651 \times 10^{-4} + 0.3937a - 0.00567 + 0.111 \leq 1.11036 \Leftrightarrow$$

$$\Leftrightarrow \frac{\pi}{5}a^2 + 1.1054265 + 0.3786a \leq 1.11036 \Leftrightarrow$$

$$\Leftrightarrow \frac{\pi}{5}a^2 + 0.3786a - 0.004938 \leq 0 \Leftrightarrow \begin{cases} -0.615333 \leq a \leq 0.0127721 \\ a \geq 0 \end{cases}$$

For $x = L = 1$,

$$1 \leq 10\pi(a - 0.0096 + 0.188^2)^2 \Leftrightarrow 1 \leq 10\pi(a + 0.1784)^2 \Leftrightarrow \begin{cases} a \geq 0 \\ a \leq -0.356812 \end{cases}$$

Thus, the feasible values for a are between 0 and 0.0127721.

The variation of the total volume as a function of the parameter a is presented in Figure 3-13. While the global minimum of the function is found at $a = -0.301$, this point does not correspond to the feasible interval. Therefore, the optimal point is found on the limit of the feasible interval, at $a = 0.000$.

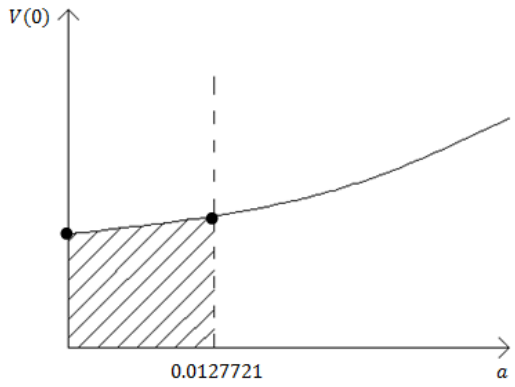

Figure 3-13 - Function V_{tot} for b=0.0096 and c=0.188

The first optimization iteration is now completed. It started from the initial point $(a, b, c) = (0,0,0)$ and successively minimized the objective function in c, b and a directions. The new "optimal" point after the first iteration is $(a, b, c) = (0.000,0.0096,0.188)$. Further improvements may be achieved by repeating the procedure described above, starting now in the "optimal" point that resulted after the first iteration. The process, however, is repetitive and is not included in this document.

It is now possible to compare the values of the cross sectional areas of the bar corresponding to the "optimal" values of the parameters a, b and c with their analytical counterparts obtained using expression (3.32). These values are presented in Table 6 and the variation of the corresponding radii illustrated in Figure 3-14.

The assessment of the two curves in Figure 3-14 shows that the "optimal" vector found yields a good approximation of the exact area values for the considered problem. It should also be noted that the approximation produces larger area values than the exact solution, meaning that it produces structurally safe results.

Area values		
x	**Theoretical** $A(x) = \frac{P}{\sigma_c} e^{\frac{\gamma(L-x)}{\sigma_c}}$	**Approximated** $A(x) = \pi(0.188 - 0.0096x)^2$
0	0.110517	0.111036451
0.1	0.109417	0.109905357
0.2	0.108329	0.108780053
0.3	0.107251	0.107660541
0.4	0.106184	0.106546818
0.5	0.105127	0.105438887
0.6	0.104081	0.104336746
0.7	0.103045	0.103240395
0.8	0.10202	0.102149835
0.9	0.101005	0.101065066
1	0.1	0.099986087

Table 6 - Cross sectional area of the bar – approximated and exact values

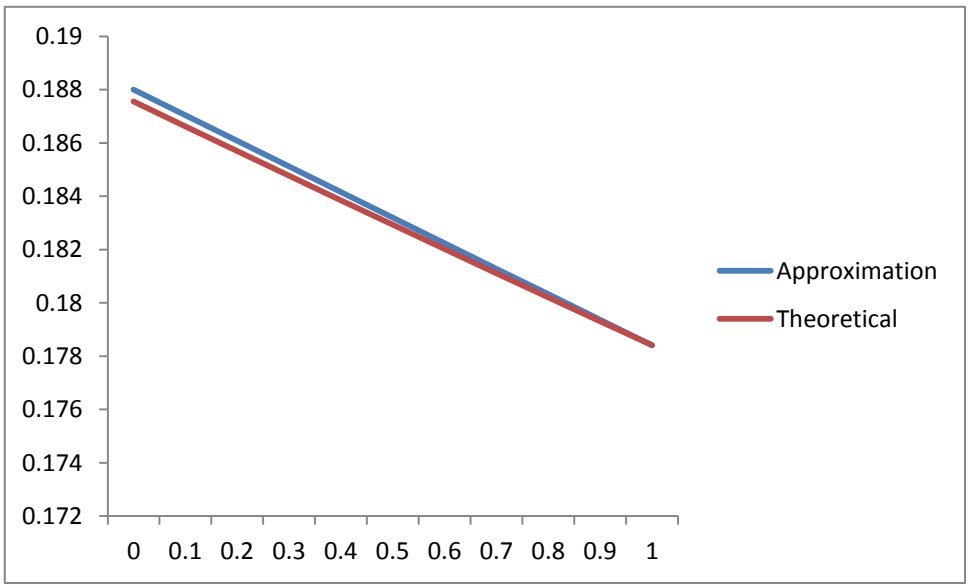

Figure 3-14 - Variation of the cross sectional radius – approximated and exact values

3.6 Function minimization methods in MSC.-NASTRAN

The structural optimization application reported in the next chapter uses the finite element package MSC.-NASTRAN. It is therefore relevant to briefly describe the function minimization methods that are used to perform the structural optimization in this software.

From the minimization methods described in this work, the methods used by MSC.-NASTRAN involve the computation of the gradient. Therefore, from the unconstrained minimization methods, MSC.-NASTRAN uses the steepest descent method, which is based on the determination of the local downhill gradient of an initial arbitrary point to obtain the following iteration point, and the conjugate gradient method, which is based on the minimization along the conjugate directions. However, as many optimization problems are restricted problems, the optimizer uses restricted optimization methods as well, such as linear programming, used when both objective function and constraints are linear.

To introduce the main concepts and procedures used by MSC.-NASTRAN for structural optimization, the topological optimization of a simple cantilever plate is presented next. This example shows the basic steps of a topological optimization, from the creation of the finite element mesh and definition of loads and boundary conditions to the determination of basic topology result and the analysis of the optimized structure.

3.6.1 Topological optimization of a cantilever plate

The optimization theory is applied next to the topology optimization of a cantilever plate. The topology optimization aims to determine the final layout of a structure by achieving an optimal distribution of material, given the design space, boundary conditions, loads applied and required design performance.

The framework of the topology optimization in MSC.-NASTRAN is the Density (or the Artificial Material) Method. In this approach, an artificial homogeneous material is used and each element of the model is given an additional property of relative density, which is used to control the stiffness properties of the elements. The relation between the effective material stiffness and the relative density is given by equation,

$$E_e = E_0 \xi_e{}^p \qquad (3.35)$$

where,

$$\xi_e = \frac{\rho_e}{\rho_0} \qquad (3.36)$$

In equation (3.35), E_0 is the Young's modulus of the real material, E_e is the Young's modulus of the fictitious material assigned to the elements, ξ_e stands for the relative density, defined as

the quotient between the densities of the fictitious and the real materials. The relative density takes values between 0 and 1, and p is a penalty factor introduced to enhance the control on the design variables. (Kim *et al*., 2011)

The topology optimization process starts with the definition of the design space, that is, the initial approximation of the topology of the structure, followed by the creation of the finite element model and the respective analysis. It is within the next step (the achievement of the basic topology result) that the relative density gains purpose. An initial finite element analysis is performed on the non-optimized structure, and a relative density value is attributed to each finite element, according to the predicted intensity of the stress field and the percentage of material to save. This value is compared with a threshold value previously defined by the analyst and the elements with lower relative densities are eliminated.

It should be noted that the threshold value and the material reduction to be accomplished are independent parameters of the optimization. The percentage of material reduction is defined as a mass target constraint in the process and has influence on the attribution of relative densities to the elements, while the threshold value of the relative density is a parameter that enables the elimination of elements with densities inferior to it, which can lead to a coarse optimized structure or, more often, to information about the final shape to the design team. For instance, by setting the threshold value to 0.0, no elements are eliminated. Nevertheless, the values of the relative densities of the elements still give important information about which elements could be eliminated to reach the defined mass reduction. Visually, this information is given through different colored elements: the white elements represent the elements with the lower density and the red elements are elements with higher density. This enables the analyst to verify the distribution of the lowest density elements along the structure, without actually eliminating any parts of it. On the other hand, when the threshold value is different from 0.0, it is possible to promptly obtain an optimized structure by eliminating the elements whose relative densities are lower than the threshold value in order to reach the defined mass reduction percentage. This generates a basic topology result that, although a coarse approximation, is closer to a feasible final design. After obtaining the basic topology result, the following step consists of the smoothing of the edges of the resulting structure, and the final design of the part is complete. It should be noted that this last step, consisting on the creation of the final optimized design, although possible to accomplish directly through the pre/post-processor PATRAN, as performed for the following example, is generally obtained by a careful evaluation of the topological optimization result by the design team so that the final design is practically feasible.

To illustrate this procedure, consider the problem of the cantilever plate represented in Figure 3-15, subjected to a concentrated force *Q* acting on its free surface. The goal of the analysis is to perform a topology optimization task such that 50% of the mass is removed. The plate is constructed of aluminum and has the geometric and material characteristics presented in Table 7.

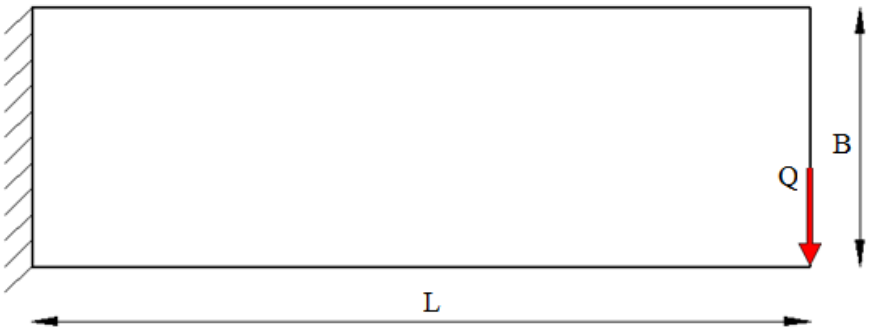

Figure 3-15 - Cantilever plate

Dimensions and Properties	
L	30 mm
B	10 mm
t	1 mm
E	68.9 GPa
ν	0.33
Q	30 N

Table 7 - Dimensions and properties of the cantilever plate

Previous to the optimization procedure, a linear static analysis is performed on the initial structure in order to verify the stress and displacement fields occurring in the non-optimized structure and compare with the correspondent stress and displacement fields of the optimized structure. The finite element mesh used on the initial structure is constructed using 1200 quadratic shell elements with the edge length of 0.5 mm. The stresses and the deformed shape of the initial structure are presented in Figures 3-16 and 3-17, respectively.

The stress plot of the initial structure shows that the larger stresses occur in the areas where the cantilever plate is constrained and near the load application, generating smaller stresses in the center and upper right sections of the structure, where no loads or constraints are

applied. The larger displacements verified in the structure occur at the right section, where no constraints are applied, with the largest displacement value occurring at the load application area.

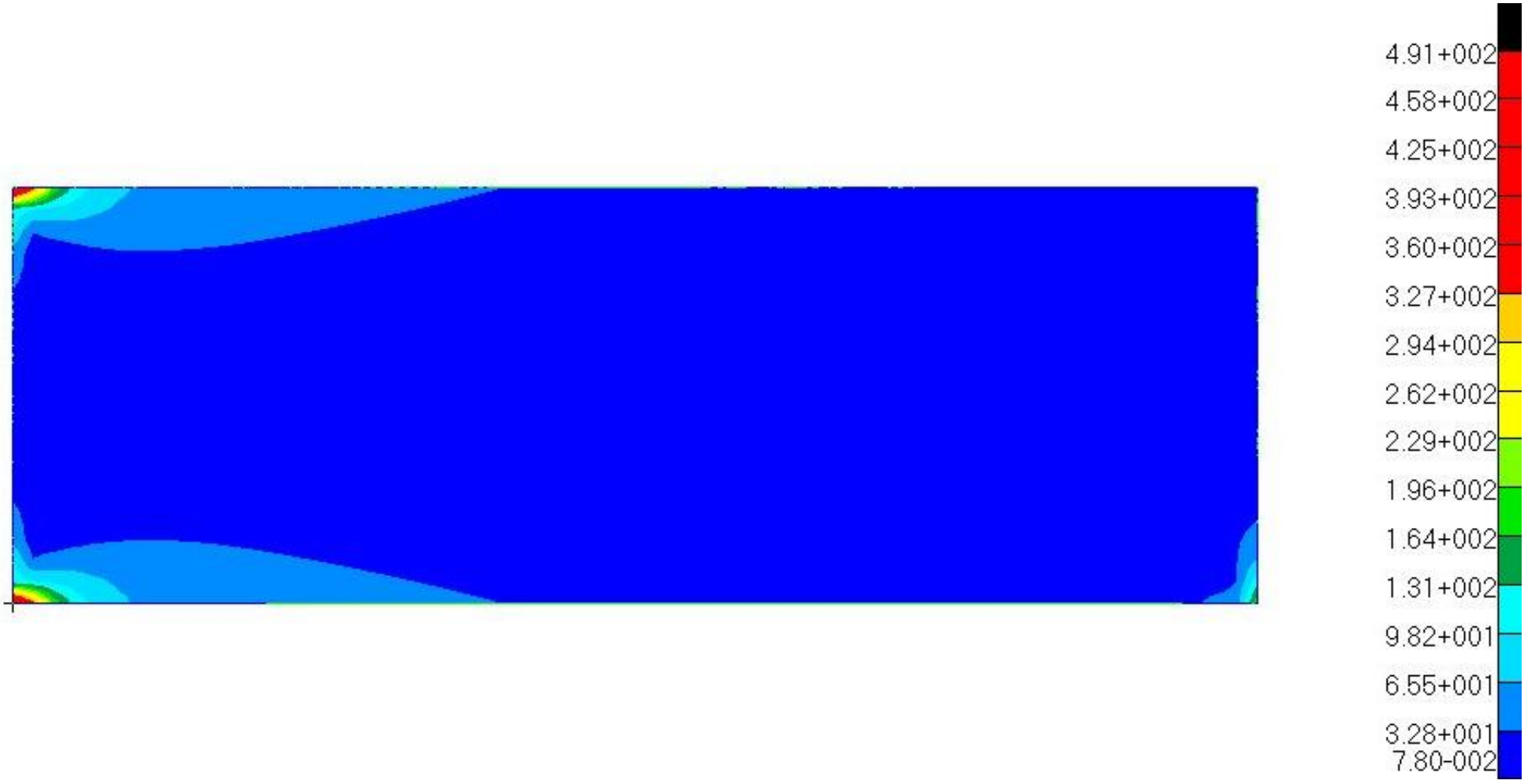

Figure 3-16 – von Mises stress output of the non-optimized cantilever plate

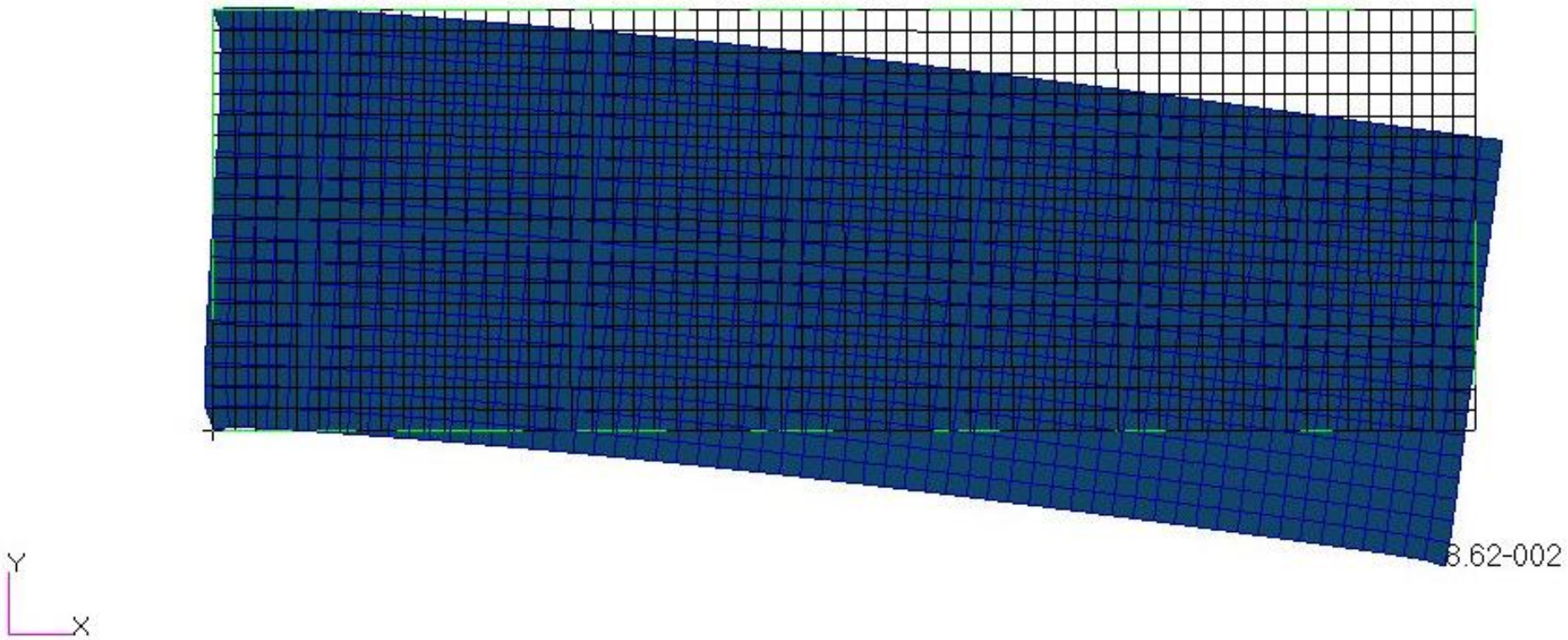

Figure 3-17 – Deformed shape of the cantilever plate

In order to set up the optimization job, several optimization parameters are defined. The value of the desired remaining mass after optimization is set by defining a mass factor of 0.5 for the mass target constraint. This constraint should enable the reduction of the total material mass in 50%. The design variable is the normalized material density of each element and its initial value is taken 0.5 in order to match the mass target constraint and to assure that the initial design is feasible. The penalty factor[6] was assigned a value of 3.

After performing the analysis, MSC.-NASTRAN displays the density distribution of the optimized structure, as illustrated in Figure 3-18. All elements are included in the density distribution plot, as the threshold parameter is set to 0 (no elements are eliminated). The dark colored elements have higher relative densities, marking the regions of the structure with the highest stress intensity.

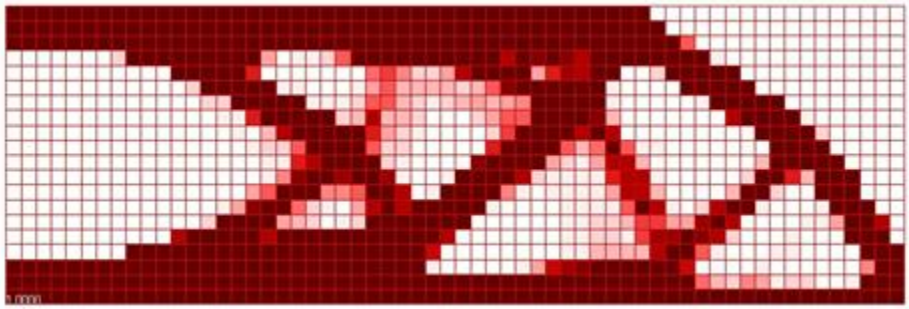

Figure 3-18 - Different density elements in the model

To obtain the basic topology result, the density threshold parameter is set to 0.4 and the finite elements with relative densities lower than this value are now removed. Figure 3-19 presents the basic topology design obtained using this setting.

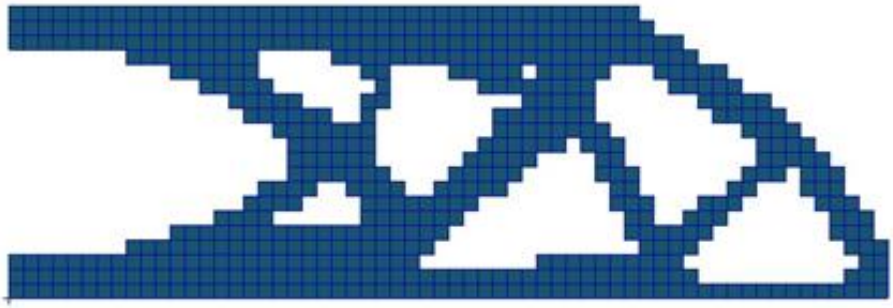

Figure 3-19 - Element density distribution for a density threshold of 0.4

[6] Commonly, in topology optimization the penalty factor is between 2 and 4.

The next step towards the final design is the smoothing of the resulting optimized shape, for easier manufacturing. The final design should include the structural members which proved to be essential for the transmission of the load. For the study case presented here, the resulting optimized structure is presented in Figure 3-20. This is the final topology design of the cantilever plate.

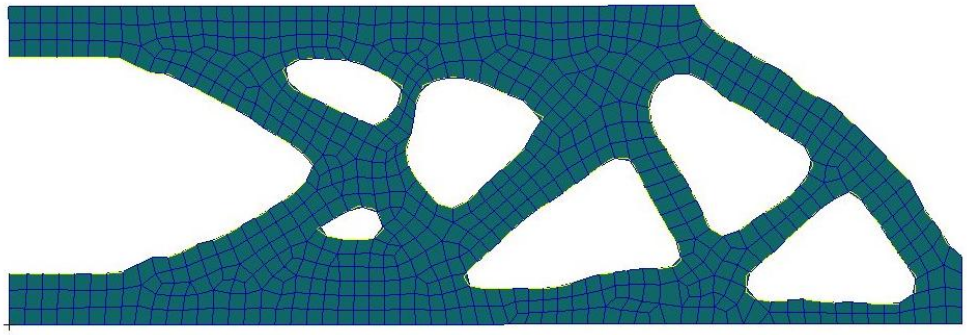

Figure 3-20 - Smoothed structure topology design

The solution obtained for this problem involves material savings of roughly 50%, which was the value defined as the mass constraint target. As shown in Figure 3-20, the material distribution corresponds to the expected principal stress directions associated to the application of the concentrated load at the tip of the cantilever. Conversely, the removed material corresponds mainly to the central area, where the stresses are relatively low in a bending-dominated problem and to the upper-right area which is not affected by the applied load.

It should be noted that performing an optimization job using MSC NASTRAN requires detailed knowledge on the method used by this software to accomplish the job. A good understanding of the methodology endorses the optimal definition of the design parameters required for the optimization setup, such as the penalty factor or the initial design value.

Once obtained the smoothed topology result, it is possible to perform a linear static analysis on the optimized structure. The stress output of the optimized cantilever plate, presented in Figure 3-21, shows that the larger stresses remain on the areas of load and constraints application and are slightly lower than the maximum stress obtained in the non-optimized structure, as in the latter a maximum stress of 491 MPa was obtained, opposed to 461 MPa obtained in the optimized structure, corresponding to a stress decrease around 6%. The deformed shape of the optimized structure is presented in Figure 3-22, where is possible to verify that the area where the largest value of displacement occurs remains the area of load

application and the displacements obtained for the optimized structure are only slightly larger than the displacements obtained for the non-optimized cantilever plate.

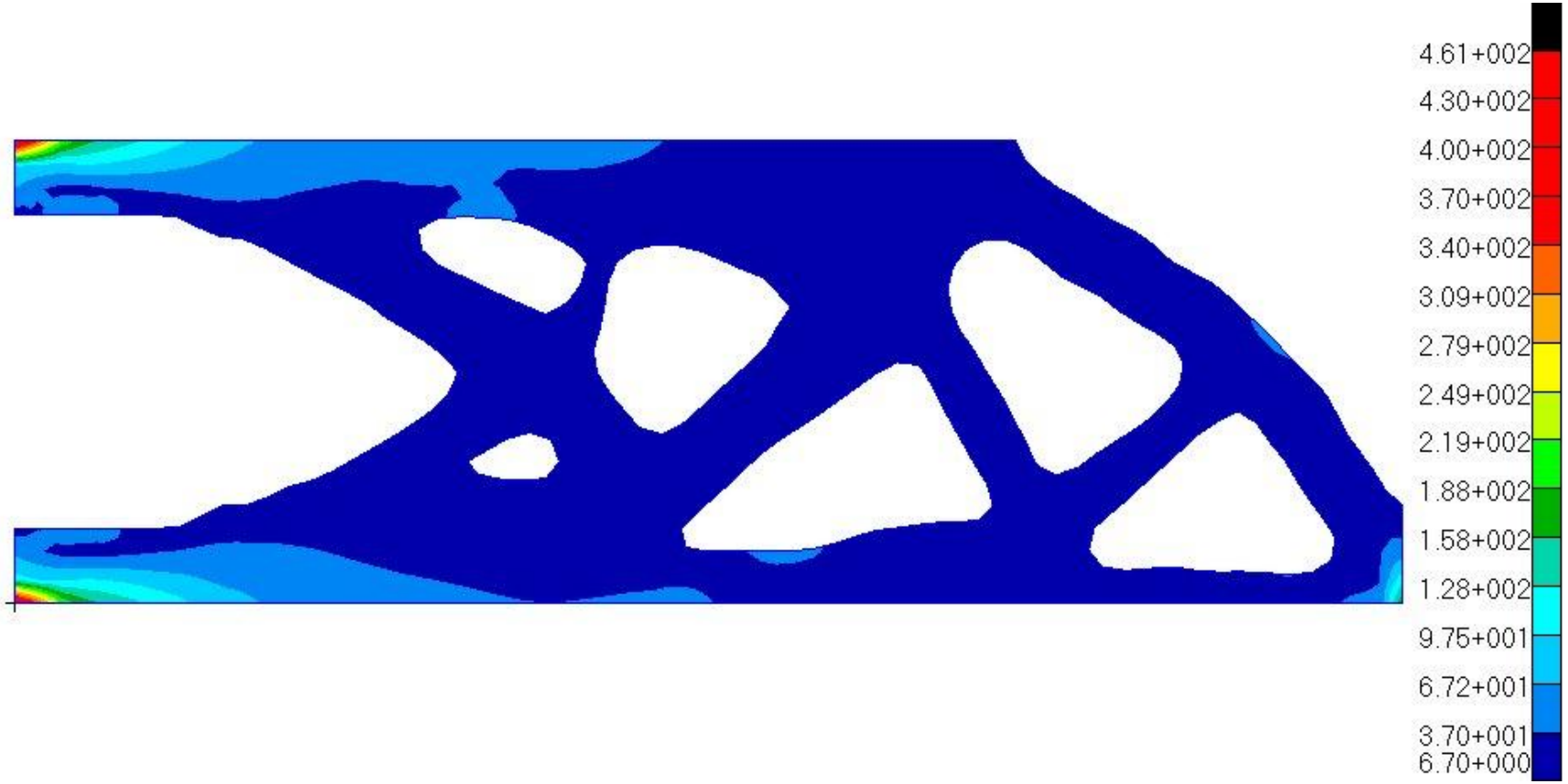

Figure 3-21 – von Mises stress output of the optimized cantilever plate

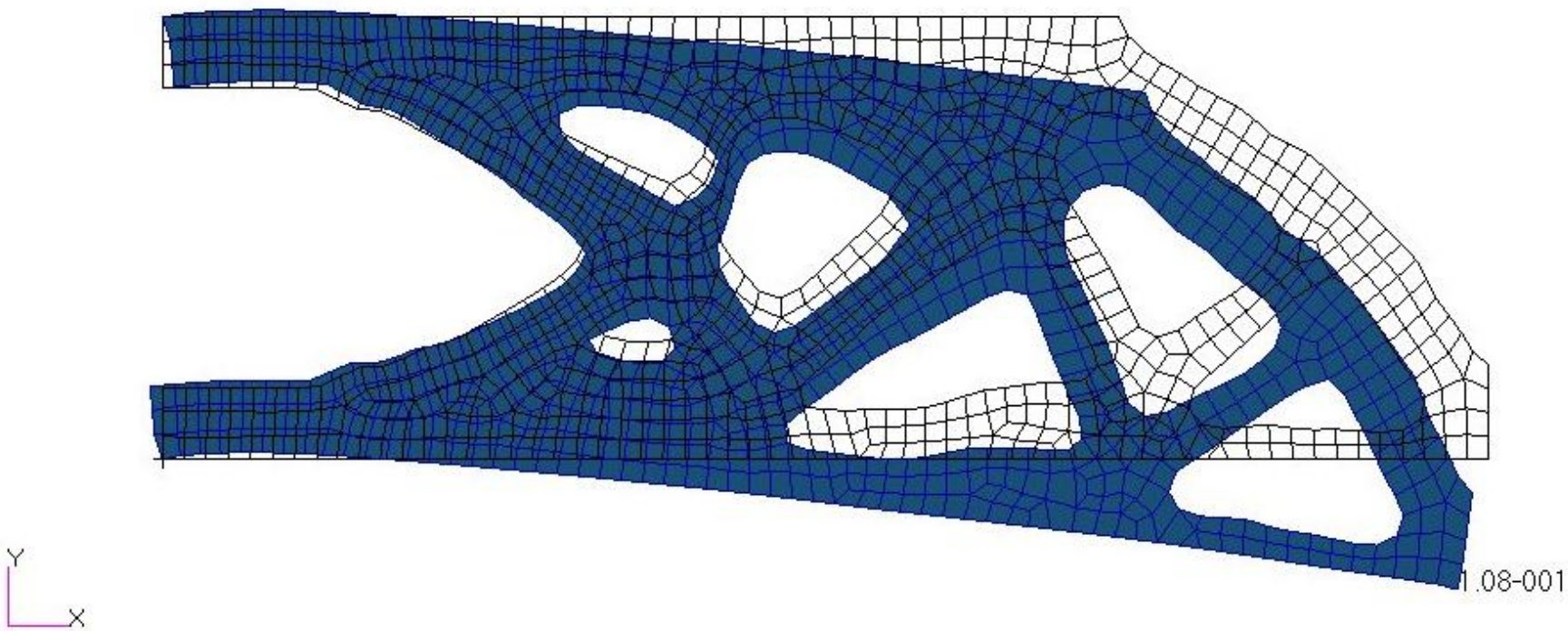

Figure 3-22 - Deformation of the optimized cantilever plate

4 STRUCTURAL OPTIMIZATION OF A WHEEL CARRIER

4.1 Introduction

Since early ages, humans were confronted with the necessity of moving from one location to another and the means used to cover those distances are an interesting study subject on itself. Initially, humans moved from one point to another simply by walking, but the necessity of covering longer distances and exploring new territories led to the use of animals for transportation. A significant improvement on this matter came along with the invention of the wheel, which enabled the creation of animal-powered vehicles. The first wheels, discovered in Mesopotamia, date back to around 3500 B.C. and consisted simply of planks of wood joined together. The technique was later improved by the Egyptians, who made wheels with spokes, and by the Romans, who created a large variety of wheeled vehicles. The invention of the automobile as we know today only took its first steps in 1769 when Nicolas-Joseph Cugnot[7] constructed a steam powered vehicle. However, it was only in 1885 that Karl Benz created the first vehicle powered by an internal combustion engine. Later, in 1913, Henry Ford started producing Ford model T at a large scale through a new and revolutionary assembly line, creating the basis for the current large scale vehicle production.

It is based on this large scale production reality that the structural optimization and, more specifically, the material consumption optimization, are very important. There are multiple reasons for this: on the one hand, as vehicles are typically produced in large series, seemingly minimal savings in materials for one vehicle may mean vast savings for the total production of that model series. On the other hand, as the dead weight is a significant part of the total load a vehicle must support (typically much more than 50%), its minimization may lead to a significant increase in the overall performance of the vehicle.

The daily-growing quality provided by the vehicle producers requires as well daily-growing improvements of the design of the structural components. The improvements of the structural components of the vehicle, such as the weight reduction, enhance the vehicle's performance and reduce the production costs.

The advances accomplished by the structural optimization and structural analysis tools opened the possibility of optimizing complex components that would have been impossible just

[7] Although the creation of the first automobile vehicle is attributed to Nicolas-Joseph Cugnot, some sources claim that the Belgian missionary Ferdinand Verbiest created a steam-powered vehicle in 1672 for the Chinese emperor Chien Lung.

a decade ago. To fully illustrate and understand such complex processes, a topology optimization performed on an automobile wheel carrier is reported in this work.

4.2 Problem description

The wheel carrier is the structure that ensures the connection between the wheel and the main vehicle structure. It is responsible for the transmission of loads that arise from the driving conditions and for supporting the wheel itself. Figures 4-1 to 4-4 present different views of the wheel carrier structure.

The structural optimization reported in this work is performed on a wheel carrier of a motorsports car. In the motorsports domain, the structural weight is one of the most relevant topics to deal with, becoming the focus of several optimization works, such as the one reported in this dissertation.

To perform the optimization, the first step involves the definition of idealized loads and boundary conditions that assure a reliable representation of the real boundary conditions that arise from the connection of the carrier with the main structure of the vehicle and of the loads applied during real driving conditions. It should be noted that the load cases created are static equivalent loads and thus cannot replace a detailed fatigue analysis. For the optimization procedure, and given the structural model of the wheel carrier, several finite element meshes are studied in order to verify which one is best for performing the pre-optimization analysis. Once the finite element mesh is chosen, the static analysis is performed and the stresses and displacements occurring on the non-optimized wheel carrier are obtained. The next step consists of the topology optimization in order to obtain a new optimized structure, on which several evaluations are performed to compare the stress and displacement values in the optimized and non-optimized structures.

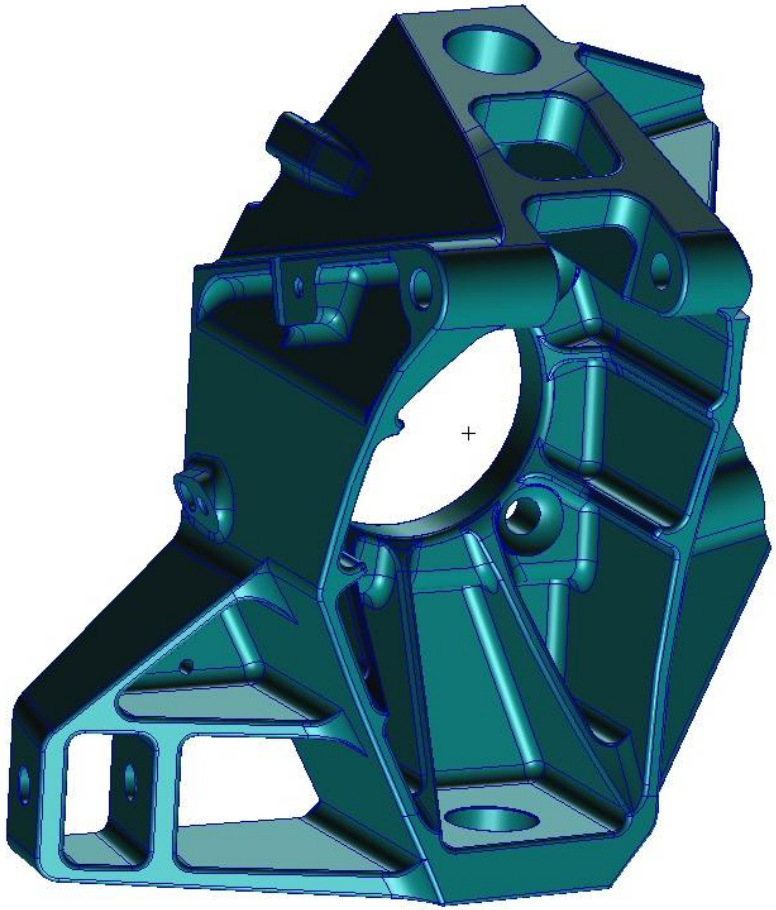

Figure 4-1 - Front left view of the wheel carrier

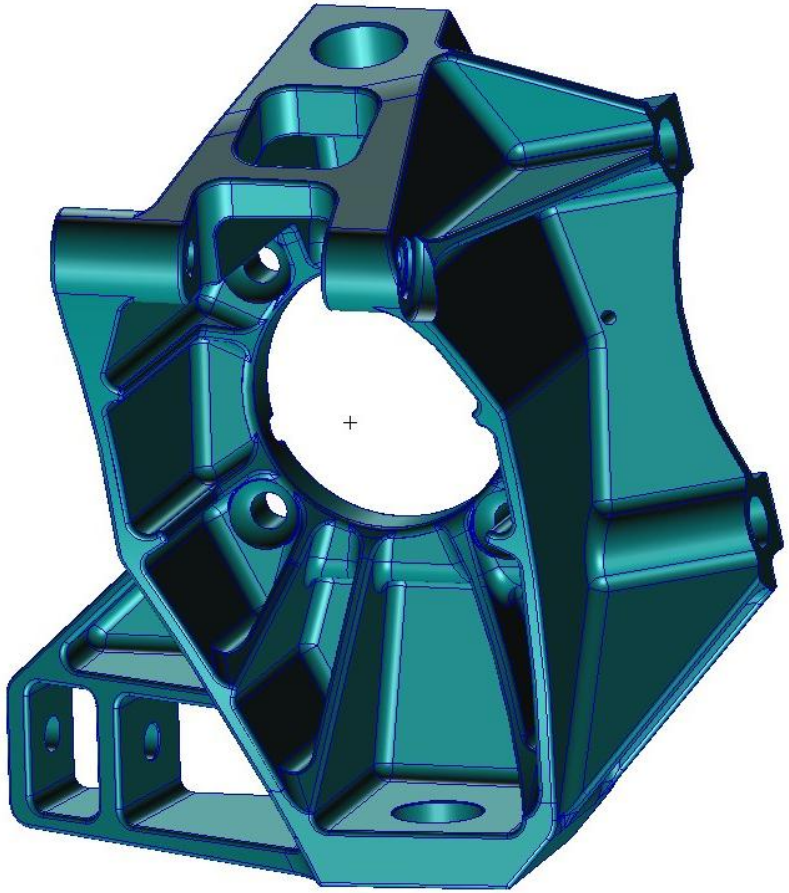

Figure 4-2 - Front right view of the wheel carrier

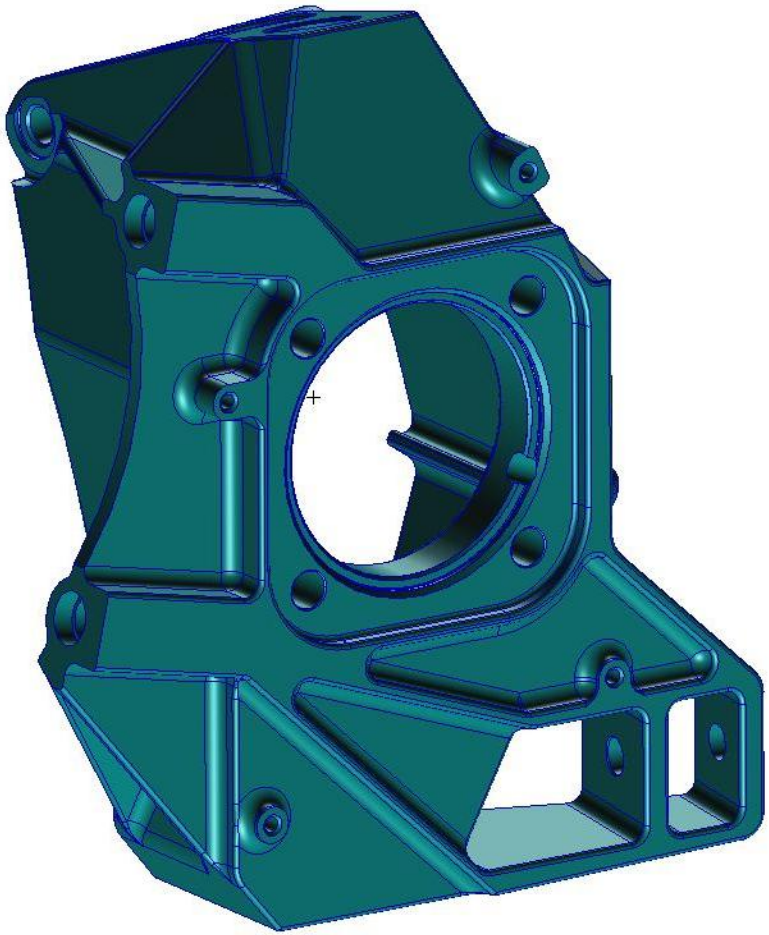

Figure 4-3 - Back left view of the wheel carrier

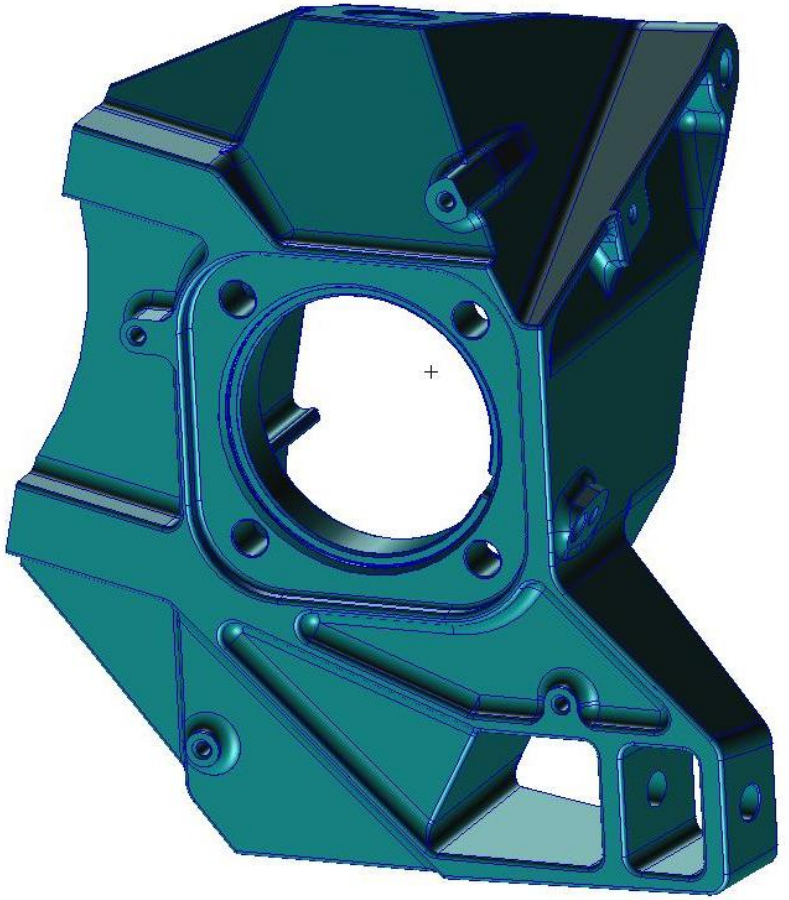

Figure 4-4 - Back right view of the wheel carrier

The wheel carrier is made of aluminum Al7075 (3.4365, AlZnMgCu1,5), as a milled part, whose properties are presented in Table 8. In this table, the *Rp0,2* indicates the conventional yielding stress, that is, the stress at which the material experiences a plastic strain of 0.2% The total mass of the non-optimized wheel carrier structure is 3.589 kg.

Properties	
E	71 GPa
ν	0.33
Rp0,2	440 MPa

Table 8 - Aluminum Al7075 properties

The software used to perform the wheel carrier analysis and optimization is composed of the solver MSC.-NASTRAN and the pre/post-processor PATRAN. The latter is a pre- and post-processor software through which is possible to create or import the model geometry, define the finite element mesh, apply the loads and boundary conditions, create material and element properties, submit the model to the solver and create the deformation and stress fringe plots. The solver, MSC.-NASTRAN, is a finite element analysis program extensively used by aerospace, automotive and civil engineering industries, capable of solving a large variety of engineering problems, such as linear static analyses, composite material analyses, acoustic analyses and design sensitivity and optimization. Figure 4-5 schematizes the software used and presents the main capabilities of the pre/post-processor and the solver.

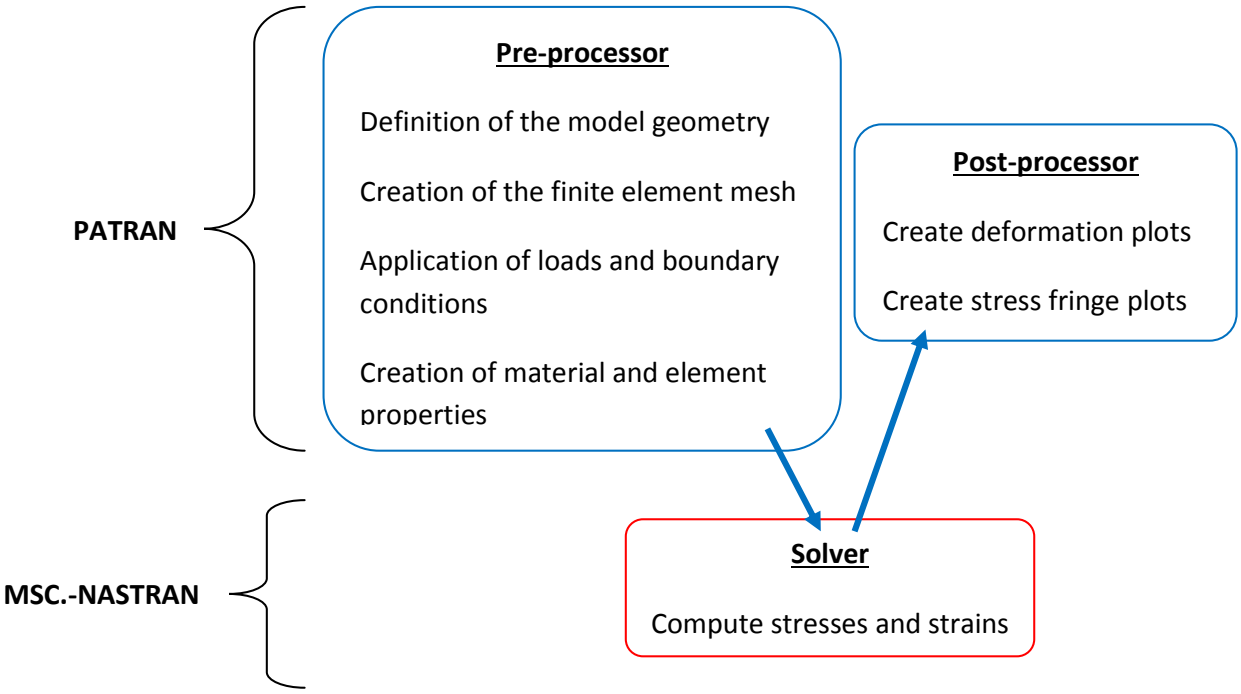

Figure 4-5 - Pre/post-processor and solver used and respective main capabilities

4.3 Loads and boundary conditions

The values of the loads applied to the structure are obtained through a multi-body dynamic analysis performed on the chassis structure that is replaced by static forces, each simulating an extreme racing condition. For the wheel carrier, this procedure yields three load cases, identified in Figure 4-6, where A, B, C, D and E are the points where the load is applied. The constraints of this structure are applied in the screw centers, identified in Figure 4-7, where the translational and rotational displacements are fixed.

The applied loads and boundary conditions are meant to simulate several different driving conditions and arise from the connection between the wheel carrier structure and the remaining automobile structure. The Ratterkerb3 load case represents the rotational vibration that arises at the wheel axle once the vehicle drives over the kerbs at the edge of a race track, the Ludwigskerb load case simulates the lateral accelerations the vehicle experiences when driving over the kerbs and the Bremsen load case represents a general braking action. The values of the forces for the load cases were obtained through a statistical load spectrum, from which the maximum was filtered for each load case.

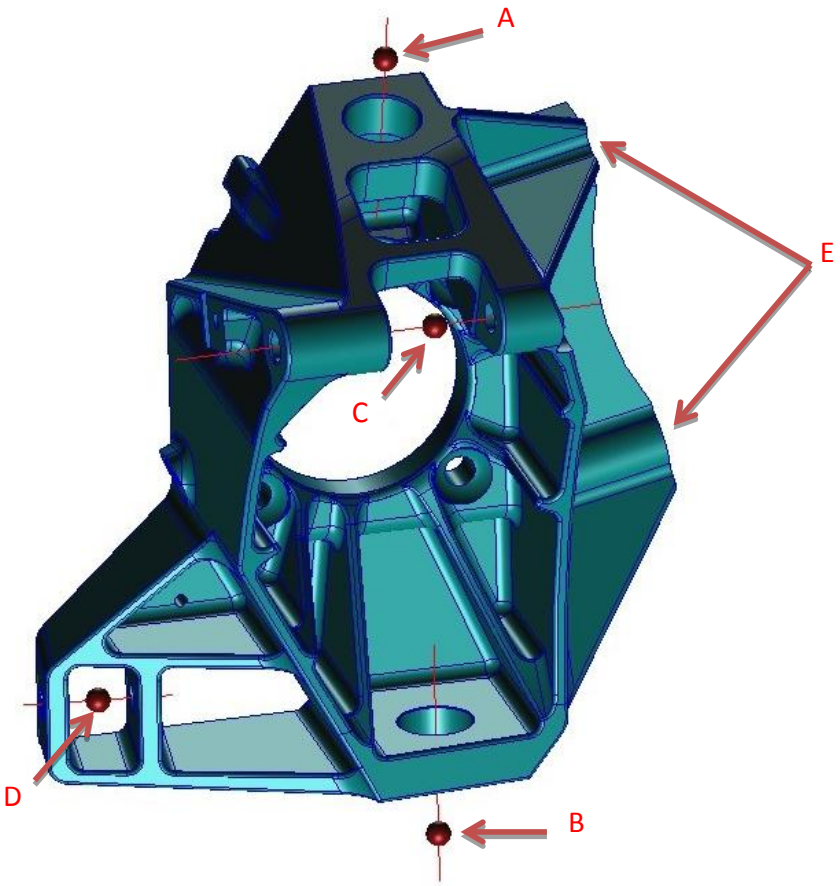

Figure 4-6 - Load application points

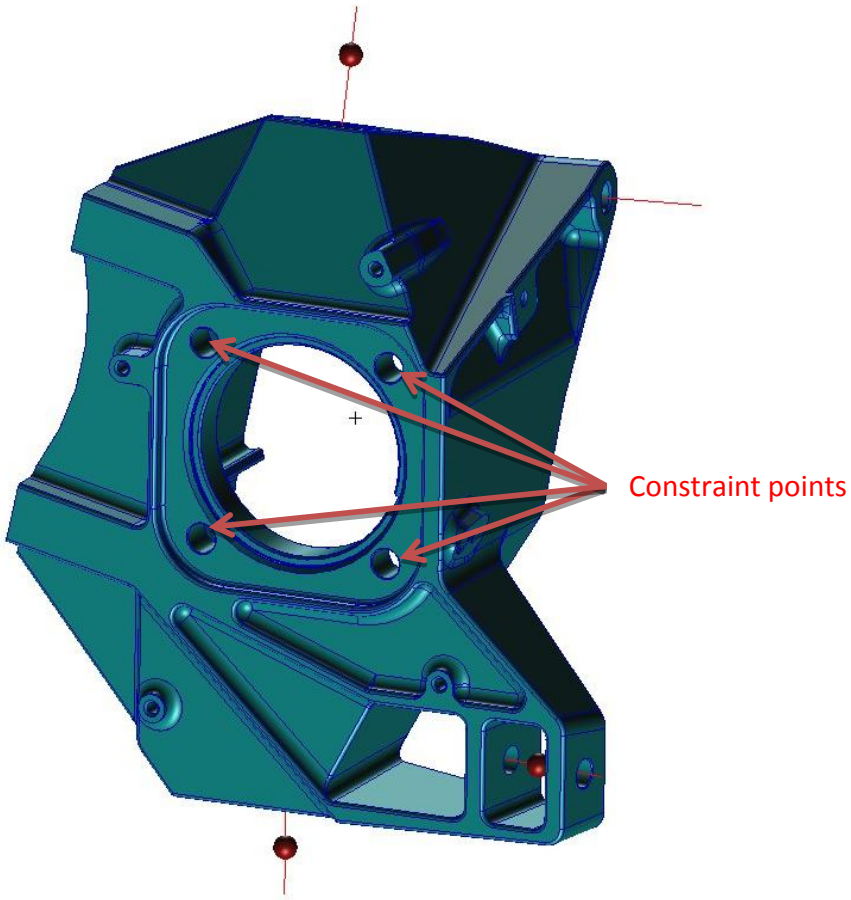

Figure 4-7 - Constraint application points

The forces and moments applied on points A, B, C, D and E for each load case are presented in Tables 9 to 11. It should be noted that point E is used only for the Bremsen load case, consisting of a braking moment.

Force/Moment	Load Case: Ratterkerb3				
	A	**B**	**C**	**D**	**E**
Fx [N]	228,2	759,6	-1828,2	290,7	0
Fy [N]	4673,8	7164,1	39,5	-1248,5	0
Fz [N]	-979,7	-3757	818	-6780,8	0
Mx [Nmm]	0	100	2800	0	0
My [Nmm]	100	-100	-100	0	0
Mz [Nmm]	500	0	5800	0	0

Table 9 - Applied loads for the Ratterkerb3 load case

Force/Moment	Load Case: Ludwigskerb				
	A	**B**	**C**	**D**	**E**
Fx [N]	2178,9	2,4	-10763,8	-298,3	0
Fy [N]	98,4	120,1	-142,4	-1233,3	0
Fz [N]	7851,4	-12365,1	4662,7	-6284,9	0
Mx [Nmm]	100	0	3500	0	0
My [Nmm]	-1400	400	-1000	0	0
Mz [Nmm]	0	0	4700	0	0

Table 10 - Applied loads for the Ludwigskerb load case

Force/Moment	Load Case: Bremsen				
	A	**B**	**C**	**D**	**E**
Fx [N]	-62,4	491,7	-2702,3	13,4	0
Fy [N]	-21817,7	6683,7	-146,5	-91,1	0
Fz [N]	970,6	-212,4	1213,3	-492,5	0
Mx [Nmm]	0	100	-17800	0	0
My [Nmm]	100	-100	-1200	0	0
Mz [Nmm]	100	-100	-40600	0	4000000

Table 11 - Applied loads for the Bremsen load case

The application of the loads and constraints is accomplished through the use of PATRAN objects MPC (Multiple Point Constraints), which are special element types capable of establishing a behavior rule between several specified nodes. The MPC's used in this structure are the types RBE2 and RBE3. The RBE2 elements define a rigid body zone behavior. A number of independent DOF, specified on an independent (master) node, control an arbitrary number of dependent DOF on some slave nodes. Thus, the RBE2 element simulates a rigid link between the dependent and the independent nodes, preventing any relative motion between them. Conversely, the RBE3 element is a link between one dependent and several independent nodes. This is an interpolation element used to distribute loads and mass over the respective nodes and to constrain the motion of the slave node to a weighted average of the motions of the master nodes. As opposed to the RBE2 elements, the RBE3 elements do not result in additional stiffness added to the structure, and therefore are more convenient to distributing the applied loads.

4.4 Finite element mesh

The choice of the type of finite elements and mesh size are of the utmost importance as it impacts directly the quality of the finite element solution and the computational time required to achieve it. For this application, three-dimensional elements were chosen. These elements (labeled as Tet10 in MSC.-NASTRAN) are tetrahedral in shape and have ten nodes, at the vortices and the middle of each side. They approximate the displacement field using quadratic functions. Consequently, the predicted stress field is linear within the element. It is relevant to refer that additional surface elements were applied over the three-dimensional elements as a

skin layer in order to compare the stresses occurring in the surface elements with the extrapolated stresses of the three-dimensional elements. The next step consists of creating the mesh of tetrahedral finite elements. The main challenge when creating the mesh is to strike the right balance between the need of accurate solutions, requiring fine levels of discretization, and the practical limitation of the computational time. In this case, three different meshes were created in order to compare the stress variation between the differently meshed structures. The tested meshes involved elements with edge lengths of the order of three millimeters, four millimeters and five millimeters.

A stress evaluation was performed on the structure for each mesh in order to evaluate the relative differences between the stress values and computing time. It is important to refer that the analyses are performed by varying some PATRAN stress evaluation parameters, namely the averaging domain and the extrapolation rules. The averaging domain must be defined for element based quantities that are displayed at node locations because multiple values may occur in nodes shared by multiple elements. On the one hand, if the domain averaging is not applied, each element retains its result value at its nodes, causing irregular fringe plots with stress and strain discontinuities at element boundaries. On the other hand, if the averaging domain is set to all entities, all elements surrounding a node contribute to the averaging process and receive the averaged result, creating smooth fringe plots. The extrapolation rule refers to the algorithm to be used when element results are provided to PATRAN at quadrature points and extrapolation is necessary to obtain the results at the element nodes or centroid. Various extrapolation rules are available. The shape functions extrapolation method is based on mapping the output locations to an element topology so that known interpolation functions of that topology are used to compute results at nodes. As an example, if there are thirty-two output results related to thirty-two quadrature points in a Hex26 element, these thirty-two points can be considered part of a virtual new element Hex32. The results at the Hex26 nodes are obtained through interpolation once the results of the Hex32 are available. More simple is the centroid extrapolation method, which is simply based on the extrapolation of the analysis result from its initial location to the centroid of the element.

The stress estimations are focused on the areas where stresses are decisive for the design of the structure, which are identified with a red circle in Figure 4-8 for the Ratterkerb3 load case, Figure 4-9 for the Ludwigskerb load case and Figure 4-10 for the Bremsen load case. Localized contour plots of the Von Misses stresses in those regions are also given in the same figures, with the red areas corresponding to the larger stress values. It should be noted that for the Ratterkerb3 and Ludwigskerb load cases the area where the maximum stress is obtained is the same. It is also relevant to refer that the stress peaks occurring in the load and constraint

application points are neglected because of the well-known singularity problem occurring in these areas.

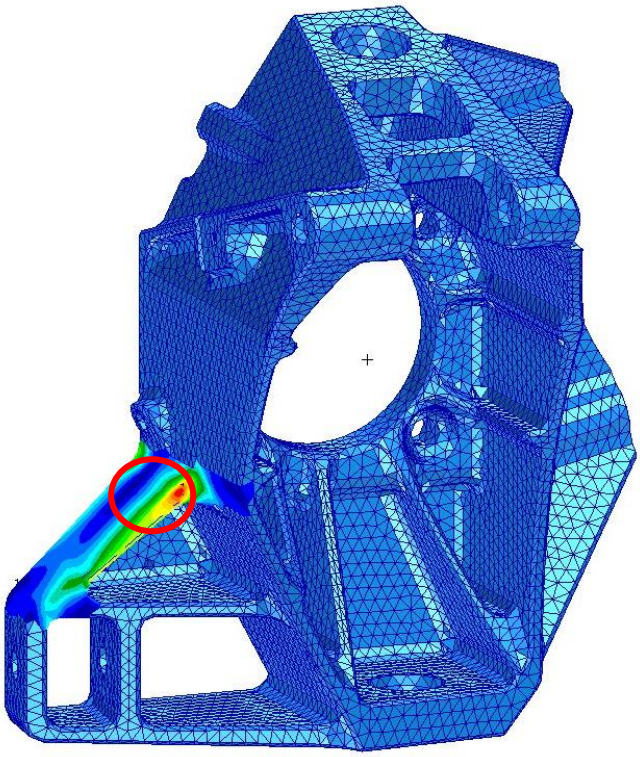

Figure 4-8 - Maximum stress area for the Ratterkerb3 load case

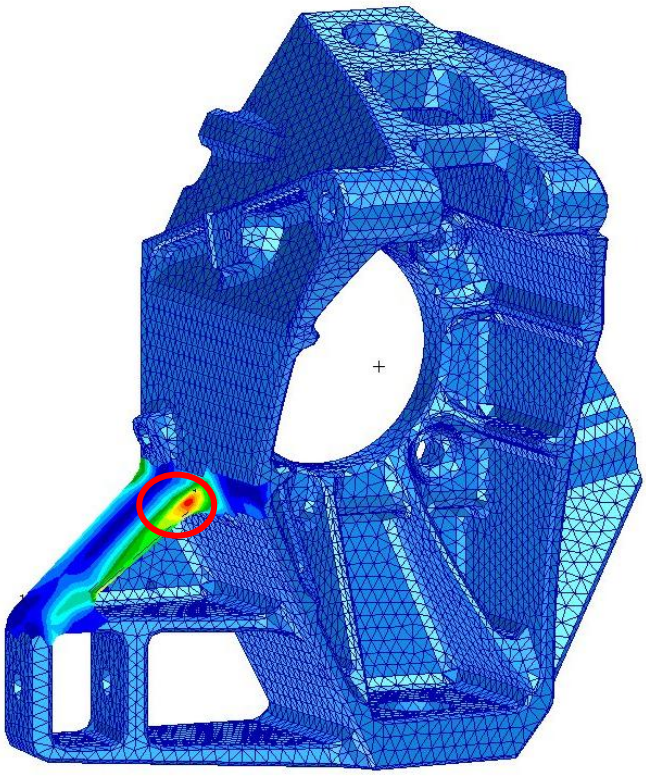

Figure 4-9 - Maximum stress area for the Ludwigskerb load case

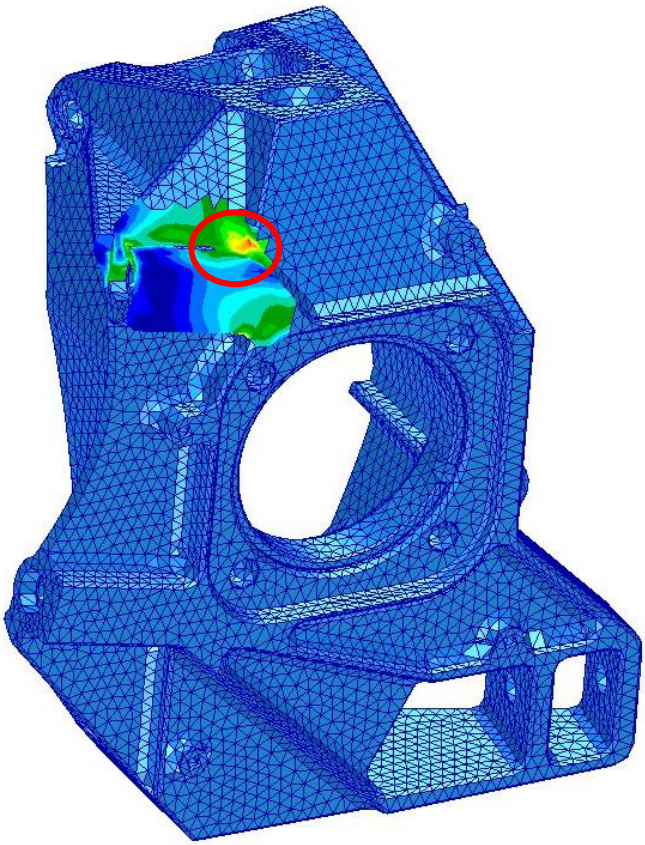

Figure 4-10 – Maximum stress area for the Bremsen load case

The maximum Von Misses stress values obtained for each mesh are specified in Tables 12 to 14, along with the averaging definitions. A graphical comparison between the stress values corresponding to the various averaging/extrapolation options is given in Figures 4-11 to 4-13.

Element Dominant Edge Length: 3 mm		
Averaging definition	**Stress evaluation**	
	Load Case	**Maximum Von Misses stress [MPa]**
Domain: All entities **Extrapolation: Shape functions**	Ratterkerb3	136,73
	Ludwigskerb	174,34
	Bremsen	79,28
Domain: All entities **Extrapolation: Centroid**	Ratterkerb3	118
	Ludwigskerb	147,84
	Bremsen	68,67
Domain: None **Extrapolation: Shape functions**	Ratterkerb3	143,16
	Ludwigskerb	182,44
	Bremsen	86,85
Domain: None **Extrapolation: Centroid**	Ratterkerb3	120,20
	Ludwigskerb	150,92
	Bremsen	69,74

Table 12 - Maximum stress for the mesh with dominant edge length of 3 mm

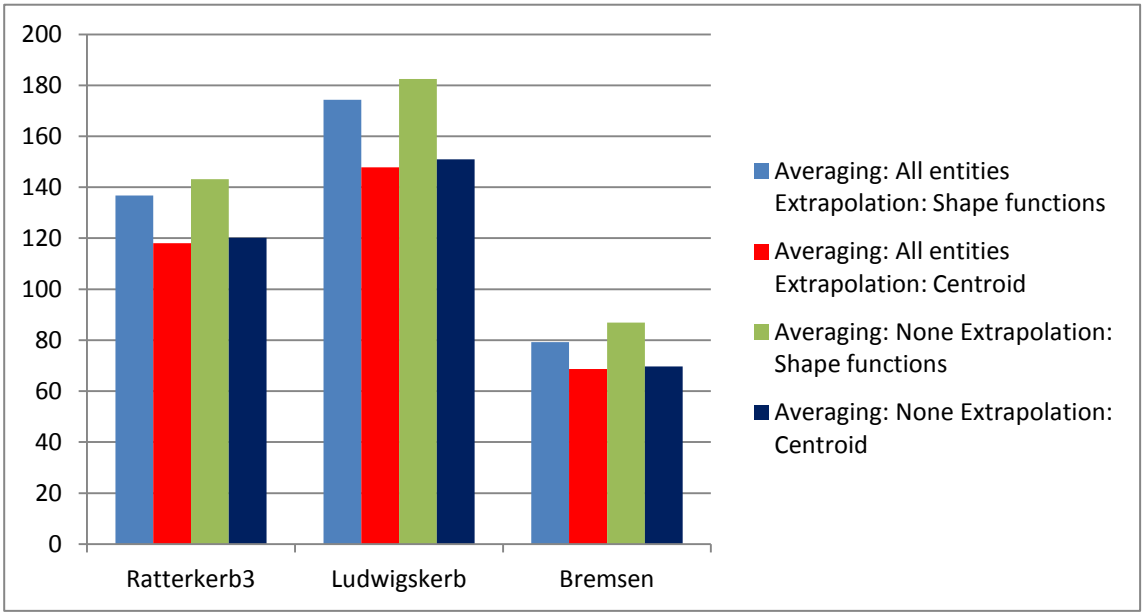

Figure 4-11 - Comparison between the stress values for the different averaging definitions for a mesh with dominant edge length of 3 mm

Element Dominant Edge Length: 4 mm		
Averaging definition	**Stress evaluation**	
	Load Case	**Maximum Von Misses stress [MPa]**
Domain: All entities **Extrapolation: Shape functions**	Ratterkerb3	134,61
	Ludwigskerb	171,31
	Bremsen	88,21
Domain: All entities **Extrapolation: Centroid**	Ratterkerb3	118,16
	Ludwigskerb	148
	Bremsen	64,70
Domain: None **Extrapolation: Shape functions**	Ratterkerb3	140,16
	Ludwigskerb	178,16
	Bremsen	99,29
Domain: None **Extrapolation: Centroid**	Ratterkerb3	120,20
	Ludwigskerb	150,90
	Bremsen	65,58

Table 13 - Maximum stress for the mesh with dominant edge length of 4mm

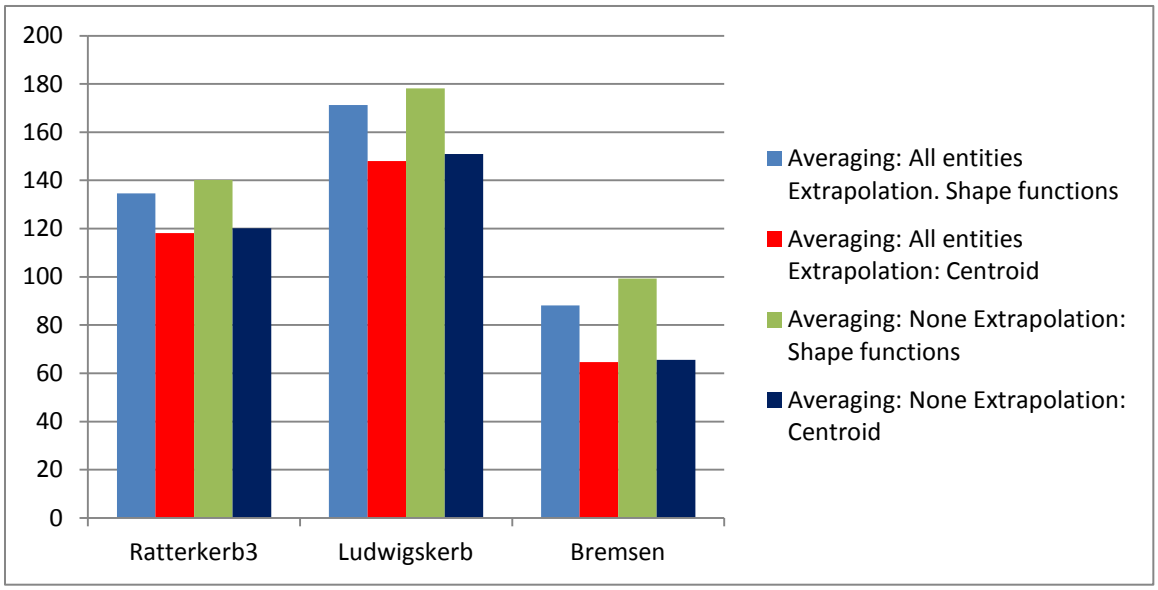

Figure 4-12 - Comparison between the stress values for the different averaging definitions for a mesh with dominant edge length of 4 mm

Element Dominant Edge Length: 5 mm		
Averaging definition	**Stress evaluation**	
	Load Case	**Maximum Von Misses stress [MPa]**
Domain: All entities **Extrapolation: Shape functions**	Ratterkerb3	131,28
	Ludwigskerb	165,78
	Bremsen	73,79
Domain: All entities **Extrapolation: Centroid**	Ratterkerb3	112,93
	Ludwigskerb	140,45
	Bremsen	52,93
Domain: None **Extrapolation: Shape functions**	Ratterkerb3	132,68
	Ludwigskerb	167,97
	Bremsen	101,33
Domain: None **Extrapolation: Centroid**	Ratterkerb3	113,87
	Ludwigskerb	142,05
	Bremsen	53,10

Table 14 - Maximum stress for the mesh with dominant edge length of 5 mm

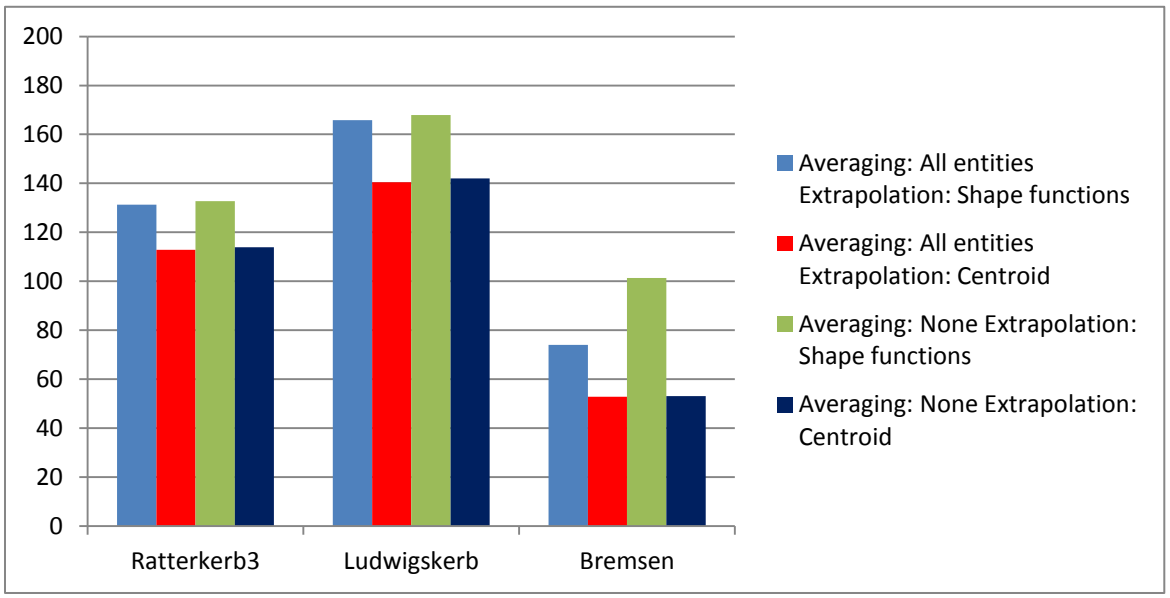

Figure 4-13 - Comparison between the stress values for the different averaging definitions for the mesh with dominant edge length of 5 mm

Figures 4-11 to 4-13 suggest that the choice of the extrapolation rule is much more relevant for the overall accuracy of the results than the choice of the averaging domain. Indeed, the averaging seems to make virtually no difference between the results when the centroid extrapolation is performed and is only practically relevant (37,3%) in the Bremsen load case with the shape function extrapolation. On the other hand, there is a clear difference between the results using different rules of extrapolation, which reaches almost 100% for the Bremsen load case on the coarser mesh. Thus, for stress evaluation purposes the averaging domain was set to all entities and the extrapolation rule was set to the shape functions. This choice was made based on the fact that the definition of shape functions, rather than the centroid, as extrapolation rule yields higher stress values for all load cases and the variation of the averaging domain results in no relevant stress variations, except for the Bremsen load case. Although there is a relevant stress variation for this load case, the stress values obtained by setting the averaging domain to all entities were considered acceptable and preferred over a more conservative approach, when the averaging is not applied.

Finally, the stress values must be compared for the different tested meshes in order to choose a mesh refinement that grants enough accuracy at a reasonable computational cost. An immediate conclusion when comparing the stress values for the three meshes is that the differences are relatively small. It is thus more profitable to use for the optimization the mesh that saves more computing time. This enables the optimization process to advance without becoming a too time-consuming procedure, reducing the computational effort necessary to perform the optimization. Thus, the mesh chosen to perform the optimization is the mesh with leading element length of five millimeters. The total number of DOF of this mesh is 891024. Figures 4-14 and 4-15 represent the mesh used on the structure.

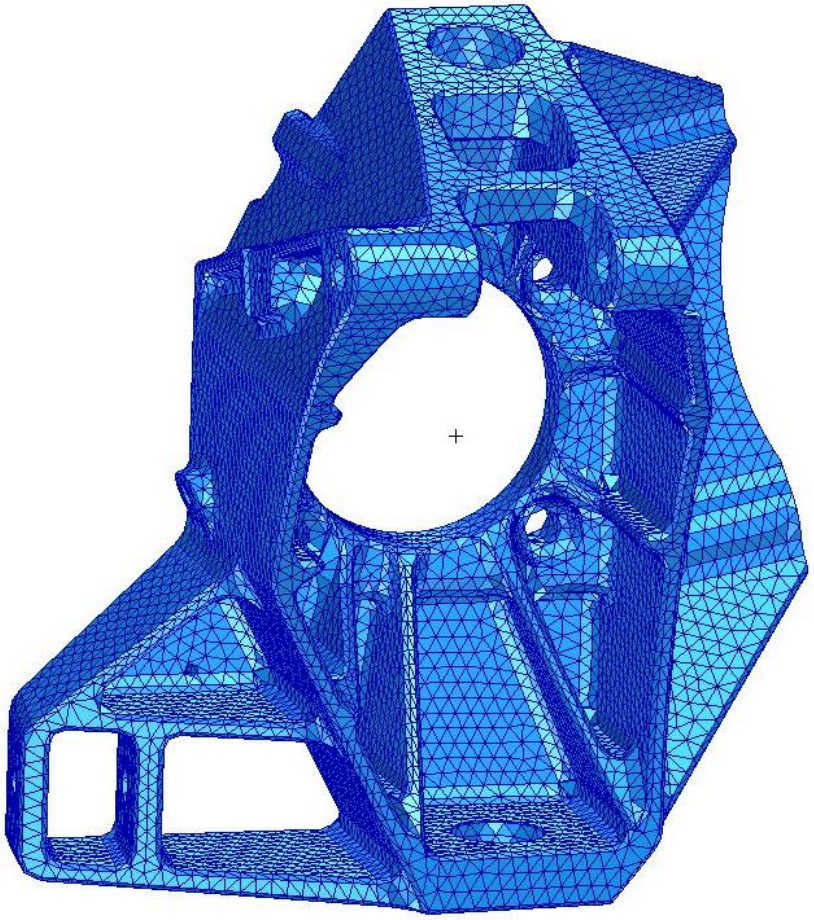

Figure 4-14 - Front view of the meshed structure

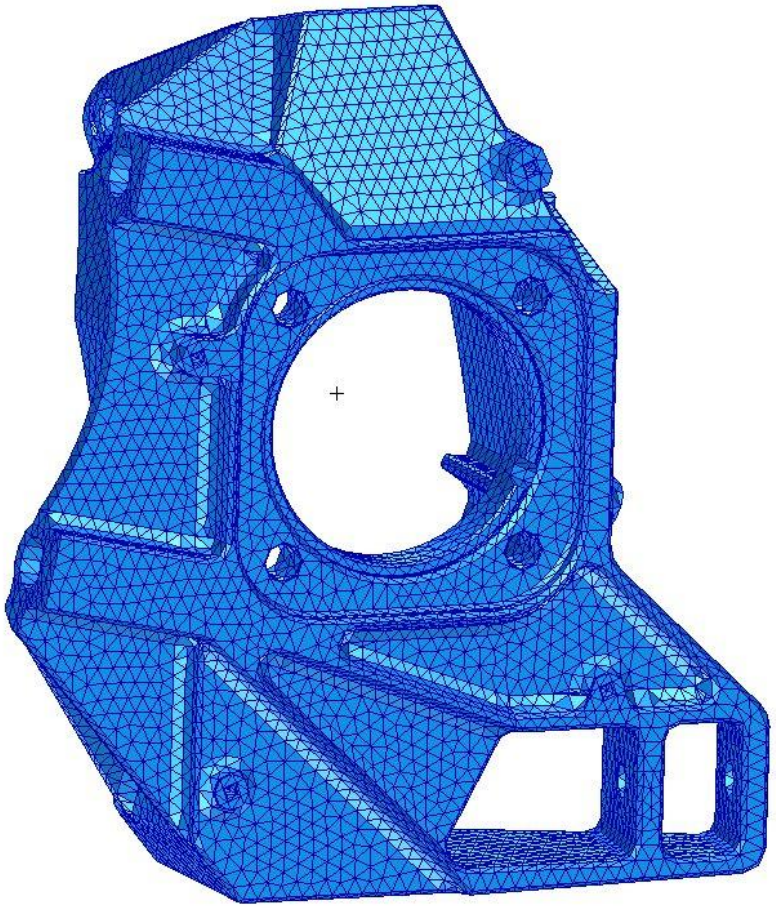

Figure 4-15 - Back view of the meshed structure

4.5 Linear static analysis

Once the finite element mesh is defined, it is possible to perform a basic structural evaluation, previous to the optimization, under linear static conditions. This enables the evaluation of the stresses and displacements occurring in the non-optimized structure and defines the basis for the comparison between the non-optimized and optimized structures. The maximum stresses that arise from the linear static analysis of the non-optimized structure are presented in Table 15 for each load case. It should be noted that these stresses occur in the maximum stress zones represented in Figures 4-8 to 4-10.

Load Case	Maximum Von Misses stress [MPa]
Ratterkerb3	131,28
Ludwigskerb	165,78
Bremsen	73,79

Table 15 - Maximum stress values in the non-optimized structure

The stress distribution for each load case is presented, for the entire structure, in Figures 4-16 to 4-18. For all load cases, the areas in red correspond to larger stresses and the blue color corresponds to smaller stresses. As previously referred, the stress peaks occurring in the load application and constrained areas are neglected, being thus removed from the analysis. For the Ratterkerb3 load case, the stress field is shown in Figure 4-16. It is possible to verify that the larger stresses occur in the lower part of the structure. Although there are some stress concentrations in the lower right section of the structure, the most relevant area regarding this load case, from the stress evaluation point of view, is located at the rib, where the largest stresses occur. For the Ludwigskerb load case, the stress distribution is shown in Figure 4-17. As for the Ratterkerb3 load case, the Ludwigskerb load case generates larger stresses in the lower part of the structure, with stress concentration areas in the lower right part and high stresses occurring at the rib on the left side.

For both Ratterkerb3 and Ludwigskerb load cases, the area where the stressses reach their maximum is the same. This area is therefore highly relevant for the design of the part.

For the Bremsen load case, the stress distribution is presented in Figure 4-18. Unlike the previous load cases, here the larger stresses occur in the vicinity of the top vein, located at the left upper part of the structure. This is the most affected area by the application of the Bremsen load case.

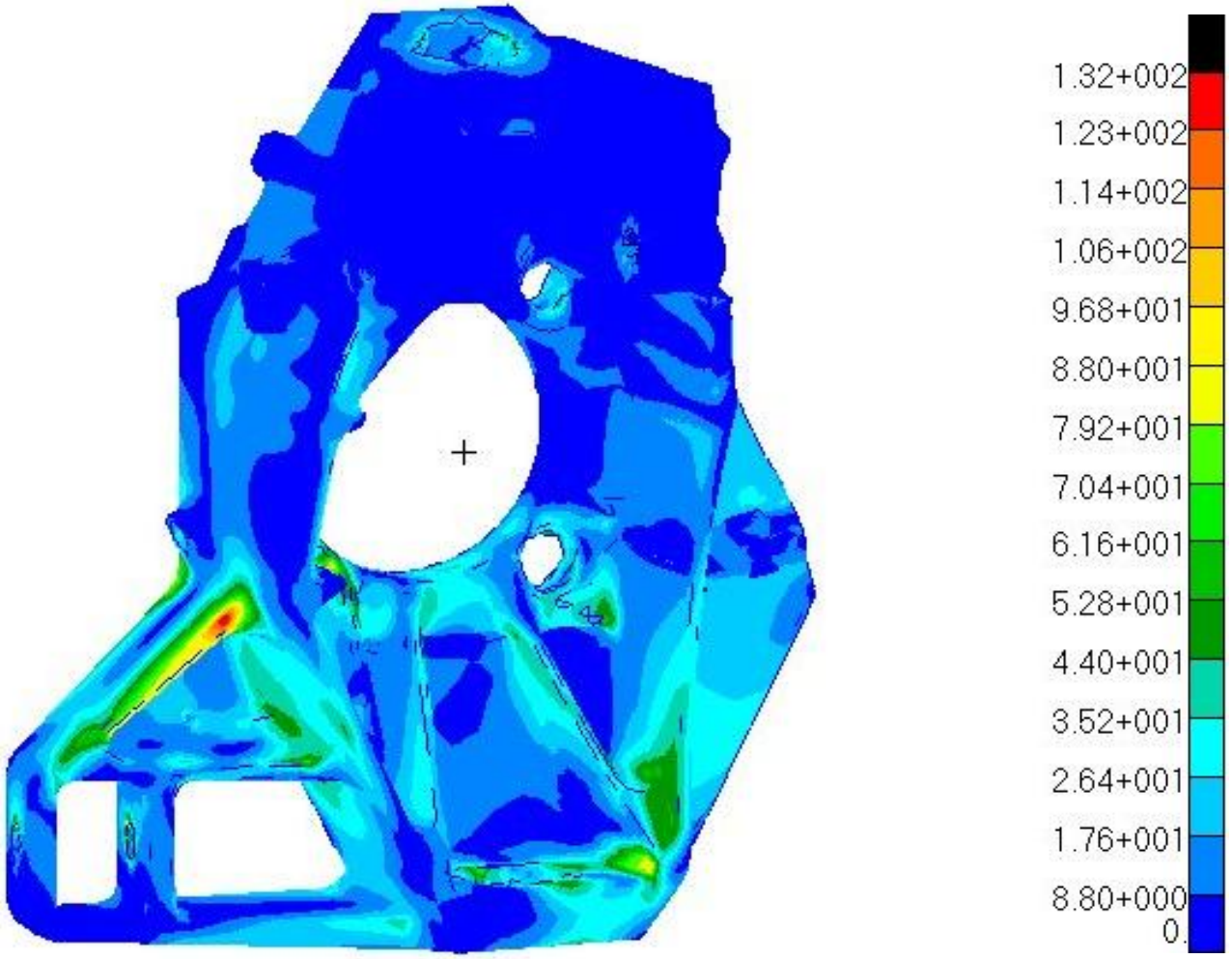

Figure 4-16 - Stress distribution for the Ratterkerb3 load case

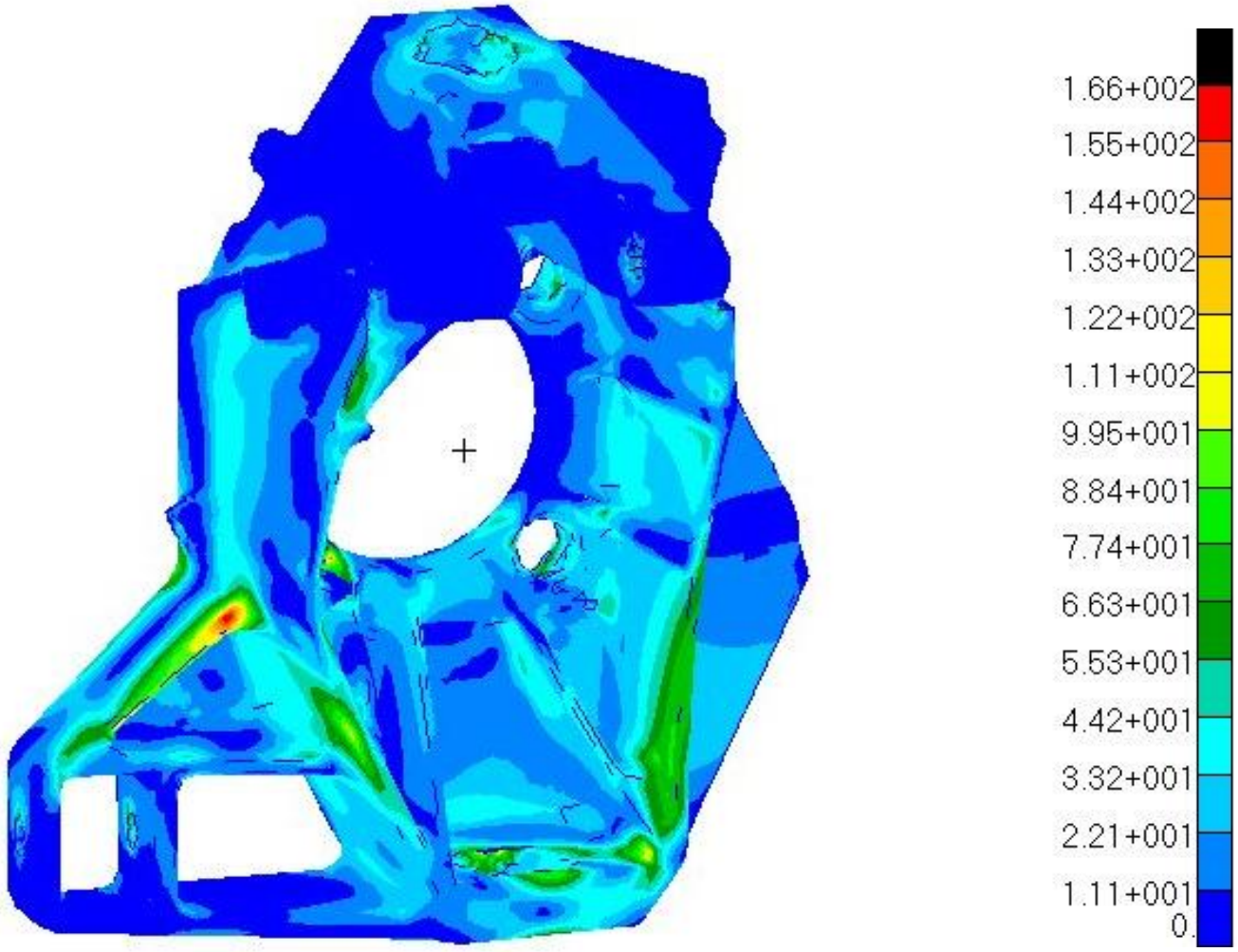

Figure 4-17 - Stress distribution for the Ludwigskerb load case

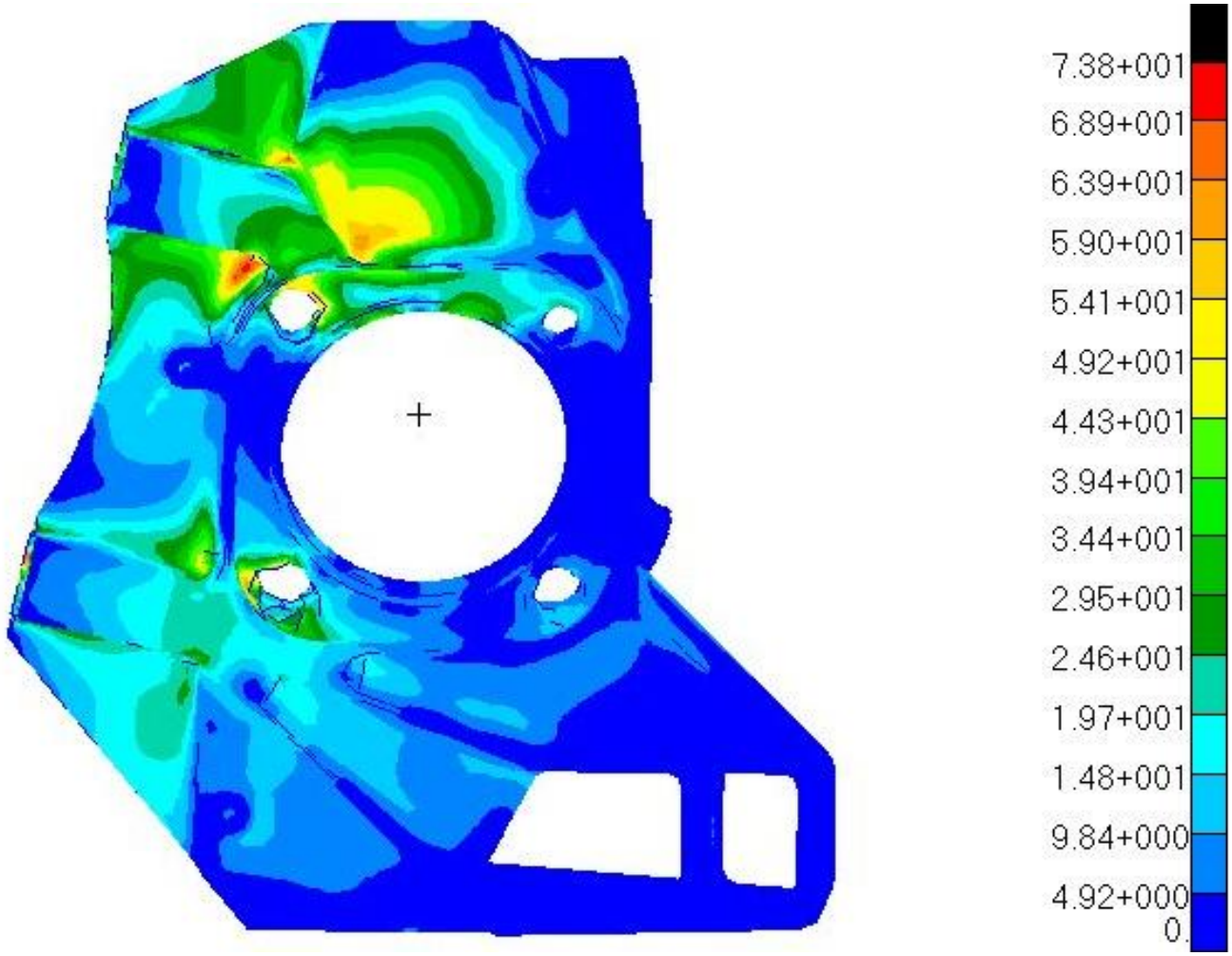

Figure 4-18 - Stress distribution for the Bremsen load case

The maximum displacements obtained in the wheel carrier are presented in Table 16.

Load case	Maximum displacement [mm]
Ratterkerb3	0,495
Ludwigskerb	0,580
Bremsen	0,0788

Table 16 - Maximum displacement values in the non-optimized structure

The displacement fields for the tested load cases are presented in Figures 4-19 to 4-23. For comparison purposes, the undeformed structure, represented by the black finite element mesh, is also plotted in the same figures. Consequently, at some locations where the displacements maximize, the mesh is overlapped by the deformed structure.

For the Ratterkerb3 load case, presented in Figure 4-19, the maximum displacement occurs at the lower left section of the structure. This area is shown in more detail in Figure 4-20, in which the deformed structure is represented in black and the undeformed structure in blue. It is clear that the major component of the displacement occurs in the Z direction. This is caused by the application of a force of around 6,8kN along that direction in the load introduction point D located at the lower left section of the structure.

The displacement field for the Ludwigskerb load case is shown in Figure 4-21. For this load case, the area where the maximum displacement is reached is the same as for the Ratterkerb3 load case. Although the displacement fields of both Ratterkerb3 and Ludwigskerb load cases are similar in shape, the latter load case produces larger displacements than the Ratterkerb3 load case due to the higher intensities of the applied forces.

For the Bremsen load case, the displacement field shown in Figure 4-22 presents lower displacements than those obtained for the other two load cases. For this load case, the maximum displacement occurs in the vicinity of the application point of the Bremsen moment. This area is presented in more detail in Figure 4-23. It is clear that the major component of the displacement of this section occurs in Y direction. This is explained by the application of the braking moment around Z direction, which generates large displacements in the Y direction in the vicinity of the moment application point.

It is important to refer that there is a maximum allowable displacement of 1.0mm defined for this type of wheel carrier. The values of displacement obtained are below the allowable displacement value and hence the structural safety is not compromised.

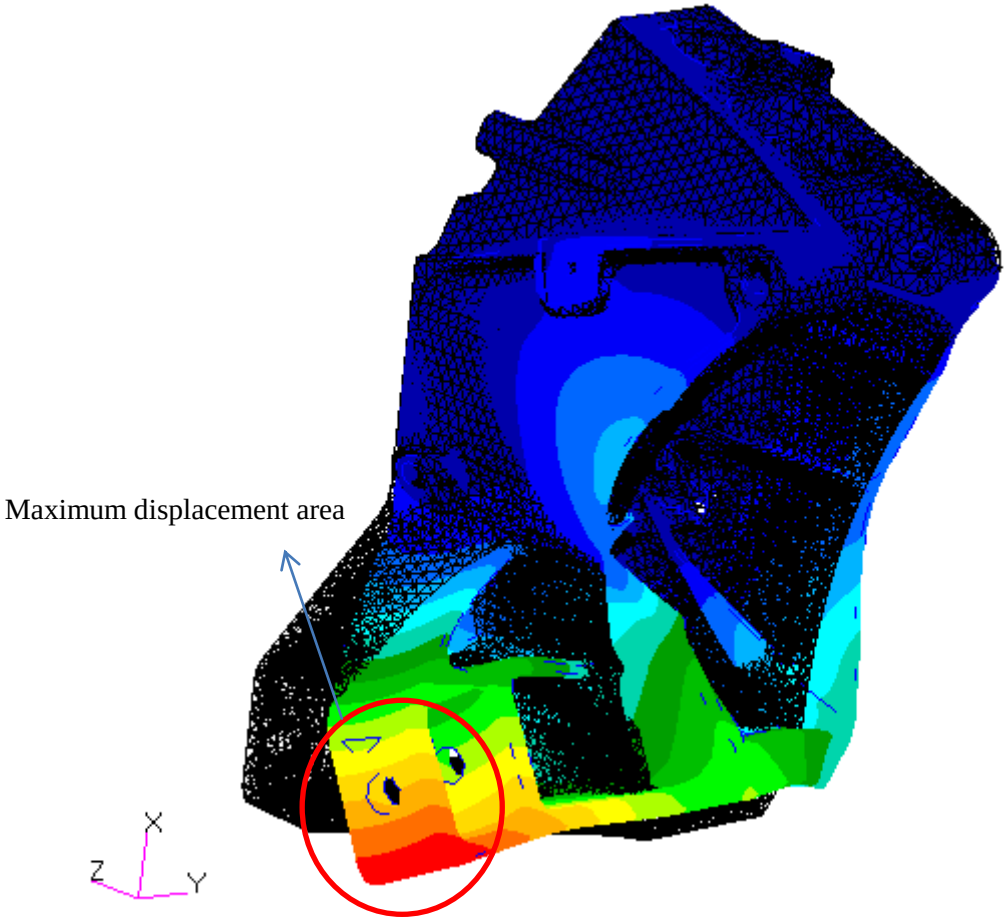

Figure 4-19 - Deformed structure for the Ratterkerb3 load case

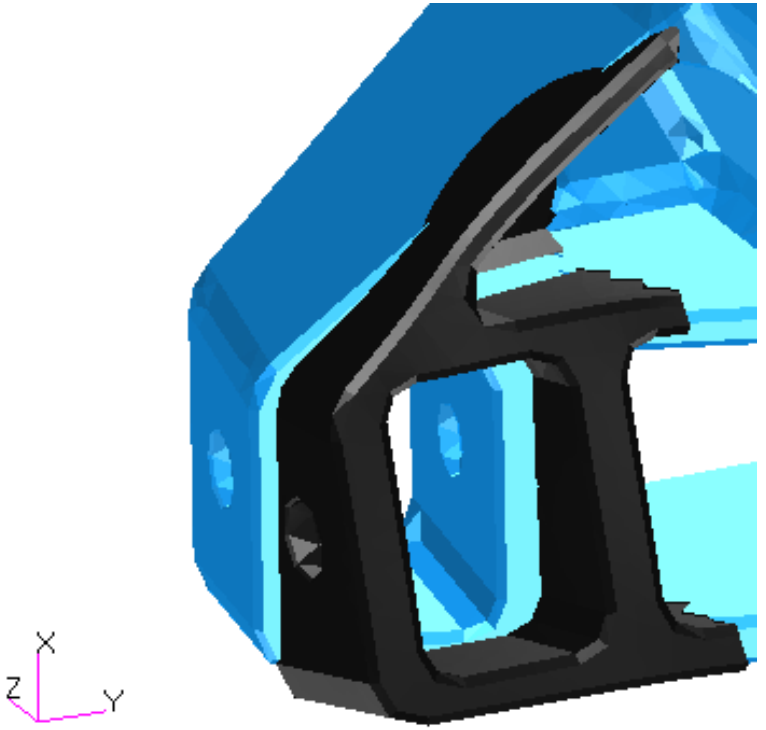

Figure 4-20 - Maximum displacement area for the Ratterkerb3 load case

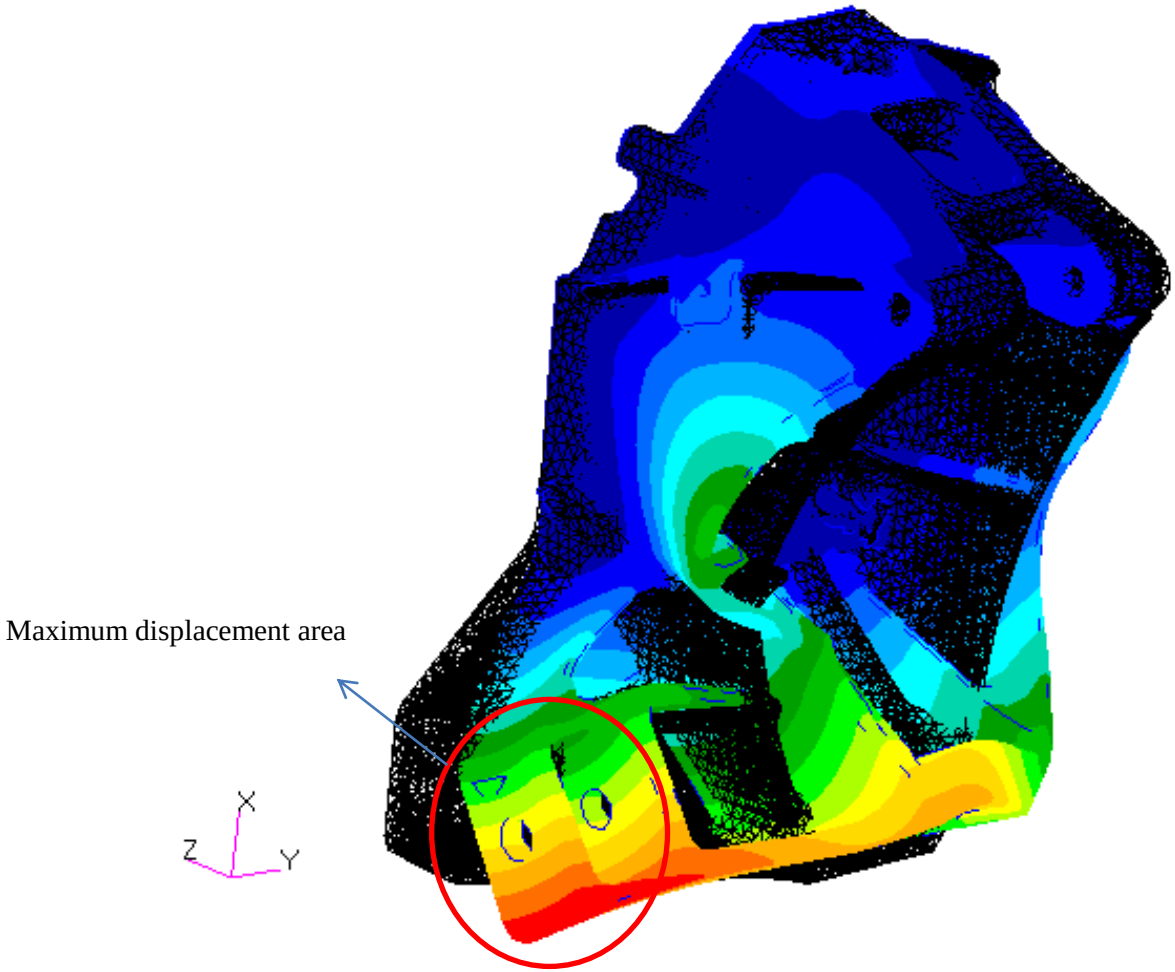

Figure 4-21 - Deformed structure for the Ludwigskerb load case

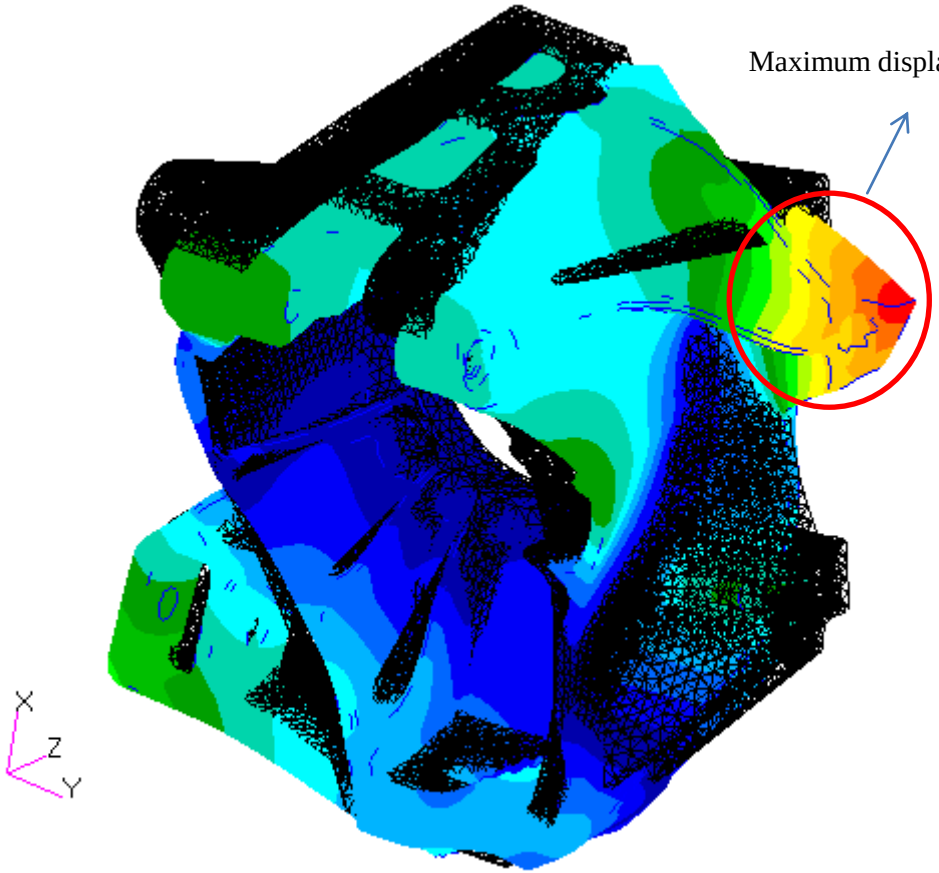

Figure 4-22 - Deformed structure for the Bremsen load case

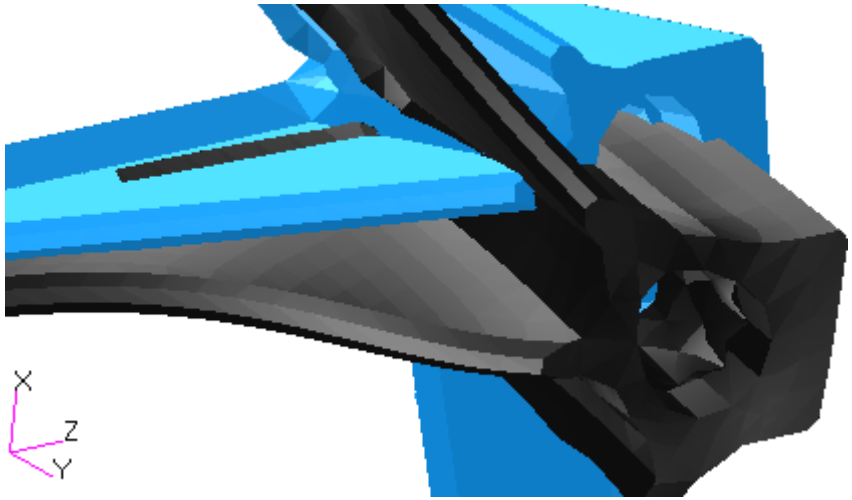

Figure 4-23 - Maximum displacement area for the Bremsen load case

4.6 Topology optimization

After choosing the finite element mesh to use and performing the linear static analysis on the non-optimized structure, the topology optimization of the wheel carrier took place. The topology optimization is based on the already described density method theory, which implies the establishment of an element density value according to the intensity of the stresses in the structure. The value of the density of each element is compared with an established threshold value and the elements with a relative density lower than this value are eliminated from the basic topology result.

The main goal of the wheel carrier optimization procedure is to reduce its weight through the element elimination procedure already described. This concept, which stands at the basis of the topology optimization procedures, enables an optimal material distribution on a structure, given the initial design space, leading to the structural weight reduction and the consequent cost savings and performance improvements.

The aim of the optimization reported here was to reduce the weight of the wheel carrier between 10% and 20% of the initial weight. As the wheel carrier stands as a relatively small component of the vehicle structure, with a non-optimized weight of 3.589 kg, its weight reduction is rather small when considering the whole structural weight of the vehicle. However, taking into account the mass production that characterizes the automotive domain, it is easily understood that even a small weight reduction may provide a significant cost reduction in the mass production of the cars.

As an initial step of the optimization procedure, it is necessary to distinguish between the areas that are included in the process and the areas that are not. In most structures there are areas that are simply impossible to reduce due to the important role they play in the structural design. The wheel carrier contains several such areas, identified in red in Figure 4-24, that are discarded from the optimization process because they represent connection points between the wheel carrier and the remaining vehicle structure and hence are important to the structural design. To exclude these areas from the optimization process, a new property is created and applied to the elements they contain and once the optimization parameters are defined, this new property is simply excluded from the analysis, so that only the elements that are not assigned to this property are included in the optimization process.

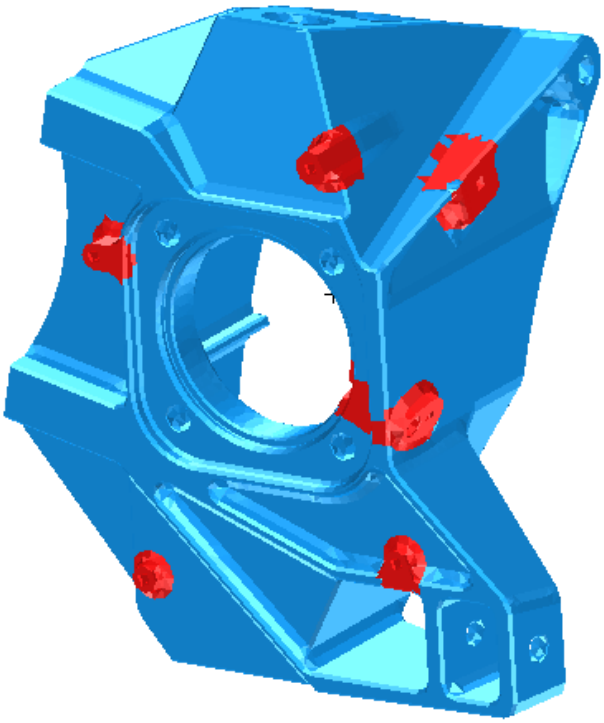

Figure 4-24 - Identification of the areas discarded from the optimization

The general optimization procedure took place by defining the main parameters for the optimization loops. The most important parameter, the mass target constraint, enables the definition of the percentage of material to save. Thus the process was started by entering a value of 0.8, which means that the optimization procedure should keep 80% of the initial material.

The result of the optimization for the threshold value of 0.0 and a reduction of 10% of material is presented in Figures 4-25 and 4-26. This result shows the different relative densities of the elements and offers an idea about the areas where the targeted material reduction is possible. The result shows that the areas of material reduction are mainly concentrated in specific structural parts, identified by the groups of white elements, rather than isolated elements spread along the structure. These zones correspond to low values of Von Misses stresses and are thus identified as potential areas for optimization.

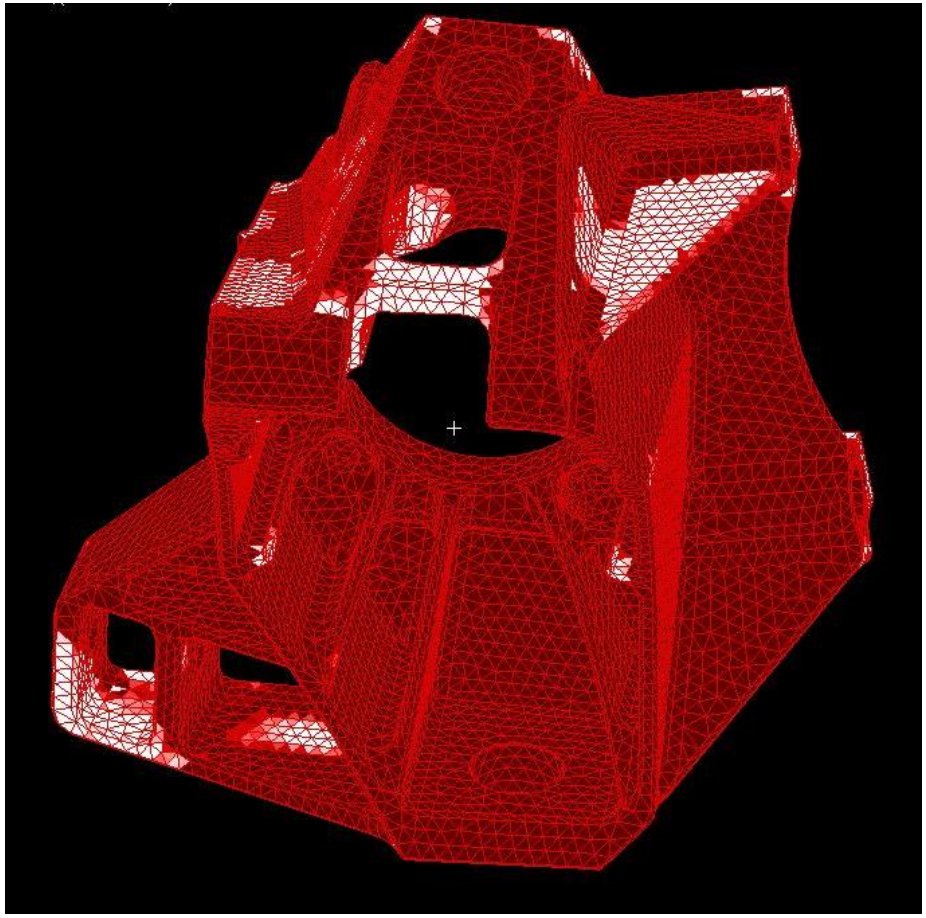

Figure 4-25 - Basic topology result for material reduction of 10% and threshold value of 0.0

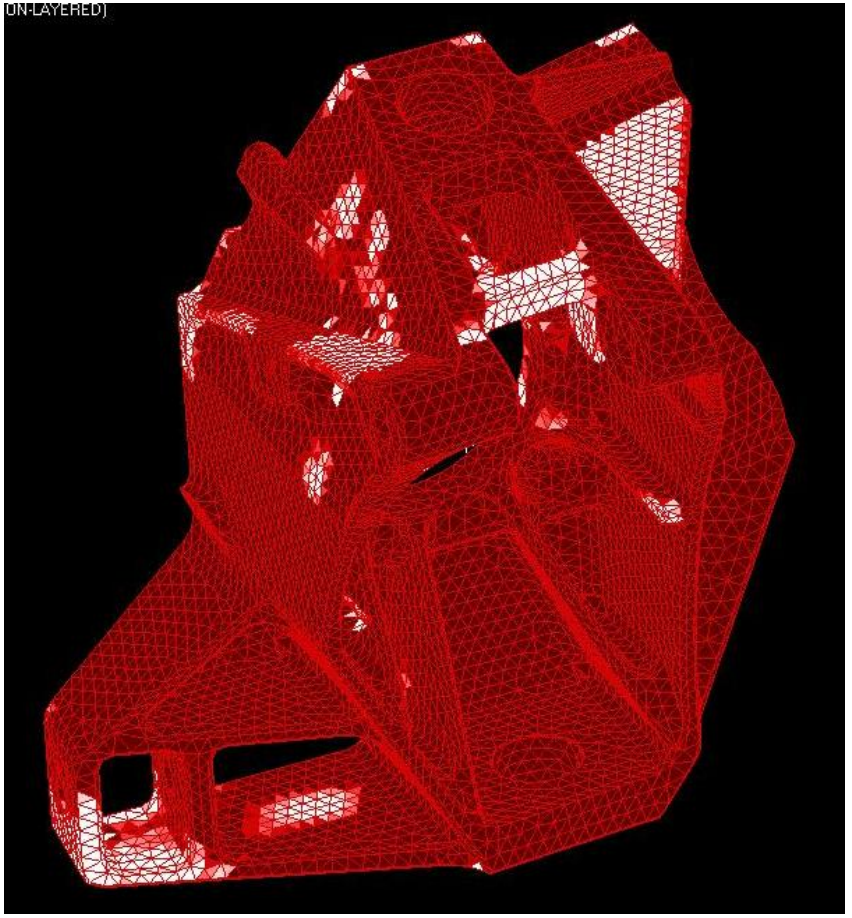

Figure 4-26 - Basic topology result for material reduction of 10% and threshold value of 0.0

In Figures 4-27 and 4-28 the output of the optimization loop for a material reduction of 20% is presented. As for the 10% reduction, a threshold value of 0.0 was chosen to enable a clear verification of the areas with concentration of low density elements and a comparison between both basic topology results of 10% and 20% material reduction. It is possible to verify that, although larger, the main material reduction areas are the same. The comparison between the optimization results for the 10% and 20% material reductions shows that there are no great differences in the outputs and thus the optimization result chosen to create the optimized structure is the one that involves the reduction of 20% of the initial material.

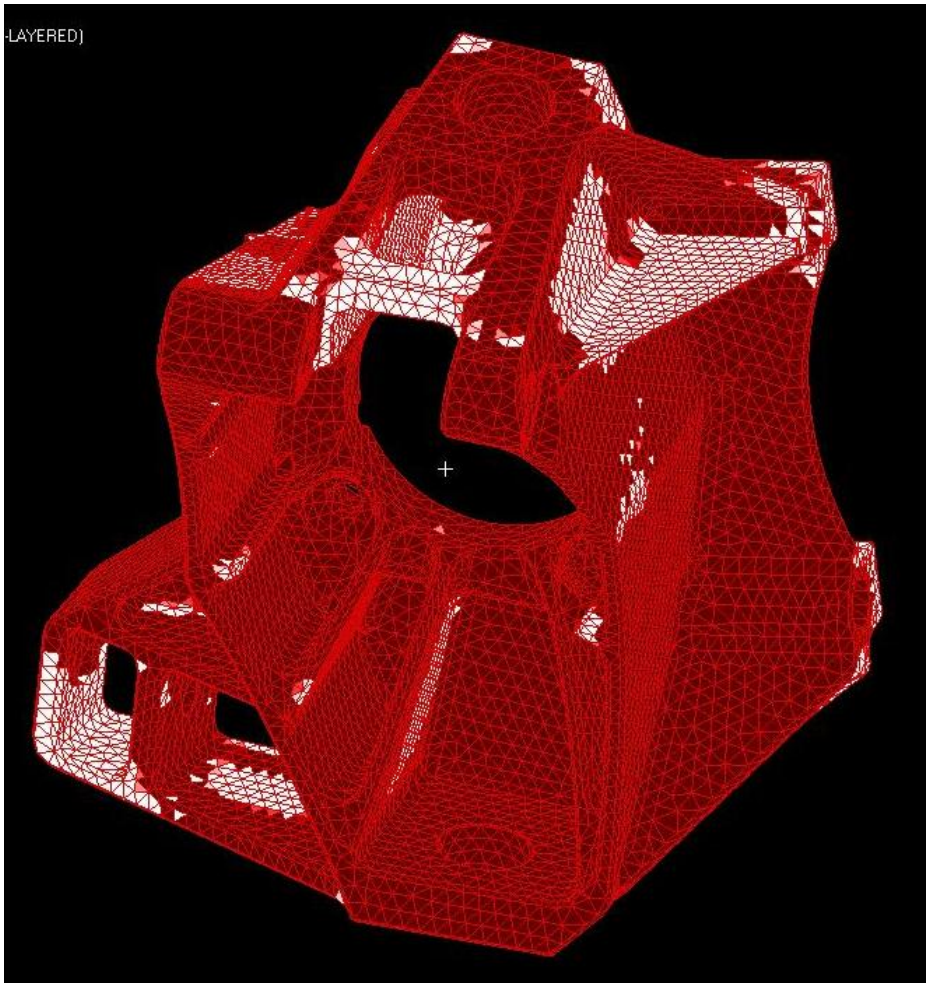

Figure 4-27 - Basic topology result for material reduction of 20% and threshold value of 0.0

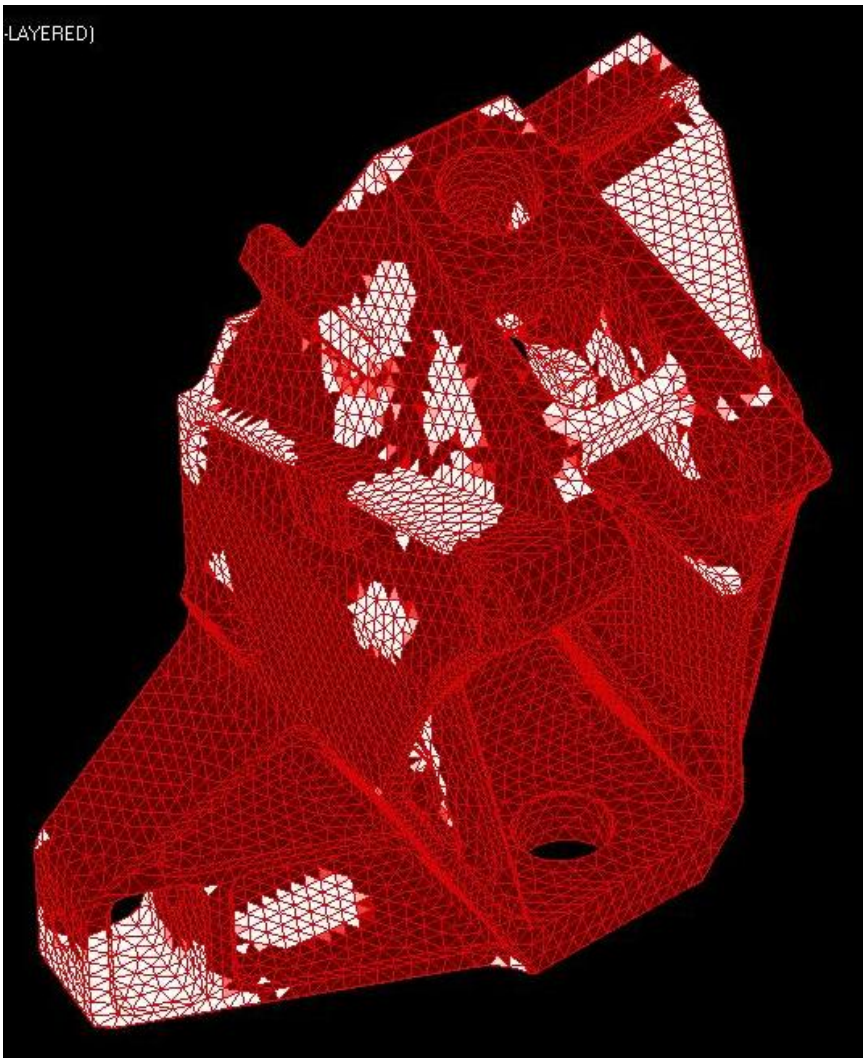

Figure 4-28 - Basic topology result for material reduction of 20% and threshold value of 0.0

The optimized structure was created next based on the information given by the FE models with null thresholds, already presented in the figures above, and by the models with higher thresholds, which involve an actual material reduction and hence offer a preliminary idea about the final shape of the optimized structure. A threshold value of relative density of 0.2 was defined, which enabled the elimination of the elements with relative density below this value. The new optimized structure is presented in Figures 4-29 to 4-31. It should be noted that the models created by removing lower density elements are actually coarse approximations of the optimized structures, as the choice of which elements to eliminate is made by the software alone and is based on a simple evaluation on the relative densities of the elements, thus leaving aside other relevant factors such as the importance of the area for design purposes. This basic topology result is, however, relevant for the design team as it represents an approximation of the final design of the structure.

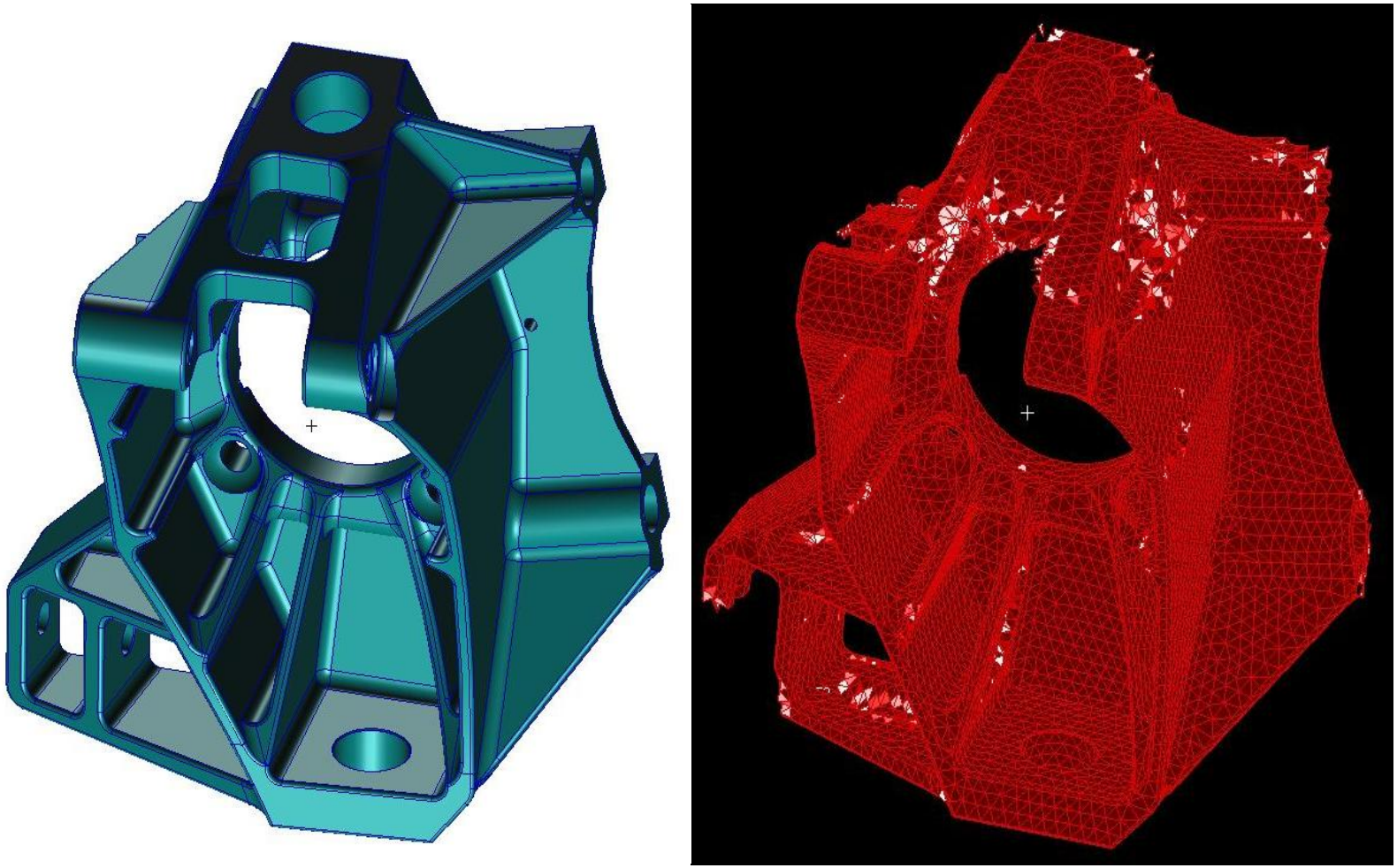

Figure 4-29 - Comparison between the non-optimized structure and the optimized model with a threshold value of 0.2

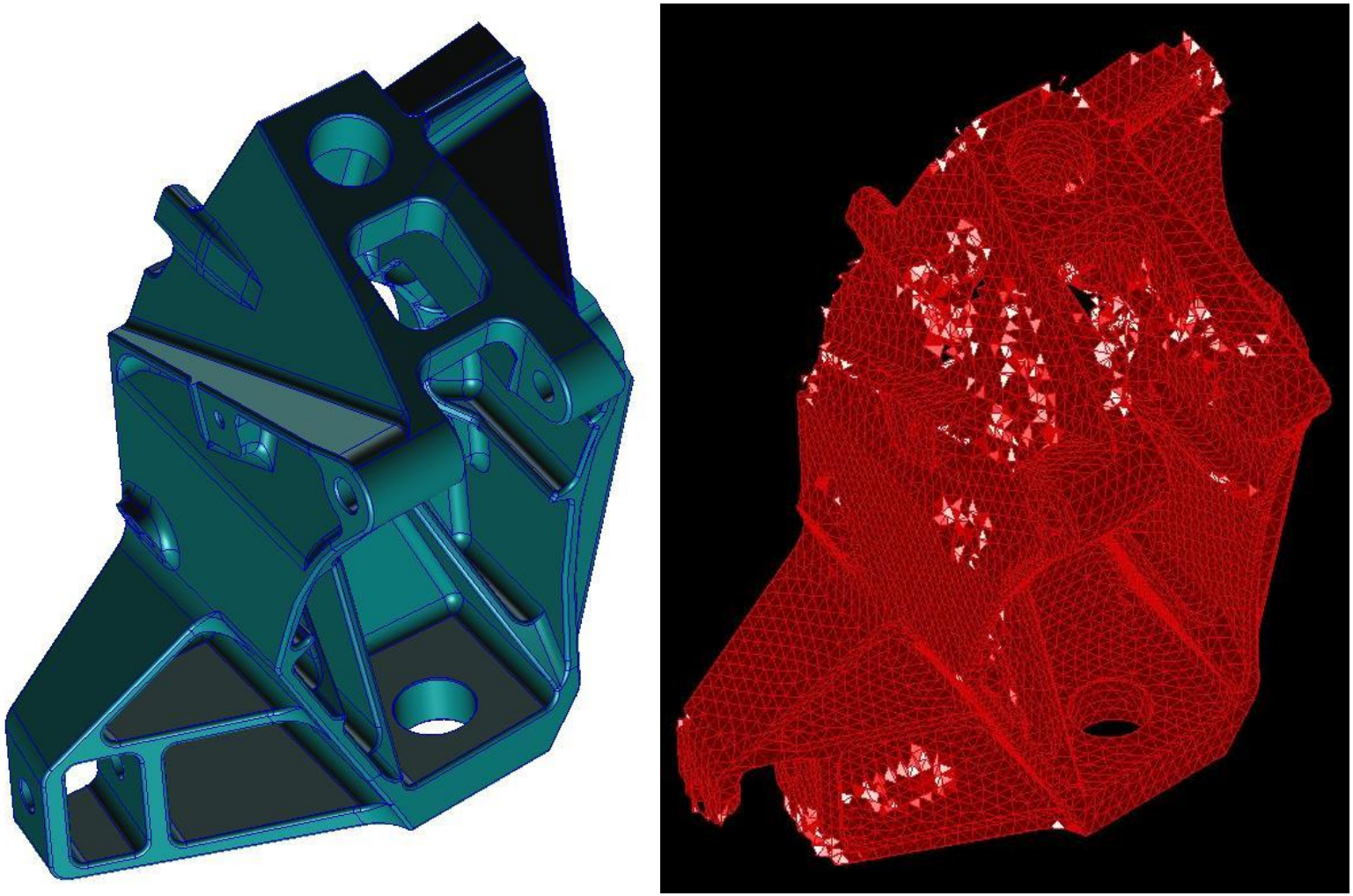

Figure 4-30 - Comparison between the non-optimized structure and the optimized model with a threshold value of 0.2

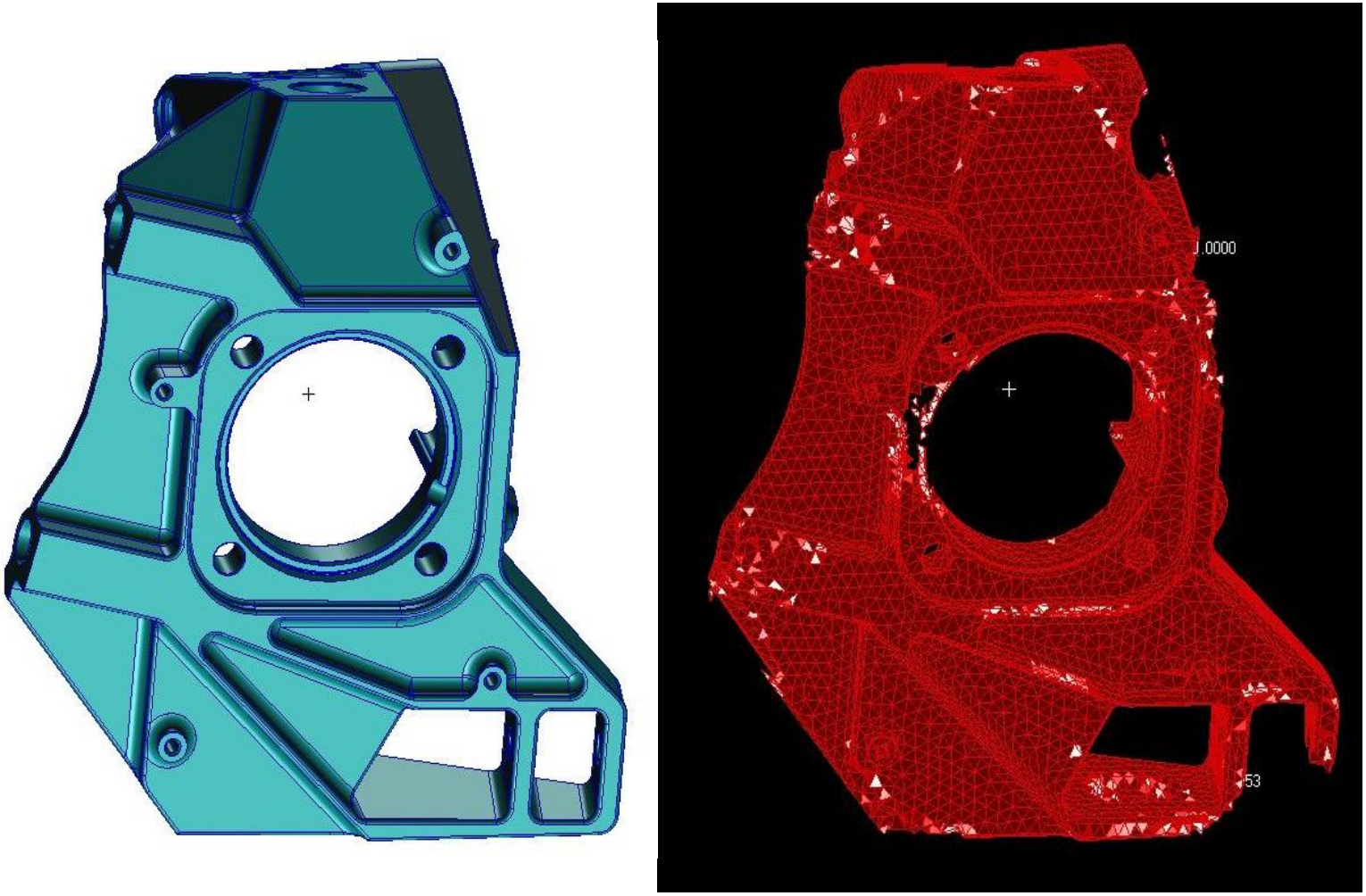

Figure 4-31 - Comparison between the non-optimized structure and the optimized model with a threshold value of 0.2

The evaluation of the optimized structure presented in the figures above shows that there are areas where the material reduction may be accomplished through the creation of holes inside the structure. This typically occurs when the lower relative density elements are concentrated in some particular internal locations. In other cases, the reduction of material may be achieved through the complete elimination of that area. However, the decision to cut off material in the structure must take into account whether the material reduction is feasible or not, based on the structural importance of the areas with optimization potential. For instance, although the output reveals that there are internal areas where the material reduction is possible based on the comparison of the relative density of the elements with the threshold value, the role that those areas play in the behavior of the wheel carrier structure may be relevant and thus the material reduction in those areas is unadvisable. In other cases, the material reduction is not possible in areas with optimization potential because the manufacturing of such optimized parts would be very hard to accomplish.

Taking into account all these considerations, the final design of the optimized structure is presented in Figures 4-32 to 4-35. It corresponds to a reduction of 0.421 kg from the initial mass value of 3.589 kg, that is, approximately 12% mass reduction. Table 17 presents the mass of both optimized and non-optimized structures, the respective difference and the percentage of reduction. It is important to note that the initial 20% reduction target does not correspond to a real 20% mass reduction because of the areas that cannot be eliminated from the structure for the reasons discussed above.

Structure	**Mass [kg]**	**Mass reduction [kg]**	**Percentage of reduction [%]**
Non-optimized	3.589	0.421	11.73
Optimized	3.168		

Table 17 - Mass reduction obtained through optimization

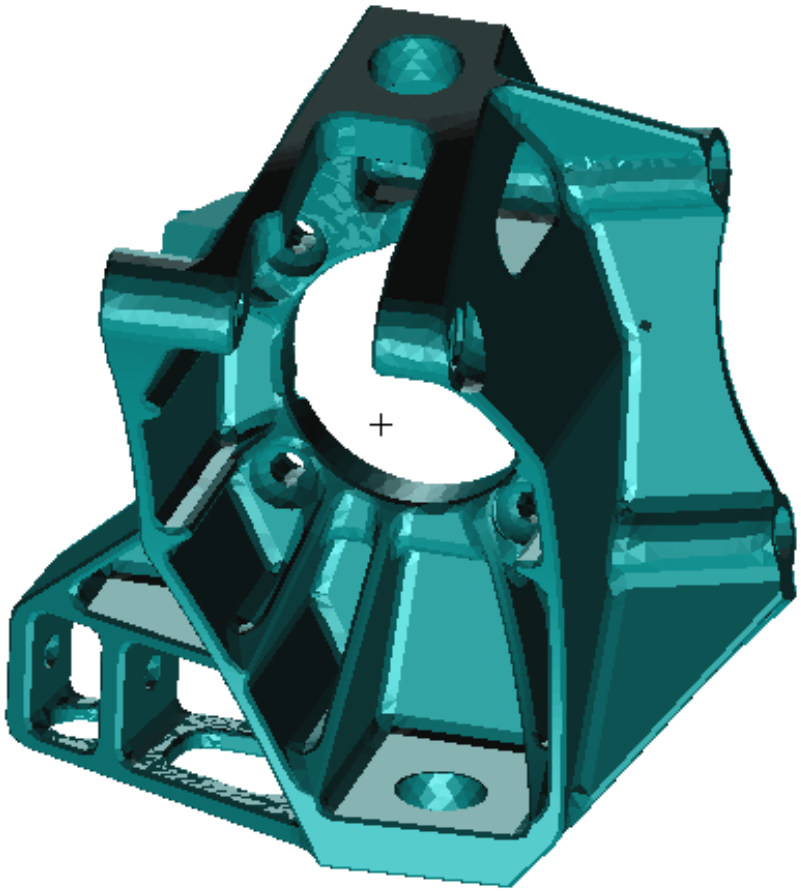

Figure 4-32 - Front view of the optimized wheel carrier

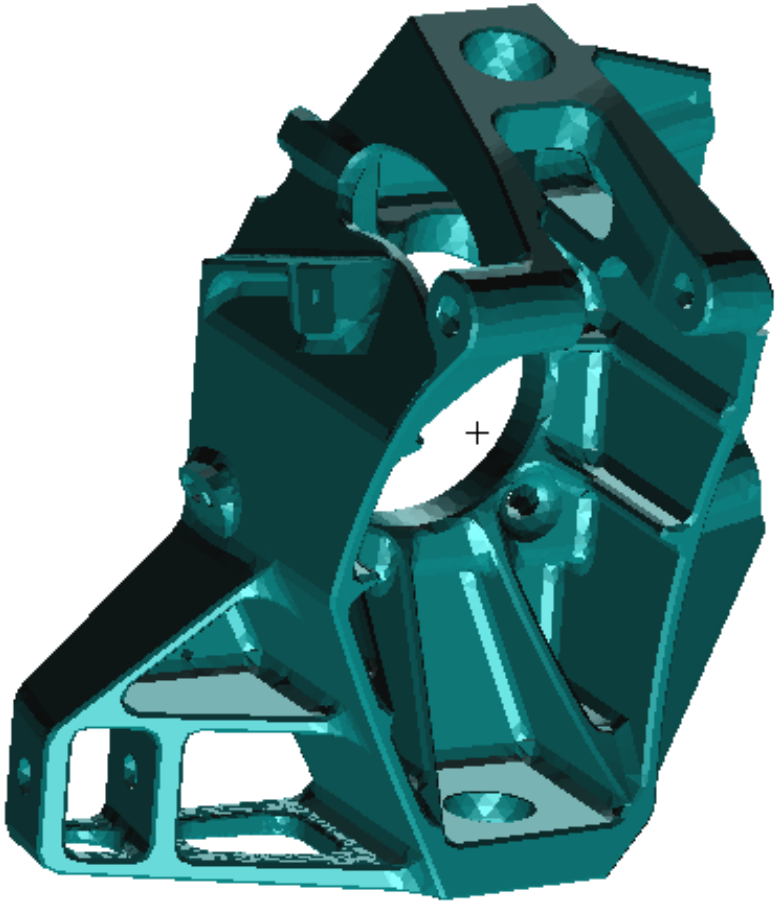

Figure 4-33 - Front view of the optimized wheel carrier

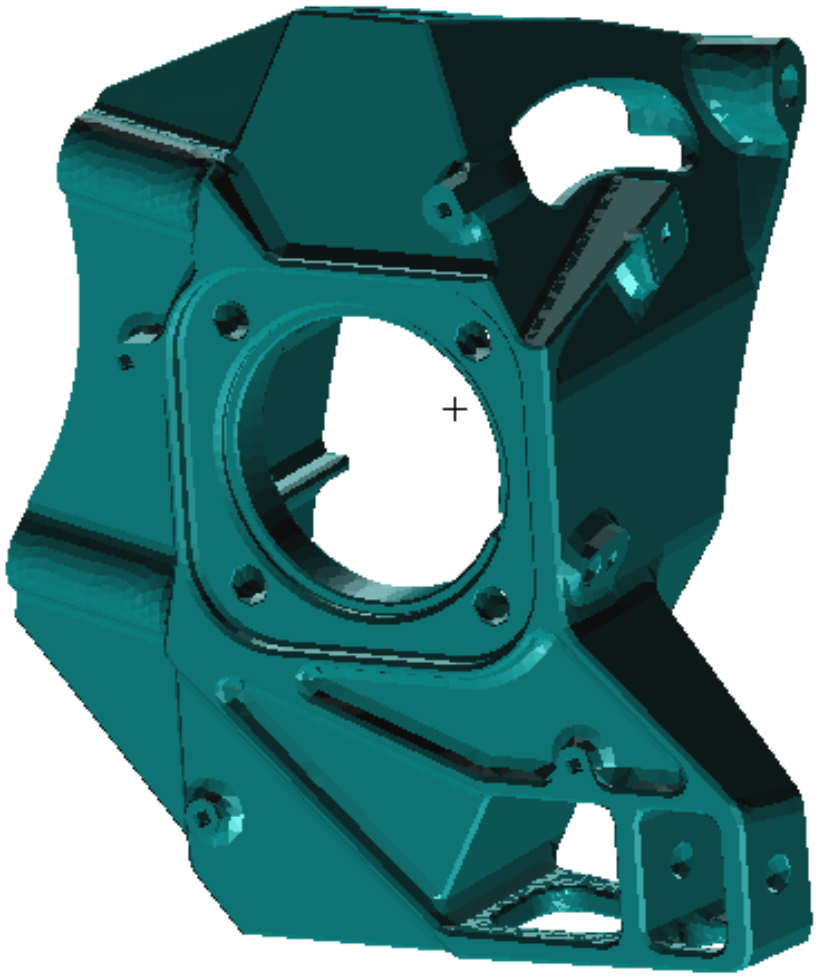

Figure 4-34 - Back view of the optimized wheel carrier

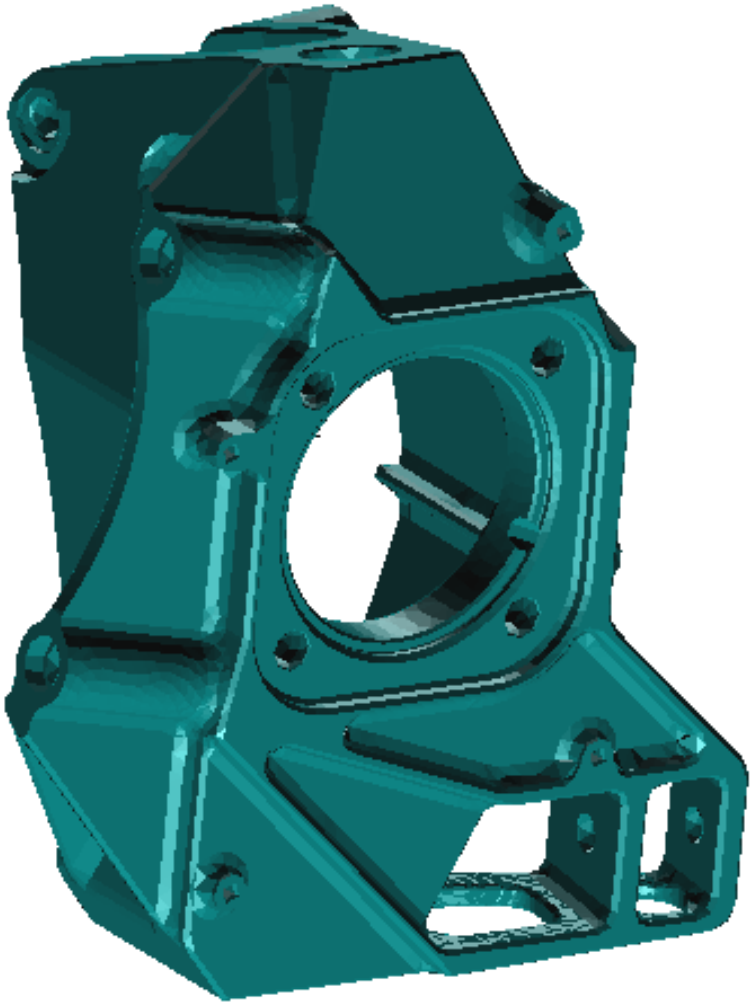

Figure 4-35 - Back view of the optimized wheel carrier

The figures presented above illustrate the areas where material is removed. The optimization performed on the wheel carrier reshaped structural elements in some areas and created holes in the structure in other areas. Reshaped areas correspond to locations that do not accommodate significant stresses, but play relevant roles in the wheel carrier's function. One such zone is the area of application of the braking moment.

Conversely, the holes created in the optimized structure are areas that, according to the primary optimization output, have a significant number of elements with low relative densities and are not essential for the functioning of the part. They were removed due to the fact that their relative density is inferior to the defined threshold value.

The definition of the optimized structure is therefore a procedure that depends not only on the optimization output of the software but also on the integration of the structure in the vehicle body, connection areas and manufacturing constraints. For instance, in the area 1 identified in Figure 4-36, a significant number of elements with low relative density are located in the lower stiffener face and in the vertical rib with mounting hole face, as shown in Figures 4-29 to 4-31, and hence with optimization potential. However, it must be taken into account that this zone corresponds to a connection area, and thus the complete elimination of the low density elements would compromise its function. Instead of removing this area altogether, the solution found consisted of creating a hole in the lower surface, maintaining the elements located in the vertical rib. Conversely, the area 2, identified in Figure 4-36, is not relevant for the connection of the carrier to the rest of the vehicle and the respective removal does not hinder the manufacturing process. As a result, rib area 2 can be fully removed.

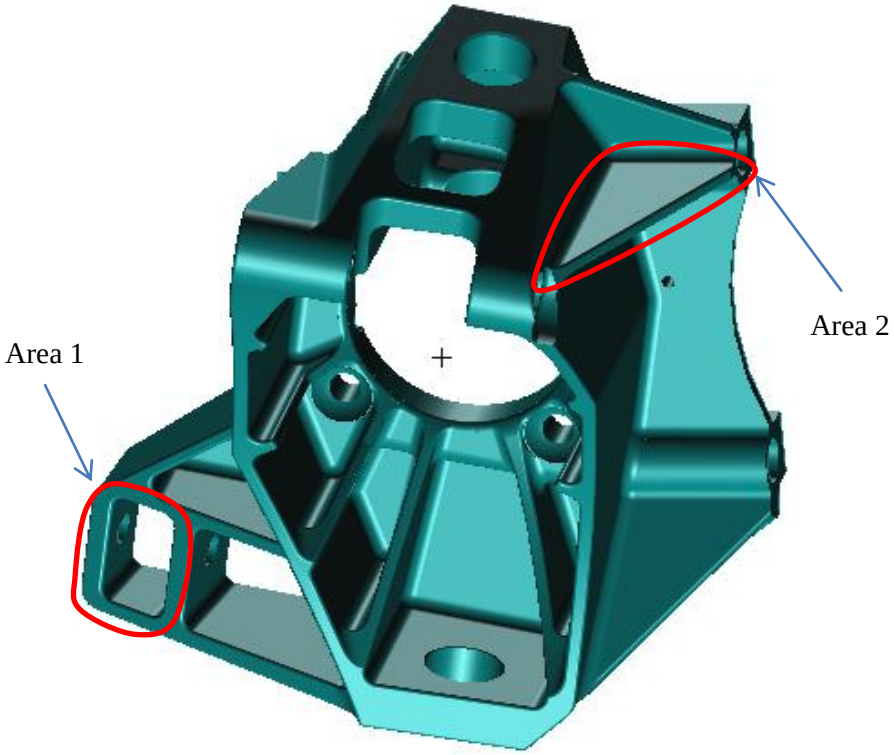

Figure 4-36 – Areas requiring different optimization approaches

For reader's convenience, the optimization procedure is outlined in Figures 4-37 and 4-38. The primary output of the program identifies areas of low relative densities, meaning that they are structurally dispensable. Based on this output, the engineer interprets the results and decides which of these parts can actually be removed, taking into account the functionality of the part. Finally, this leads to the formulation of the optimized structure, where feedback from the producer regarding feasible shapes and dimensions must also be considered.

Primary optimization output

Identification of the areas for optimization in the non-optimized structure

Optimized structure

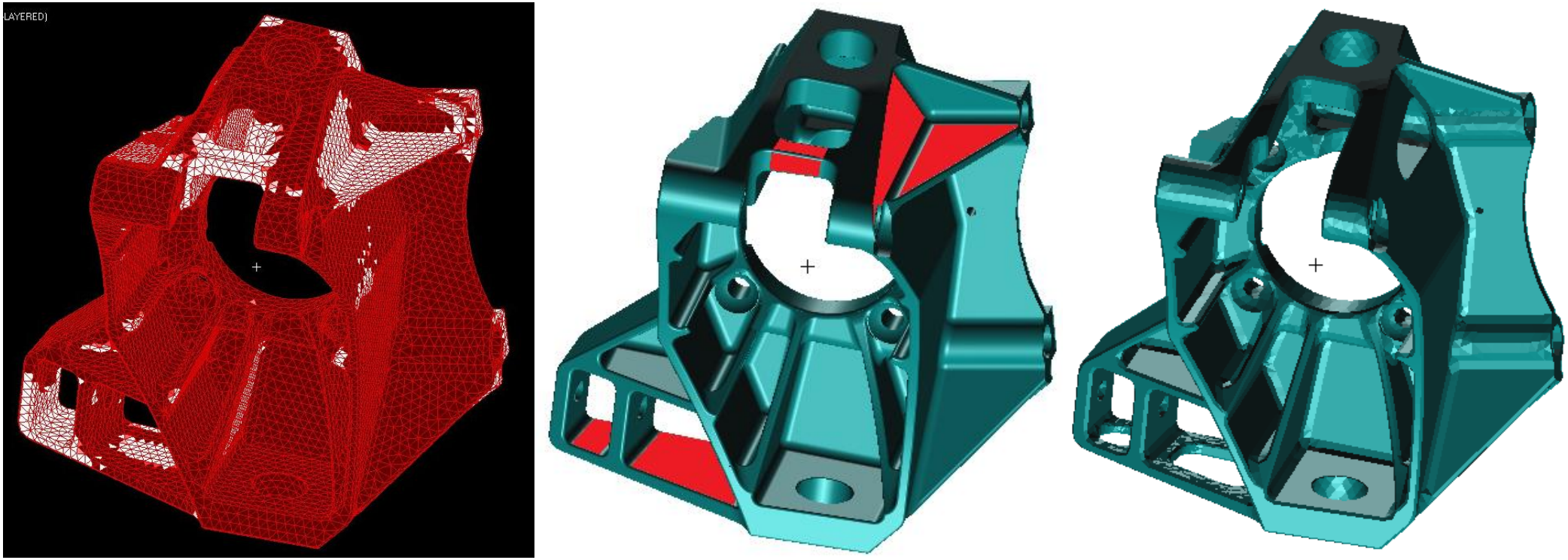

Figure 4-37 – Phases of the creation of the optimized structure (left side view)

Primary optimization output

Identification of the areas for optimization in the non-optimized structure

Optimized structure

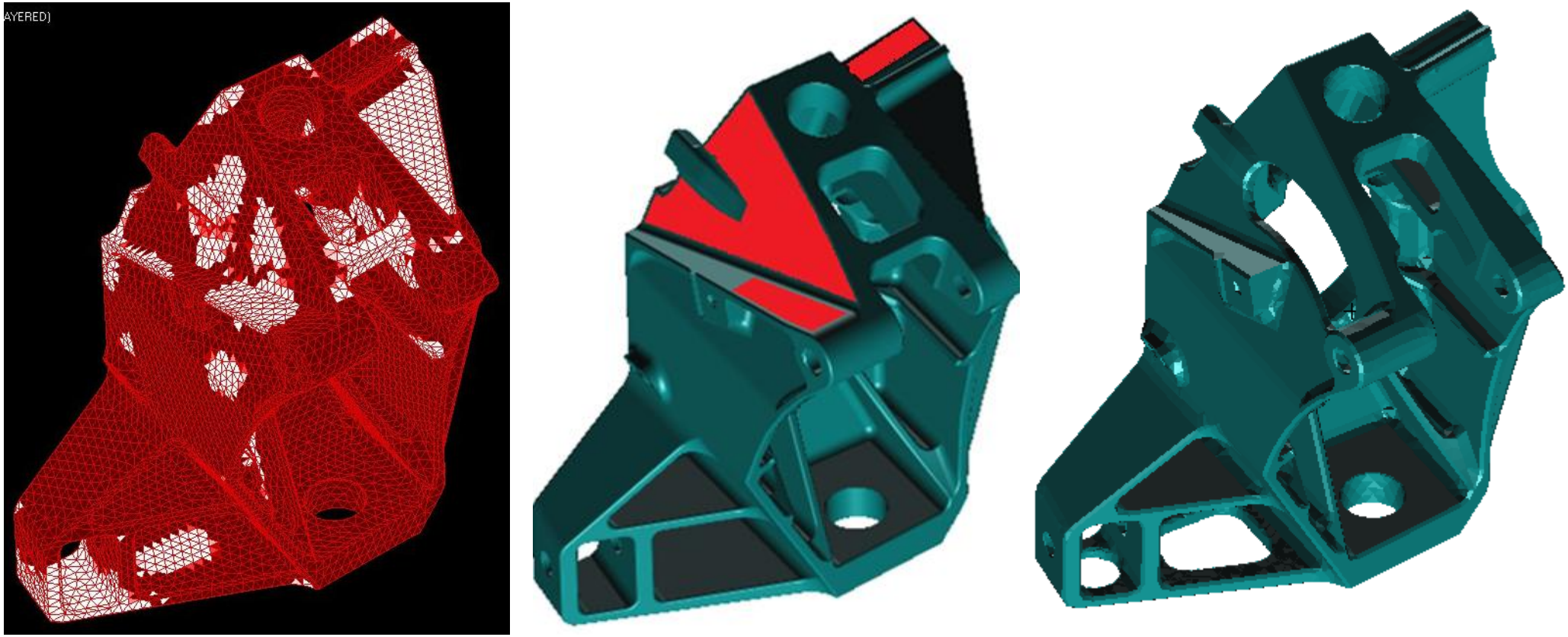

Figure 4-38 – Phases of creation of the optimized structure (right side view)

4.7 Analysis of the optimized structure

When the optimization procedure is finished, there are several evaluations that should be performed in order to create a comparison basis between the initial (non-optimized) and the optimized structures. One immediate procedure is based on the stiffness comparison between both structures. The first step involves the creation of different load cases for each direction and each load application point. Each of these load cases is purposely created for the stiffness analysis and consists of the application of a single load of 10kN in one of the three axial directions. A load case consisting of the application of a 1kNm Bremsen moment in the same point as for the optimization analysis is also created for the stiffness analysis. The load cases thus created are presented in Table 18 with the respective load application points, as identified in Figure 4-6. This procedure is performed with the same loads for the non-optimized and for the optimized structures, thus enabling the direct stiffness comparison between both. The relative structural stiffness is assessed by comparing the displacement vectors at each load application point, in each direction separately, for all load cases. These results are presented in Appendix A, for the non-optimized structure, and in Appendix B, for the optimized structure.

Load Case	Load introduction point	Force [kN]			Moment [Nm]
		Fx	Fy	Fz	Mz
1	A	10	-	-	-
2	A	-	10	-	-
3	A	-	-	10	-
4	B	10	-	-	-
5	B	-	10	-	-
6	B	-	-	10	-
7	C	10	-	-	-
8	C	-	10	-	-
9	C	-	-	10	-
10	D	10	-	-	-
11	D	-	10	-	-
12	D	-	-	10	-
13	E	-	-	-	1000

Table 18 - Load cases created for the stiffness comparison between the optimized and non-optimized structures

From the interpretation of all displacement vectors, it was concluded that the most relevant losses of structural stiffness correspond to the following situations:

- Displacement at point C in X direction when the load is applied on point C in X direction, corresponding to the load case 7;
- Displacement at point C in Y direction when the load is applied on point C in Y direction, corresponding to the load case 8;
- Displacement at point A in Y direction when the load is applied on point A in Y direction, corresponding to load case 2;
- Displacement at point D in Z direction when the load is applied on point D in Z direction, corresponding to load case 12.

For these situations, the displacement values obtained with both optimized and non-optimized structures are presented in Table 19 along with the absolute difference and the relative increase caused by the elimination of material.

Load application point	Displacements [mm]			Difference [mm]	Percentage of increase [%]
	Direction	Structure			
		Non-optimized	Optimized		
D (load in Z direction)	Z	0,3892756	0,4732922	0,08401654	21,5827912
C (load in X direction)	X	0,1765208	0,2193769	0,0428561	24,2782154
C (load in Y direction)	Y	0,2987261	0,5295258	0,2307989	77,2610428
A (load in Y direction)	Y	0,08392702	0,1245926	0,04066558	48,4535016

Table 19 - Comparison between displacement values of the optimized and non-optimized structures for four load application points

From the structural designer's point of view, the stiffness reduction of the structure is only important if the resulting increase of displacements may compromise the structural safety. This may occur if the boundary conditions, that is, the connection of the carrier to the neighboring structural parts, enforce strict restrictions on the allowable structural displacements. In this case, it was concluded that even with the significant decrease of the structural stiffness in the directions given in Table 19, the expectable displacements under operational conditions are not prone to jeopardize the structural safety. Consequently, the control of the optimization process should be based on the monitoring of the load path in the structure, which essentially means that the stress field is the most important output parameter to control for the validation of the optimized wheel carrier. Despite this, the displacements in the optimized structure under real loading conditions will still be calculated, to endorse a full comparison between the non-optimized and optimized structures.

For the strength analysis of the optimized structure, a linear static analysis was performed in order to compare the results with the already analyzed non-optimized structure.

This analysis was performed using the same load cases and boundary conditions as for the non-optimized structure. For the Ratterkerb3 load case, the Von Misses stress field obtained for the optimized structure is presented in Figure 4-39, along with the same output for the non-optimized structure. For comparison, the displacements obtained for the same situation are shown in Figure 4-40. It is concluded that for this load case, the area with the highest stress value is the same as for the non-optimized structure. Moreover, for the optimized structure the maximum stress is 127,25 MPa, which is very close to the maximum stress of 131,28 MPa obtained for the non-optimized structure. It is also possible to verify that the stress distribution on the area surrounding the holes that arise from the optimization of the left bottom section reveals higher stresses than those occurred in the same area for the non-optimized structure (80 MPa versus 30 MPa). Although this increase is significant, the structural safety is clearly far from being compromised. Therefore, the removal of material in that area is totally acceptable. As for the analysis of the non-optimized structure, it should be noted that the stress peaks occurring at the load application and constraint points are neglected. The analysis of the displacement output of the optimized structure reveals a maximum resultant displacement of 0,576mm. For the non-optimized structure, the maximum resultant displacement occurred in the same area and amounted to 0,495 mm. The higher displacements in the optimized structure in comparison with the non-optimized structure can be explained by the decrease in the structural stiffness. The increase in displacements does not, however, compromise the structural safety, as the maximum displacement value on the optimized structure is still far from the maximum allowable value of 1.0 mm.

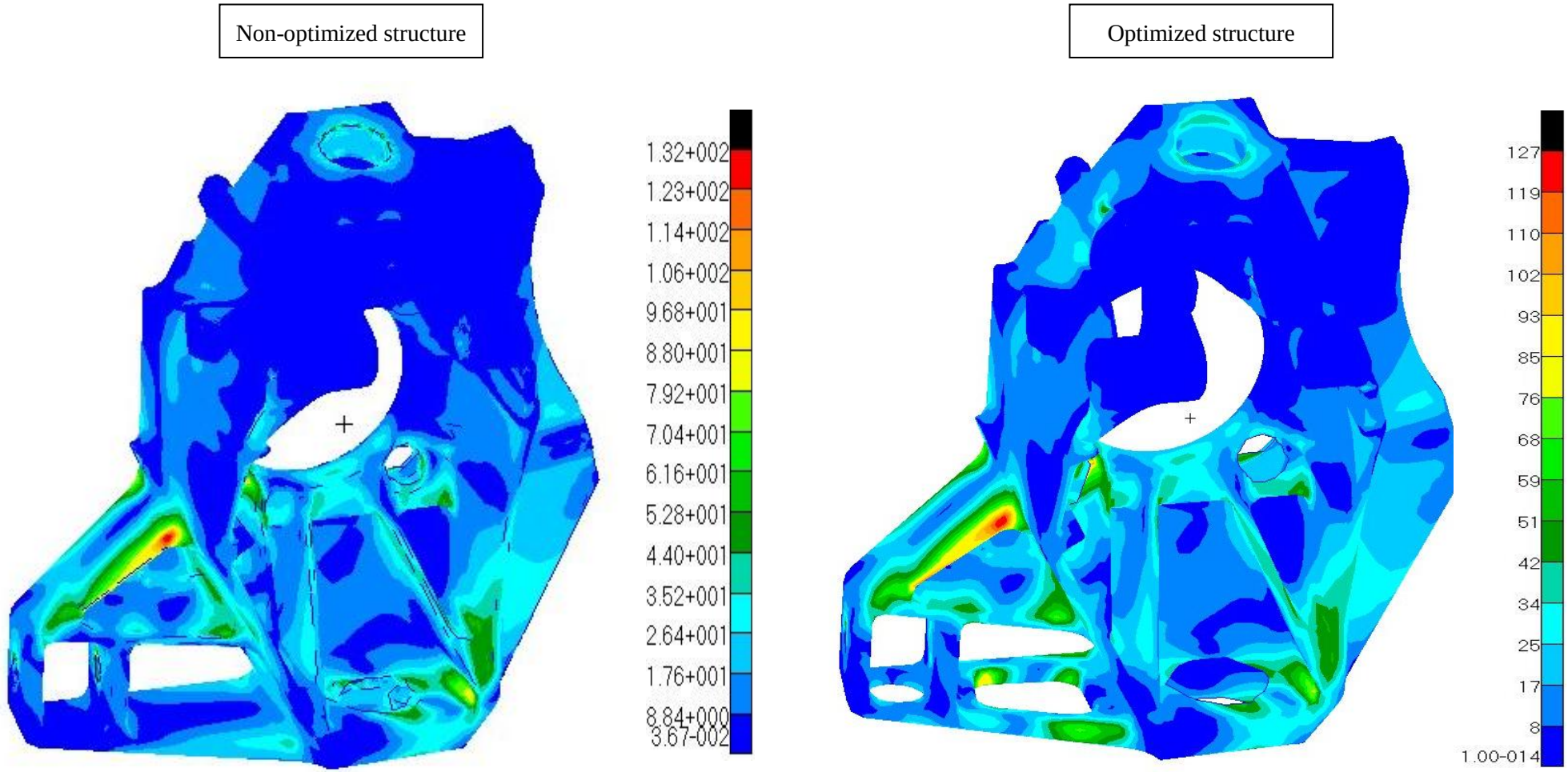

Figure 4-39 - Stress output of the non-optimized and optimized structures for the Ratterkerb3 load case

Non-optimized structure

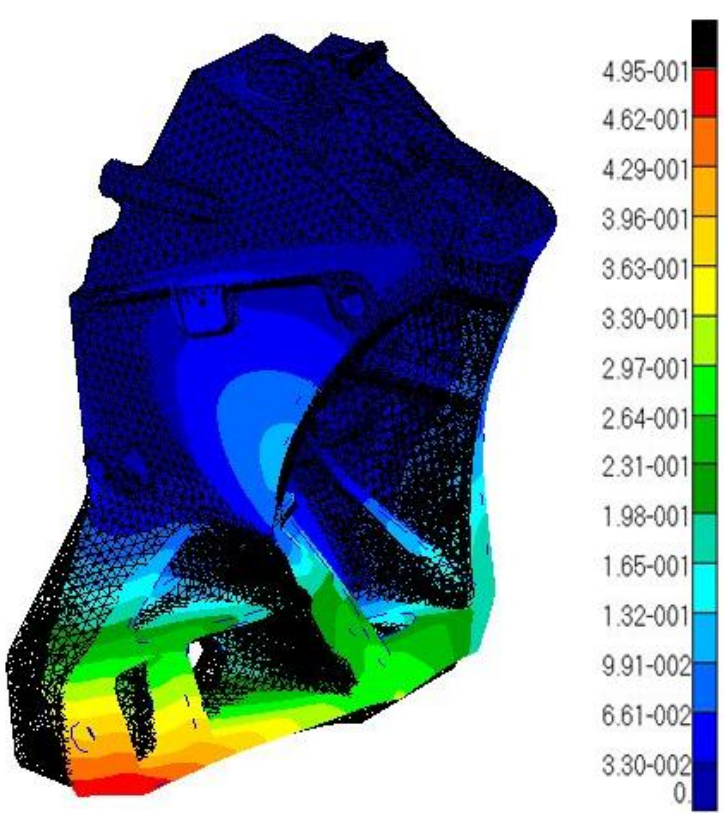

Optimized structure

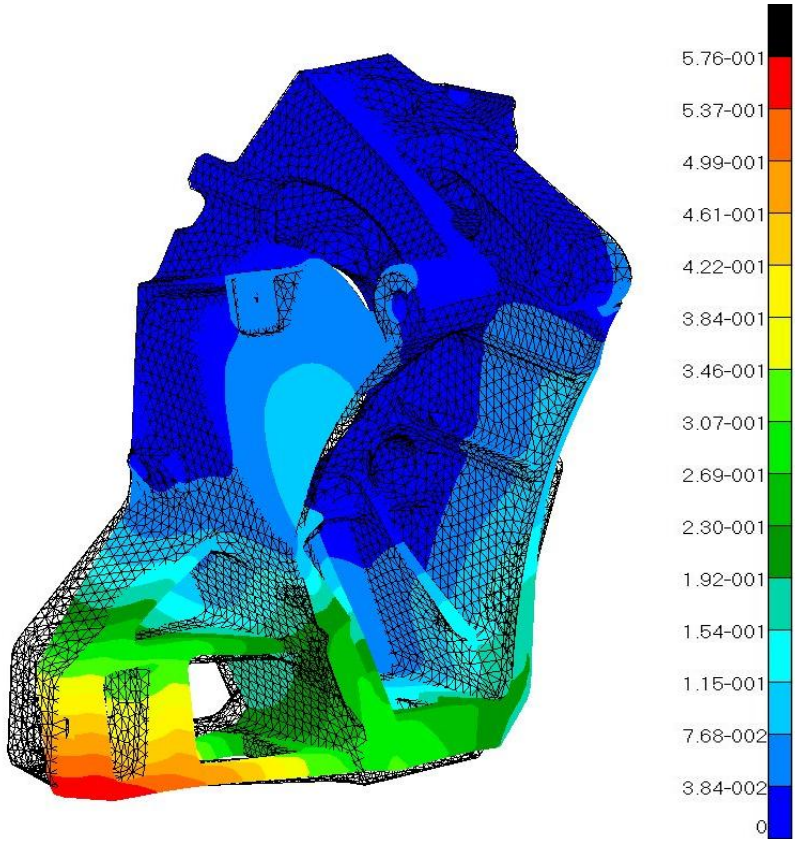

Figure 4-40 - Displacement output of the non-optimized and optimized structures for the Ratterkerb3 load case

For the Ludwigskerb load case, the stress fields obtained from the analysis of the optimized and non-optimized structures are plotted in Figure 4-41. As expected, and due to the removal of material, the stresses in the optimized structure are generally higher. As for the Ratterkerb3 load case, the area surrounding the holes created through the optimization presents higher stresses than the same area of the non-optimized structure. In this area, the stresses increase from roughly 25 MPa on the non-optimized structure to roughly 50 MPa on the optimized structure. Such increase reflects a better use of the strength of the material and poses no structural threat since it is still far from the limit strength of the alloy, 440 MPa. The maximum stresses obtained for this load case are 184,09 MPa on the optimized structure and 165,78 MPa on the non-optimized structure. Both stresses occur at the same area, namely the rib in the bottom left section of the structure. The Von Misses stress difference obtained for this load case is significant, resulting in an increase of about 11%, and subjecting the optimized structure to higher stresses during its lifetime, which may create, on a long term basis, fatigue phenomena. The evaluation of the displacement field, presented in Figure 4-42 along with the displacement output of the non-optimized structure, reveals a maximum resultant displacement of 0,645 mm, a higher value than for the non-optimized structure analysis, 0,58 mm. The higher displacements obtained for the optimized structure comparing to the non-optimized structure are caused by the removal of material and the resulting decrease in the structural stiffness. Even though there is an increase, the value of displacement on the optimized carrier does not reach the maximum allowable value of 1.0 mm and hence does not compromise the structural safety.

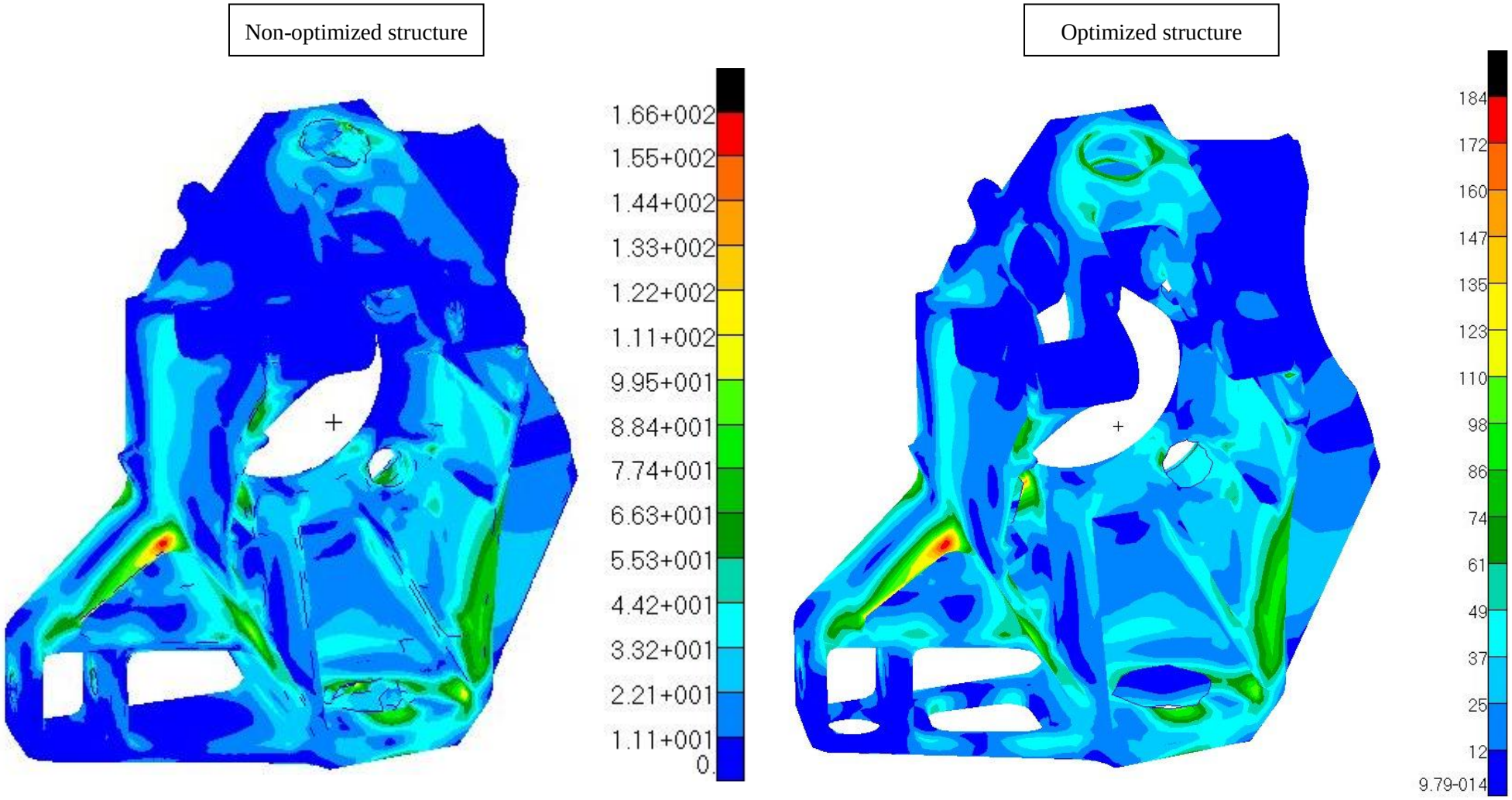

Figure 4-41 - Stress output of the non-optimized and optimized structures for the Ludwigskerb load case

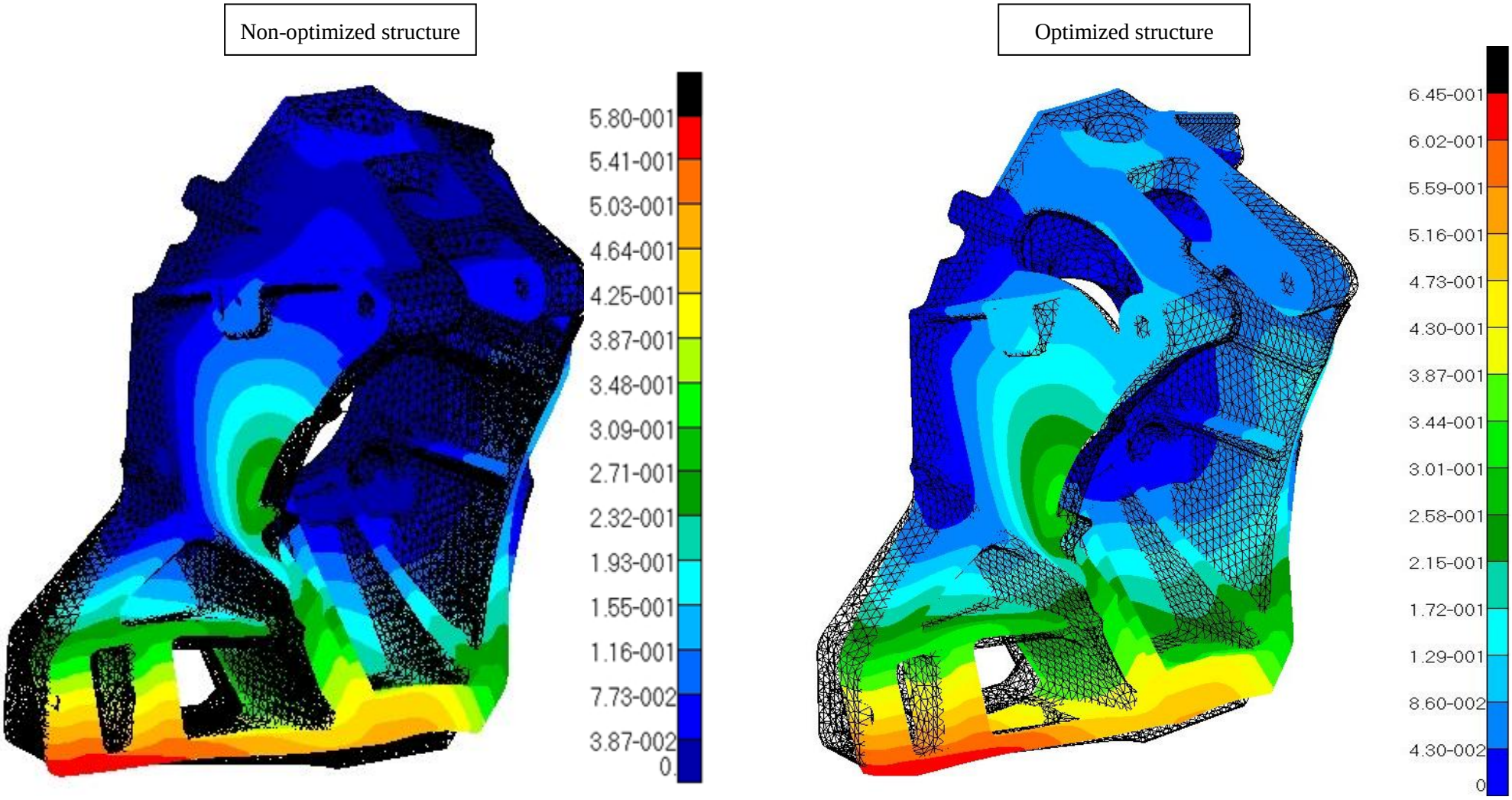

Figure 4-42 - Displacement output of the non-optimized and optimized structures for the Ludwigskerb load case

The evaluation of the stresses caused by the application of the Bremsen load case to the optimized structure, presented in Figure 4-43 along with the stress output of the non-optimized structure, also shows a relative stress increase. While for the non-optimized wheel carrier the maximum stress is 73,79 MPa, the application of the same load case on the optimized structure increases the stress value in the same area to 101,76 MPa. It should be noted that the maximum stress obtained in the analysis of the optimized structure occurs in an area directly influenced by the optimization. This area was quadrangular shaped on the non-optimized structure, and became cylindrical in the optimized structure, as illustrated in Figures 4-44 and 4-45.

The section was divided by the optimization in two parts. The part that contains the opening is included in the optimization process and transformed from parallelipipedic to cylindrical. However, the remaining part of the area remains unchanged. Thus, in the optimized wheel carrier, a connection area is created between the two parts and it is in this connection area that the largest stresses arise. In this area, the stress on the optimized structure reaches a value of around 100 MPa (Figure 4-46), which poses no structural threat to the structure as it is far from the limit strength of the alloy, 440 MPa. It is noted that the raise in stresses would have been even sharper should the connection area not been rounded, as known from the classical theory of elasticity. The evaluation of the displacement field, presented in Figure 4-47 along with the displacement output for the non-optimized structure, shows higher displacement values in the optimized structure as compared to the non-optimized structure. The maximum resultant occurs in the upper area of application of the Bremsen moment, and amounts to 0,117 mm for the optimized structure and to 0,0788 mm, for the non-optimized structure. The increase in the displacement does not hinder the structural safety of the wheel carrier, however, as the displacement value on the optimized structure is far from the maximum allowable value of 1.0 mm.

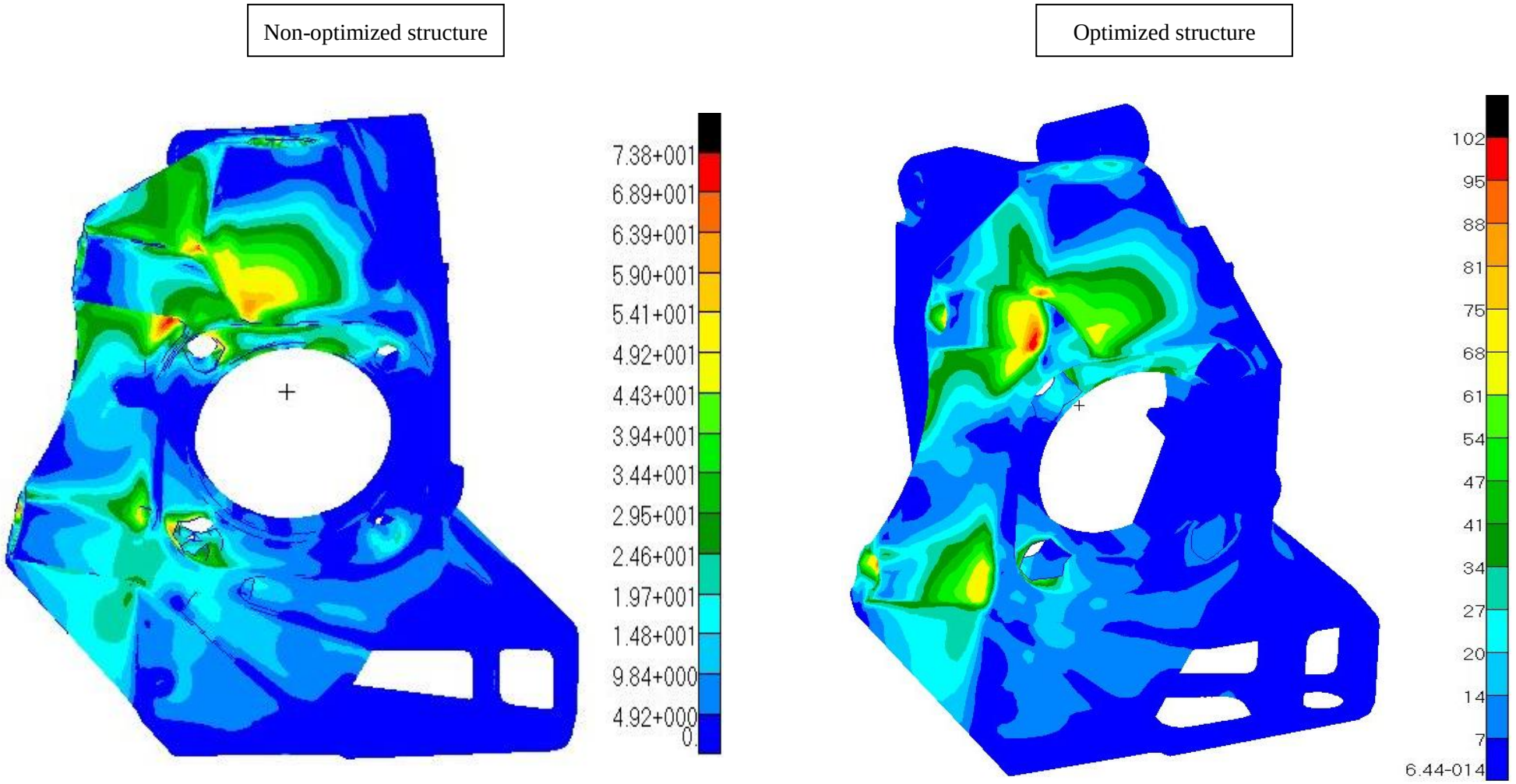

Figure 4-43 - Stress output of the non-optimized and optimized structures for the Bremsen load case

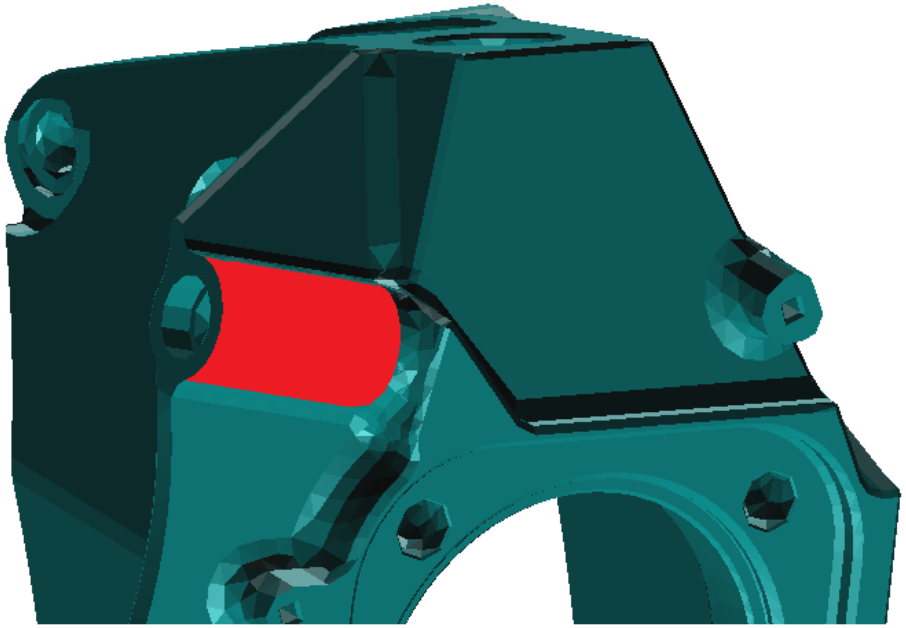

Figure 4-44 - Maximum stress area for the Bremsen load case - optimized structure

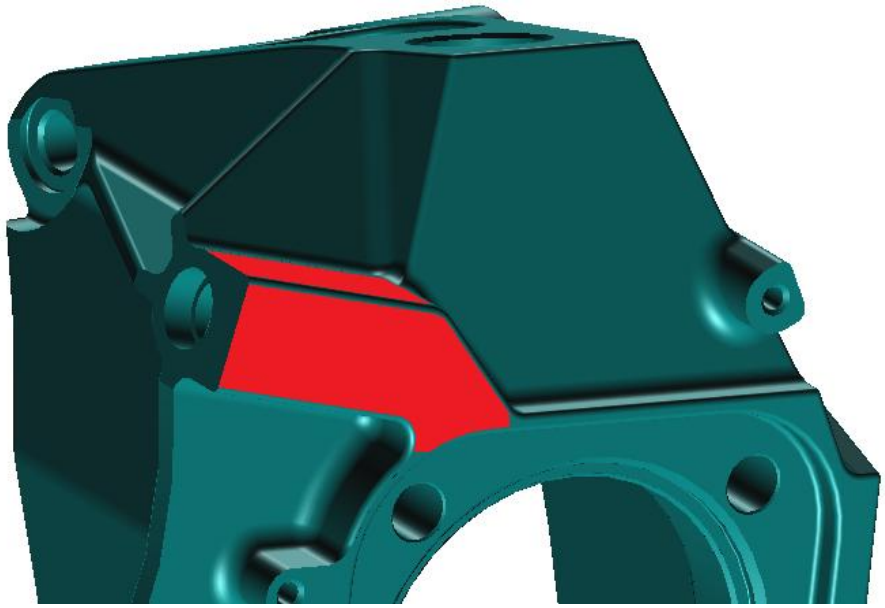

Figure 4-45 - Maximum stress area for the Bremsen load case – non-optimized structure

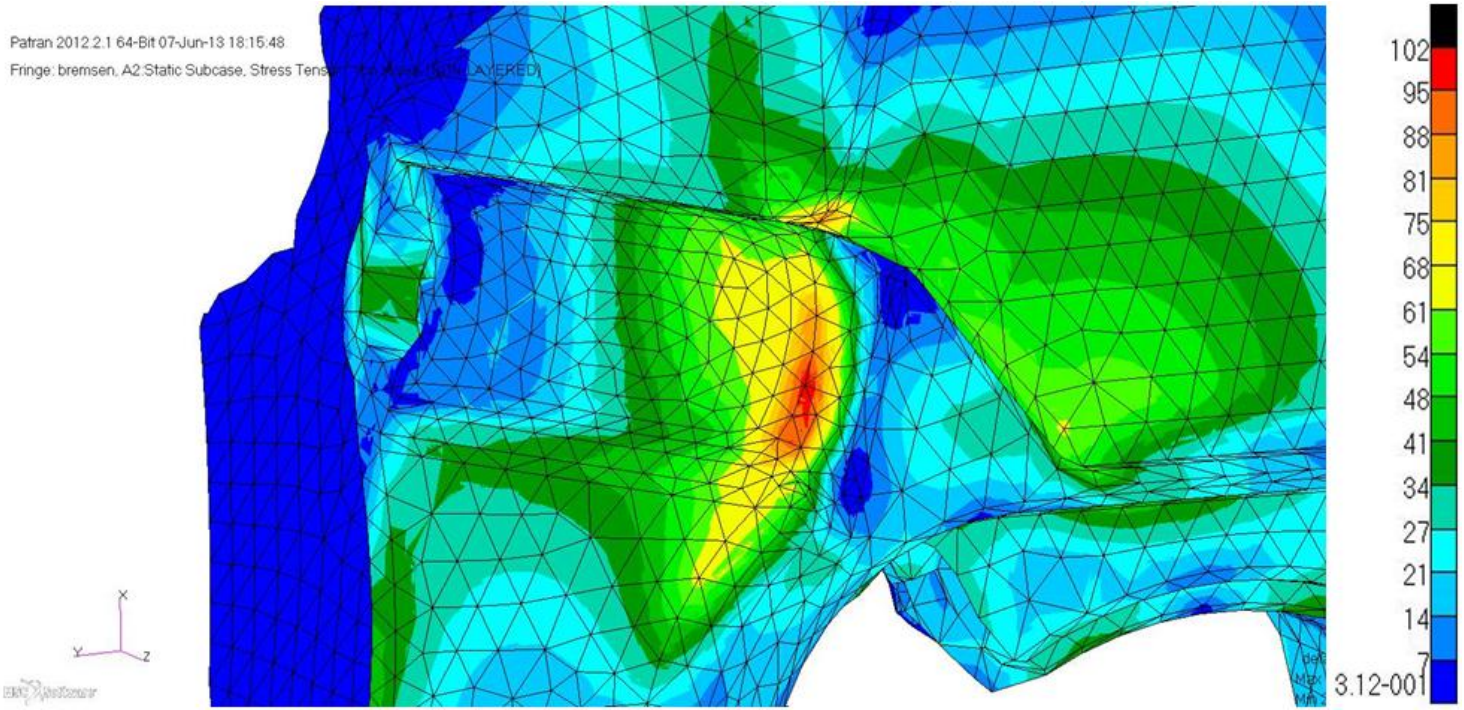

Figure 4-46 - Maximum stress area in the optimized structure for the Bremsen load case

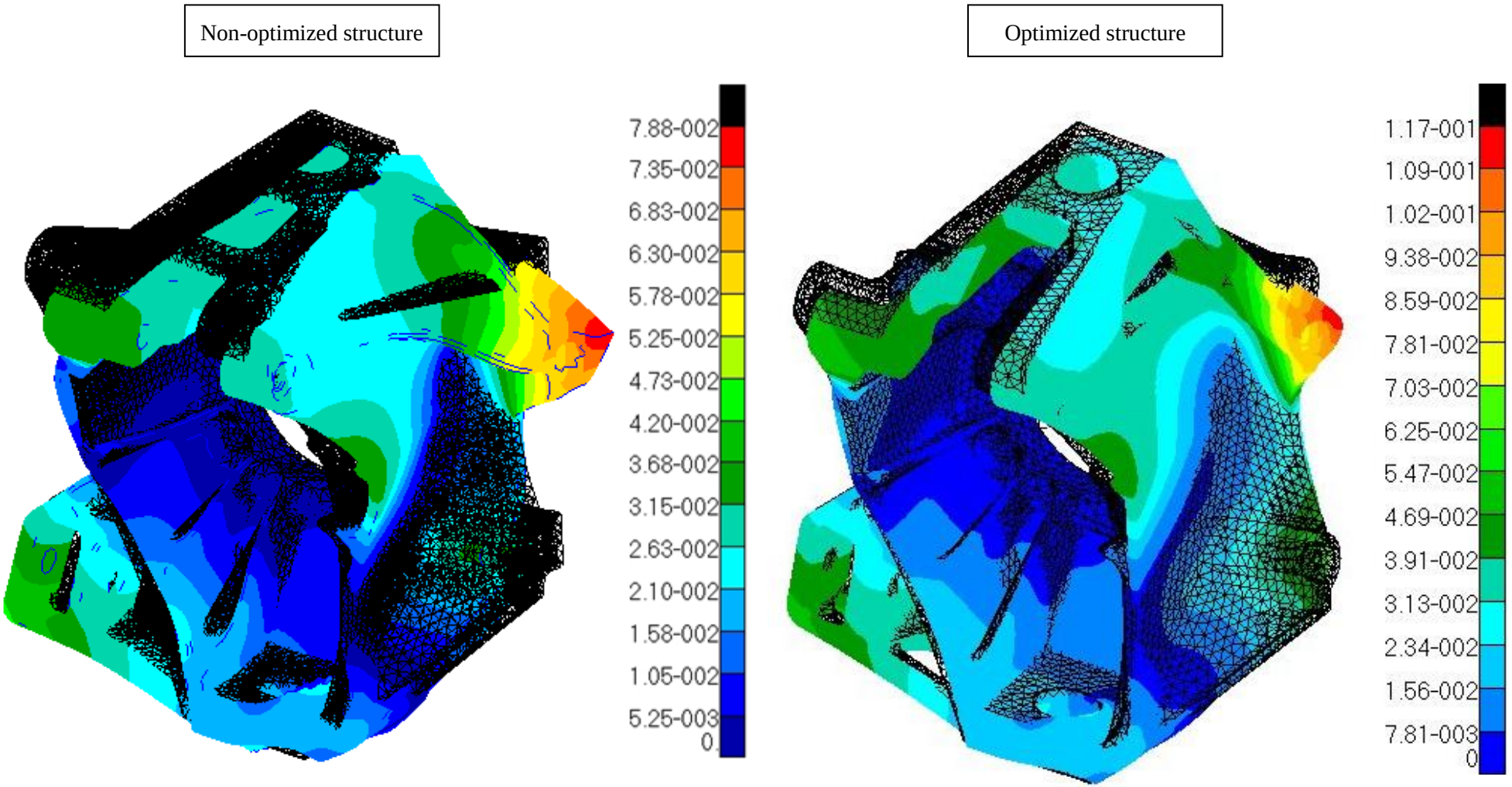

Figure 4-47 - Displacement output of the non-optimized and optimized structures for the Bremsen load case

5. CONCLUSIONS

Several approaches can be used to derive the finite element formulation. One of the most general strategies is to use the weak-form of the problem. A more physically-meaningful strategy arises from the application of the virtual work principle, which is more appealing to structural engineers than a purely mathematical approach. Alternatively, one can recover the finite element formulation by using the variational principle form of the problem, which is a more general, yet physics-based approach.

The study of the convergence of the solutions obtained using the FEM is of outmost importance, as it enables the evaluation of their quality and offers a sense of the error reduction when the finite element mesh is refined. The convergence process under mesh refinement is illustrated here using two numerical examples, namely the eigenmode analysis of a rectangular plate and the stress analysis in a tension coupon with a hole. The finite element results are compared with available analytic results and are found to converge to the exact solution as the dimensions of the finite elements are reduced.

One of the most important applications of the FEM is as part of a structural optimization process. Optimization is an essential part of the development of a product and consists of finding the shape, size and/or topology of a structural part such to maximize (or minimize) an objective function (e.g. material consumption) while still respecting a number of (typically safety-related) restrictions. A significant number of numerical methods for finding extrema of one- and multi-dimensional functions is briefly discussed in this work. One-dimensional minimization methods may or may not use derivative information of the objective function. When they do, superior convergence may be achieved, provided that the information is handled with some caution, as it may otherwise cause numerical instability. The additional convergence, however, comes at the cost of additional function evaluations, required for computing the derivatives.

Except for the Simplex Method, all multi-dimensional methods are based on successive one-dimensional minimizations. Here too, the method may or may not use function gradient information. When such information is available, conjugate gradient methods are typically preferred over Powell's and Steepest Gradient methods, which only use direct function evaluations. When the minimization problem is constrained, the minimum may lay not only inside the feasible domain, but also on its boundary. If the problem is linear, the Linear Programming Method is designed to look for extrema on the boundaries only. However, more

complex problems may require a combination of algorithms to be successfully handled. Two examples of (size and topology) structural optimization are presented to illustrate the application of the principles.

The application of the FEM for the optimization of complex structures is illustrated through the topology optimization performed on a wheel carrier of a motorsports car. From this procedure, a significant weight reduction is accomplished, as approximately 12% of the initial mass is removed. This relevant mass reduction is possible through the application of the minimization methods used by the finite element platform MSC.-NASTRAN and provides a significant reduction on the production costs taking into account the large scale production of the part. Although the optimization process involves the increase in stresses and displacements occurring in the wheel carrier for all load cases, it is concluded that the values obtained for the optimized structure are acceptable, as the allowable limits are not reached.

The weight saved through the topology optimization performed in the wheel carrier represents a good result, taking into account the complexity of the wheel carrier model and the equally complex design constraints. Nevertheless, there is potential to save even more weight through a topology optimization performed in a previous design step, when the geometry of the part is not yet defined. There is also potential to reduce the stresses occurred in the structure by performing a shape optimization process in the areas with highest stresses. It is concluded that, despite the potential to save more weight and to reduce stresses, the weight saved through the topology optimization performed in this work is a practically relevant result.

REFERENCES

Argyris, J.; Kelsey, S. (1960). *Energy theorems and structural analysis***.** Butterworths, London.

Chapra, S. & Canale, R. (2006). *Numerical methods for engineers* (5th edition). McGraw-Hill.

Chong, E. & Zak, S. (2001). *An Introduction to Optimization* (2nd edition). USA: John Wiley & Sons, Inc.

Clough, R. (1960). The Finite Element Method in Plane Stress Analysis. *Proceedings, American Society of Civil Engineers, 2nd Conference on Electronic Computation*, Pittsburgh, PA, pp 345-378.

Courant, R. (1943). *Variational methods for the solution of problems of equilibrium and vibrations*. Bulletin of American Mathematical Society.

Feldmann, M.; Heinemeyer, C.; Butz, C.; Cateano, E.; Cunha, A,; Galanti, F.; Goldack, A.; Hechler, O.; Hicks, S.; Keil, A.; Lukic, M.; Obiala, R.; Schlaich, M.; Sedlacek, G.; Smith, A.; Waarts, P. (2009). Design of floor structures for human induced vibrations. Report prepared for the Joint Research Centre Scientific and Technical Reports.

Gupta, K. & Meek, J. (1996). A brief history of the beginning of the Finite Element Method. *International Journal for Numerical Methods in Engineering* **39**: 3761-3774.

Kim, H.; Kim, B; Suh, M. (2011). Development of a Topology Optimization Program Considering Density and Homogenization Methods. *International Journal of Precision Engineering and Manufacturing* **12**(2): 303-312.

Pilkey, D & Pilkey, W. (2008). *Peterson's stress concentration factors*. Hoboken, New Jersey: John Wiley & Sons, Inc. pp 209-433.

Press, W; Teukolsky, S; Vetterling, W; Flannery, B. (1992). *Numerical Recipes in C: The Art of Scientific Computing* (2nd edition). Cambridge: Cambridge University Press.

Ritz, W. (1909). Über eine neue Methode zur Lösung gewisser Variationsprobleme der mathematischen Physik. *Jornal für die Reine und Angewandte Mathematik* **135**: 1-61.

Turner, M.; Clough, R.; Martin, H.; Topp, L. (1956). Stiffness and deflection analysis of complex structures. *Journal of Aeronautical Sciences* **25**: 805-823.

Zhang, W.; Wang, D.; Jiang, S. (2002). Truss shape optimization with multiple displacement constraints. *Computer Methods in Applied Mechanics and Engineering* **191:** 3597-3612.

Zienckiewicz, O. & Cheung, Y. (1965). *The Finite Element Method in Continuum and Structural Mechanics*. New York: McGraw-Hill.

Zienckiewicz, O.; Taylor, R.; Zhu, J. (2005). *The Finite Element Method: Its Basis and Fundamentals* (6th edition). Oxford: Elsevier.

APPENDIX A – Stiffness analysis displacements of the non-optimized structure

Non-optimized structure						
Load Case	Load introduction point	Load introduction direction	Displacements [mm]			
			Nodes	Direction		
				X	Y	Z
1	A	X	A	0,04474485	0,002262289	0,06368608
			B	0,002704693	0,0006654959	-0,01253124
			C	0,05561326	0,003650708	0,01590897
			D	0,001331304	0,0001729798	-0,01124497
			E	0,001959119	-0,0006011655	0,002416110

Non-optimized structure						
Load Case	Load introduction point	Load introduction direction	Displacements [mm]			
			Nodes	Direction		
				X	Y	Z
2	A	Y	A	0,002262289	0,08392702	0,0002466485
			B	-0,001778913	-0,001413462	0,004376644
			C	0,0003963232	0,04811292	-0,0006892935
			D	0,002407301	-0,002020089	-0,004525267
			E	-0,007793745	0,006616581	0,01584228

Non-optimized structure						
Load Case	Load introduction point	Load introduction direction	Displacements [mm]			
			Nodes	Direction		
				X	Y	Z
3	A	Z	A	0,06368608	0,0002466485	0,1789983
			B	0,005607006	0,0005572410	-0,02770961
			C	0,1250527	0,009586545	0,04212325
			D	0,002604231	0,00001736772	-0,02353440
			E	0,001092952	0,0006356711	0,01162288

Non-optimized structure						
Load Case	Load introduction point	Load introduction direction	Displacements [mm]			
			Nodes	Direction		
				X	Y	Z
4	B	X	A	0,002704693	-0,001778913	0,005607006
			B	0,05970414	0,01665998	-0,08391888
			C	0,005002447	-0,001810350	0,003131365
			D	-0,0006685440	0,008231516	-0,03984150
			E	0,006148540	0,0003384195	0,01360194

Non-optimized structure						
Load Case	Load introduction point	Load introduction direction	Displacements [mm]			
			Nodes	Direction		
				X	Y	Z
5	B	Y	A	0,0006654959	-0,001413462	0,0005572410
			B	0,01665998	0,1250068	-0,001538795
			C	0,001397472	0,002388177	0,000008264400
			D	-0,02385035	0,03631077	-0,04791001
			E	0,01340592	0,001544890	0,02533607

Non-optimized structure						
Load Case	Load introduction point	Load introduction direction	Displacements [mm]			
			Nodes	Direction		
				X	Y	Z
6	B	Z	A	-0,01253124	0,004376644	-0,02770961
			B	-0,08391888	-0,001538795	0,3849173
			C	-0,02779293	0,002872744	-0,01273958
			D	-0,003214071	-0,007437412	0,1267128
			E	-0,003163542	0,001220750	-0,006318122

Non-optimized structure						
Load Case	Load introduction point	Load introduction direction	Displacements [mm]			
			Nodes	Direction		
				X	Y	Z
7	C	X	A	0,05561326	0,0003963232	0,1250527
			B	0,005002447	0,001397472	-0,02779293
			C	0,1765208	0,008656571	0,03861320
			D	0,003558810	0,00006946215	-0,03168115
			E	0,002476992	0,00001992598	0,006278813

Non-optimized structure						
Load Case	Load introduction point	Load introduction direction	Displacements [mm]			
			Nodes	Direction		
				X	Y	Z
8	C	Y	A	0,003650708	0,04811292	0,009586545
			B	-0,001810350	0,002388177	0,002872744
			C	0,008656571	0,2987261	-0,007648167
			D	-0,001495204	0,001280083	0,02606746
			E	-0,002460695	0,006348746	0,06111619

Non-optimized structure						
Load Case	Load introduction point	Load introduction direction	Displacements [mm]			
			Nodes	Direction		
				X	Y	Z
9	C	Z	A	0,01590897	-0,0006892935	0,04212325
			B	0,003131365	0,000008264400	-0,01273958
			C	0,03861320	-0,007648167	0,02627679
			D	0,0009089504	-0,00009346133	-0,009446342
			E	0,0006019942	0,0001368038	0,007537953

Non-optimized structure						
Load Case	Load introduction point	Load introduction direction	Displacements [mm]			
			Nodes	Direction		
				X	Y	Z
10	D	X	A	0,001331304	0,002407301	0,002604231
			B	-0,0006685440	-0,02385035	-0,003214071
			C	0,003558810	-0,001495204	0,0009089504
			D	0,07950886	-0,03537401	-0,001908095
			E	-0,004785024	-0,0002842311	-0,002785791

Non-optimized structure						
Load Case	Load introduction point	Load introduction direction	Displacements [mm]			
			Nodes	Direction		
				X	Y	Z
11	D	Y	A	0,0001729798	-0,002020089	0,00001736772
			B	0,008231516	0,03631077	-0,007437412
			C	0,00006946215	0,001280083	-0,00009346133
			D	-0,03537401	0,07207213	-0,009002943
			E	0,007688927	0,0007556975	0,007450387

Non-optimized structure						
Load Case	Load introduction point	Load introduction direction	Displacements [mm]			
			Nodes	Direction		
				X	Y	Z
12	D	Z	A	-0,01124497	-0,004525267	-0,02353440
			B	-0,03984150	-0,04791001	0,1267128
			C	-0,03168115	0,02606746	-0,009446342
			D	-0,001908095	-0,009002943	0,3892756
			E	-0,005496432	-0,001694586	-0,03369879

Non-optimized structure						
Load Case	**Load introduction point**	**Load introduction direction**	**Displacements [mm]**			
			Nodes	**Direction**		
				X	**Y**	**Z**
13	**E**	**Z**	**A**	-0,000260834	0,008050459	0,001445677
			B	-0,004286827	-0,009958274	0,001049691
			C	0,001100126	0,008220507	0,0003589695
			D	0,003699251	-0,005777852	0,004317655
			E	-0,008847014	0,004053092	-0,005312168

APPENDIX B – Stiffness analysis displacements of the optimized structure

Optimized structure						
Load Case	Load introduction point	Load introduction direction	Displacements [mm]			
			Nodes	Direction		
				X	Y	Z
1	A	X	A	0,08120006	0,01165055	0,1093138
			B	0,003203155	-0,0001066624	-0,01639616
			C	0,08158498	-0,007882500	0,03197210
			D	0,001386643	-0,0001166946	-0,01176505
			E	0,002125891	-0,0004857813	0,001031846

Optimized structure						
Load Case	Load introduction point	Load introduction direction	Displacements [mm]			
			Nodes	Direction		
				X	Y	Z
2	A	Y	A	0,01165055	0,1245926	0,01119095
			B	-0,001457435	-0,002123364	0,002172068
			C	0,006111366	0,06145977	0,002762202
			D	0,002630587	-0,002436352	-0,003059773
			E	-0,01007690	0,008877069	0,03063130

Optimized structure						
Load Case	Load introduction point	Load introduction direction	Displacements [mm]			
			Nodes	Direction		
				X	Y	Z
3	A	Z	A	0,1093138	0,01119095	0,2556297
			B	0,007063946	-0,001067558	-0,03710688
			C	0,1729738	-0,008524112	0,07648829
			D	0,002710798	-0,0006134486	-0,02529039
			E	0,0008020122	0,0009892338	0,01635179

Optimized structure						
Load Case	Load introduction point	Load introduction direction	Displacements [mm]			
			Nodes	Direction		
				X	Y	Z
4	B	X	A	0,003203155	-0,001457435	0,007063946
			B	0,06203280	0,01751880	-0,08956857
			C	0,005761008	-0,001577348	0,004365799
			D	-0,001034277	0,008777629	-0,03776719
			E	0,006683398	0,0001331683	0,01741680

Optimized structure						
Load Case	Load introduction point	Load introduction direction	Displacements [mm]			
			Nodes	Direction		
				X	Y	Z
5	B	Y	A	-0,0001066624	-0,002123364	-0,001067558
			B	0,01751880	0,1295385	-0,0006774836
			C	0,0005767106	0,002978673	-0,0008275252
			D	-0,02563696	0,03854417	-0,05341389
			E	0,01483369	0,001346525	0,03056118

Optimized structure						
Load Case	Load introduction point	Load introduction direction	Displacements [mm]			
			Nodes	Direction		
				X	Y	Z
6	B	Z	A	-0,01639616	0,002172068	-0,03710688
			B	-0,08956857	-0,0006774836	0,4093447
			C	-0,03465889	-0,0003093711	-0,01838395
			D	-0,0006551631	-0,01014285	0,1247795
			E	-0,003111650	0,001595861	-0,01056465

Optimized structure						
Load Case	Load introduction point	Load introduction direction	Displacements [mm]			
			Nodes	Direction		
				X	Y	Z
7	C	X	A	0,08158498	0,006111366	0,1729738
			B	0,005761008	0,0005767106	-0,03465889
			C	0,2193769	0,01011967	0,06215706
			D	0,004201553	-0,0008939689	-0,03837701
			E	0,002333717	0,0002987588	0,008661793

Optimized structure						
Load Case	Load introduction point	Load introduction direction	Displacements [mm]			
			Nodes	Direction		
				X	Y	Z
8	C	Y	A	-0,007882500	0,06145977	-0,008524112
			B	-0,001577348	0,002978673	-0,0003093711
			C	0,01011967	0,5295258	-0,02439121
			D	-0,001267475	0,0009976311	0,03356296
			E	-0,006600804	0,01011397	0,06489094

Optimized structure						
Load Case	Load introduction point	Load introduction direction	Displacements [mm]			
			Nodes	Direction		
				X	Y	Z
9	C	Z	A	0,03197210	0,002762202	0,07648829
			B	0,004365799	-0,0008275252	-0,01838395
			C	0,06215706	-0,02439121	0,04993176
			D	0,0008765329	-0,0002341414	-0,009230560
			E	0,0005459855	0,0002709294	0,01179437

Optimized structure						
Load Case	Load introduction point	Load introduction direction	Displacements [mm]			
			Nodes	Direction		
				X	Y	Z
10	D	X	A	0,001386643	0,002630587	0,002710798
			B	-0,001034277	-0,02563696	-0,0006551631
			C	0,004201553	-0,001267475	0,0008765329
			D	0,08861759	-0,04560834	-0,01118178
			E	-0,005301827	-0,0002835061	-0,003770420

Optimized structure						
Load Case	Load introduction point	Load introduction direction	Displacements [mm]			
			Nodes	Direction		
				X	Y	Z
11	D	Y	A	-0,0001166946	-0,002436352	-0,0006134486
			B	0,008777629	0,03854417	-0,01014285
			C	-0,0008939689	0,0009976311	-0,0002341414
			D	-0,04560834	0,09080686	-0,005838790
			E	0,008433251	0,0007510565	0,009432306

Optimized structure						
Load Case	Load introduction point	Load introduction direction	Displacements [mm]			
			Nodes	Direction		
				X	Y	Z
12	D	Z	A	-0,01176505	-0,003059773	-0,02529039
			B	-0,03776719	-0,05341389	0,1247795
			C	-0,03837701	0,03356296	-0,009230560
			D	-0,01118178	-0,005838790	0,4732922
			E	-0,006197502	-0,001031981	-0,04234276

Optimized structure						
Load Case	Load introduction point	Load introduction direction	Displacements [mm]			
			Nodes	Direction		
				X	Y	Z
12	E	Z	A	0,0003390118	0,01093270	0,002568270
			B	-0,004385575	-0,01097834	0,0001882530
			C	0,002231736	0,01235190	0,0007393029
			D	0,004253006	-0,006518512	0,004336698
			E	-0,01048259	0,005100449	-0,005656932